Bioconjugation, peptide-based targeting, and imaging of ultrasmall gold nanoparticles for cancer treatment

Wilson Poon

Master of Engineering

Department of Biomedical Engineering

McGill University

Montréal, Quebec

2014-08-20

A thesis submitted to McGill University in partial fulfillment of the requirements of the degree of Master of Engineering

DEDICATION

This document is dedicated to my parents for their never-ending support and love (in the form of constant nagging about when I would finally finish my Masters degree).

ACKNOWLEDGEMENTS

I would like to thank my supervisor, Professor Jay Nadeau, for giving me the opportunity to join her research group. Also, I want to thank all past and present members of the Nadeau Lab with whom I had the indelible pleasure of working alongside. In particular, thanks to (soon to be Dr.) Elaine Zhang for her meticulous tutelage and patience in mentoring me on all things biology; and Dr. Hicham Chibli for his words of wisdom on life and chemistry. In addition, I would like to extend thanks to the Teodoro lab (especially Ms. Ailsa Lee Loy and Ms. Isabelle Gamache) for protocol development and technical support on the animal experiments; Ms. Anna Jung for assistance with the iCAP Q ICPMS apparatus; Tabrizian lab (especially Mr. Ryan Tien Sing Young, Ms. Kaushar Jahan, Ms. Lamees Nayef, and Mr. Mina Mekhail) for teaching and graciously allowing me to use their lyophilizer and zetaPALS apparatus; and Mr. Christopher Lang and Ms. Jessica Perez for assistance on LaTeX.

ABSTRACT

Ultrasmall gold nanoparticles (AuNPs) conjugated with cytotoxic drugs, such as doxorubicin (Dox), have been shown to be promising chemotherapeutic agents for overcoming multidrug resistance common in cancers. The particles improve drug solubility, while the enhanced permeability and retention (EPR) effect improves targeting. The EPR effect results from the increased vascular permeability of cancerous or inflamed tissue, which causes particles of sizes <200 nm to accumulate preferentially in the pathological areas. However, the EPR effect is not well established in human cancers, so improved methods of active nanoparticle targeting have also been sought. To elucidate whether the EPR effect alone is sufficient for tumour targeting, we developed peptide-based bioconjugation active targeting strategies for gold nanoparticles. Bioconjugation to FREG-peptide is used to prevent FGF-2 dimerization in the tumour microenvironment. Bioconjugation to MSH-peptide and myxoma peptide are used to target tumour cell-specific molecules for melanocyte recognition and melanoma cytotoxicity. Bioconjugation to cRGD-peptide is used to target tumour neovasculature via binding to $\alpha_\nu\beta_3$ integrins. In vitro uptake and *in vivo* biodistribution of peptide-conjugated gold nanoparticles is investigated using a variety of modalities including confocal microscopy, transmission electron microscopy, photoacoustic imaging, fluorescence imaging, and inductively coupled plasma mass spectrometry.

ABRÉGÉ

La conjuguaison des nanoparticules dor (Au) à des agents cytotoxiques comme la doxorubicin constitue une approche chimiothérapeutique prometteuse capable de surmonter la résistance cellulaire répandu dans les cellules cancéreuses. Les particules améliorent la solubilité des médicaments tandis que l'effet de perméabilité et rétention (EPR) améliore leur ciblage. L'EPR est le résultat de l'augmentation de la perméabilité des vaisseaux des tissus cancéreux ou enflammés, ce qui permet aux particules inférieures à 200 nm de s'accumuler en préférence dans les tissus pathologiques. Etant donné que l'EPR des cancers humains n'est pas encore très bien étudier, les chercheurs se sont retournés vers un meilleur ciblage actif par les nanoparticules. Afin de comprendre si l'EPR seul est suffisant pour le ciblage des tumeurs, nous avons développé une stratégie de ciblage actif basée sur la conjugaison des nanoparticules d'or à des peptides. La bioconjugaison au peptide FREG est utilisée pour prévenir la dimérisation des FGF-2 dans le microenvironnement des cancers. La bioconjugaison aux peptides MSH ou myxoma est utilisée pour cibler des biomolécules spécifiques à la reconnaissance et au traitement du mélanome. La bioconjugaison au peptide cRGD est utilisée pour cibler la néovascularisation tumorale via son interaction avec les intégrines $\alpha_\nu\beta_3$. Des études d'absorption *in vitro* et de biodistribution *in vivo* des conjuguées, peptides-Au, sont effectuées moyennant plusieurs techniques telles que la microscopie confocale, la microscopie à transmission électronique, l'imagerie photoacoustique, l'imagerie de fluorescence, et la spectrométrie de masse à plasma couplé par induction.

TABLE OF CONTENTS

LIST OF TABLES

LIST OF FIGURES

CONTRIBUTION OF AUTHORS

The content of this thesis is adapted from a published review, manuscripts in preparation, and unpublished data in which the author has made a substantial contribution. Unless otherwise noted below, the experiments described in this thesis are the sole work of the author. J. Nadeau (McGill University, QC) has significant input into the experimental design and implementation.

Chapter 1

X. Zhang (McGill University, QC) and J. Nadeau (McGill University, QC) contributed to sections 1.1 and 1.4.

Adapted from: **Wilson Poon**, Xuan Zhang, Jay Nadeau. Nanoparticle Drug Formulations for Cancer Diagnosis and Treatment. *Critical Reviews^{TM}in Oncogenesis*, 19(X):1-24,2014. [In Print]

Chapter 3

X. Zhang (McGill University, QC) assisted with the synthesis of tiopronin-capped gold nanoparticles. X. Zhang and A. Lee Loy (McGill University, QC) assisted with the mouse injections. Undergraduate students O. Amzallag (McGill University, QC) and E. Tawagi (McGill University, QC) assisted with organ digestion and ICPMS sample preparation work under the direction of the author.

Adapted from: Wilson Poon, Xuan Zhang, Jay Nadeau [Unpublished Data]

Chapter 4

X. Zhang (McGill University, QC) assisted with the synthesis of tiopronin-capped gold nanoparticles, mouse injections, and fluorescence imaging. A. Heinmiller (VisualSonics Inc, ON) prepared the Lewis lung carcinoma-bearing mouse samples and performed the photoacoustic imaging. R. Mielke (University of California Santa Barbara, CA) performed the environmental scanning electron microscopy and scanning transmission electron microscopy.

Adapted from: Wilson Poon, Andrew Heinmiller, Xuan Zhang, Jay Nadeau [Unpublished Data]

CHAPTER 1
Introduction

Nanoparticles may be defined as engineered materials with at least one dimension < 100 nm. The size and shape confer unique physicochemical properties that make these particles useful for cancer imaging and therapy in a variety of ways: they can improve drug delivery; they can act as anti-cancer agents alone or in synergy with delivered cargo; and they can be made multifunctional to provide targeting, imaging, and therapy all in one construct.

1.1 Nanoparticles for Drug Delivery and Cancer Therapy

1.1.1 Drug Delivery

Nanoemulsions and liposomes can be used to improve the pharmacokinetics of chemotherapeutic drugs, which are often highly hydrophobic. Such preparations include several FDA-approved drugs, many of which are in widespread use, such as Abraxane (a formulation of paclitaxel) and Doxil (a formulation of doxorubicin). Such agents have been reviewed extensively [1, 2, 3, 4]. Most are delivered intravenously, but nanoparticle encapsulation has also been used for creation of oral formulations of chemotherapeutic drugs. Oral drug delivery improves patient quality of life and reduces cost, but is difficult due to degradation of drugs in the gastrointestinal tract and unpredictability of dosing, which can be critical with compounds that have a low therapeutic index.

Other nanoparticle preparations influence drug delivery in more complex ways, down to the cellular and subcellular level. Conjugation of multiple drug molecules to the surface of a nanoparticle effectively concentrates the drug in a very small area, which can influence endocytosis and affect cell membranes. The biological behavior of such conjugates is highly size- and shape-dependent, both at the cellular and organismal level. Manufactured nanomaterials can be reliably produced in a large range of sizes, shapes, aspect ratios, and surface-to-volume ratios; common shapes include spheres (solid or hollow), rods, stars or prisms, and nanotubes as shown in Figure 1–1 [5].

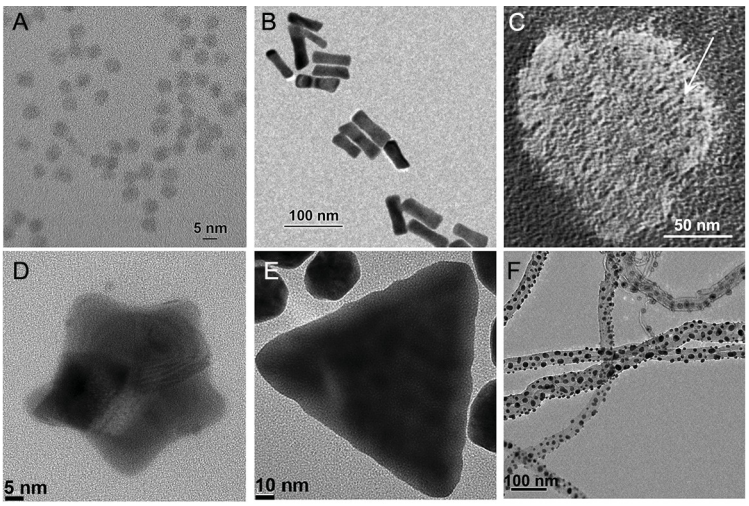

Figure 1–1: Some sizes and shapes of biologically compatible nanostructures. (a) Spherical CdTe quantum dots. (b) Au nanorods. (c) CdSe quantum dots (arrow) embedded in a lipid vesicle. (d) Au nanostar. (e) Au nanoprism. (f) Carbon nanotubes decorated with CdSe QDs (image courtesy the McGill Plasma Processing Lab).

Figure 1–2 summarizes some of the mechanisms that lead to improved subcellular delivery of nanoparticles vs. small molecule drugs alone. Spherical particles

$40 - 60$ nm in diameter can crosslink membrane receptors, leading to increased uptake [6]. Smaller particles can improve cellular uptake rates; particles of sizes < 3 nm have been shown to enter cell nuclei spontaneously. Larger particles may enter nuclei through specific mechanisms; in one study, 31 nm Au particles cross linked by Pt were shown to enter the nuclei of lung cancer cells [7]. Particles that remain attached to drugs may limit the function of drug efflux pumps, thus overcoming transporter-associated drug resistance. The ability of nanoparticles to overcome cellular doxorubicin resistance, for example, has been shown with porphyrin-polylactide nanoparticles [8] and with gold nanoparticles [9].

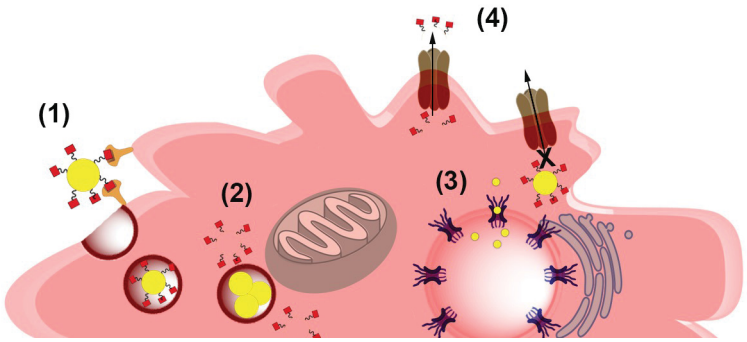

Figure 1–2: Mechanisms of interaction of nanomaterials with cells. (1) Receptor-mediated interactions, which may be multivalent. (2) Endosomal processing and drug release; interactions of particles and released drugs with endosomes, mitochondria, and other organelles. (3) entry through nuclear pores. (4) Interaction with drug efflux pumps.

On an organismal level, optimized nanoparticle formulations can help drugs evade the immune system and avoid sequestration by the reticuloendothelial system

(RES), and even to penetrate the blood-brain barrier‘[10, 11]. A 2008 study compared the tissue distributions of injected Au nanoparticles (a commercial aqueous suspension; probably citrate-capped) ranging in size from 10 to 250 nm.

Only 10 nm nanoparticles were found widely distributed outside the liver and spleen [12]. Another study compared identical nanoparticles capped with polyethylene glycol (PEG) chains of different lengths that terminated in NH_2, COOH, or OCH_3. The unreactive methoxy group showed the best delivery to tumors, while the COOH terminated particles were cleared rapidly [13]. Filamentous nanostructures may persist for a long time in the blood circulation. In one study, filomicelles were found to persist in the bloodstream and deliver paclitaxel to tumors [14].

1.1.2 Photodynamic Therapy

Quantum dots (QDs) have attracted a vast amount of interest as photodynamic therapy agents, because they may also be photosensitized by any molecule capable of transferring energy or electrons to the nanoparticle, leading to production of singlet oxygen as shown in Figure 1–3 [15]. Thus any anti-cancer drug with the appropriate spectrum can become a photodynamic therapy agent if conjugated to an activating QD. Increased reactive oxygen species (ROS) production compared with free drug have been shown with QDs conjugated to traditional photodynamic therapy (PDT) agents such as phthalocyanines [16, 17], merocyanine-540 [18], porphyrins [19], rose bengal and chlorin [20], as well as to other molecules such as platinum-based chemotherapeutic agents [21], toluidine blue [22], and dopamine [23].

In addition, QDs may be very efficiently excited by 2- and even 3-photon processes, so that deeply-penetrating near-infrared light may be used to excite them.

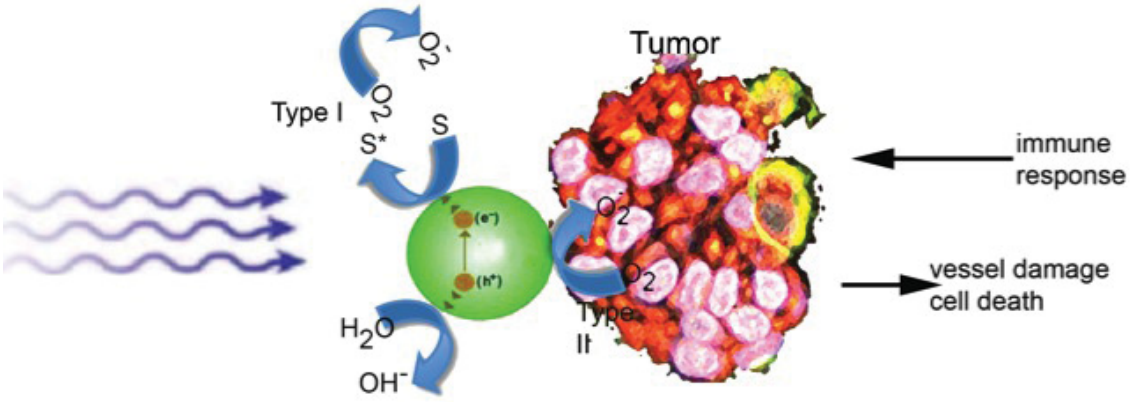

Figure 1–3: Possible mechanisms of action of photodynamic therapy (PDT). Light (shown as blue) excites a photosensitized nanoparticle (shown as green) creating an electron-hole pair (orange circles). The electron may interact with a substrate S (such as a lipid or other cell molecule) to create a substrate S*, which interacts with oxygen to create reactive oxygen species. This is known as a type I reaction. A type II reaction occurs when the particle interacts directly with oxygen to create ROS. In addition, the particle hole might interact with water to create hydroxyl radicals (OH^-). Any of these radical species can cause cell death and damage to microvessels, and can generate immune responses.

The ideal phototherapeutic window for PDT is in the near IR, from 780 to 950 nm, yet few PDT agents are excited with light of these long wavelengths. This is especially crucial for pigmented tumors, whose melanin granules absorb visible light, making them refractory to visible-wavelength PDT [24]. Thus, there is rapidly emerging interest in the field of two-photon PDT [25, 26] for thick or pigmented tumors. Photosensitizers for such applications must have large two-photon absorbance cross-sections (2PA); unfortunately, most traditional PDT agents show low 2PA, 10−100 Goeppert-Mayer units (1 Goeppert-Meyer unit = 10−50 $cm^4 \cdot s \cdot photon^{-1}$). Agents

developed specifically for 2-photon PDT have values from 1,200 to 1,500 Goeppert-Meyer units, and have been shown to be excitable through 5−10 cm of tissue (the entire thickness of a mouse body) [27, 28]. Quantum dots (both Cd-based and InP) have tremendous 2-photon cross-sections: up to 47,000 Goeppert-Meyer units [29, 30]. However, as of late 2013, the potential of nanoparticles as two-photon PDT agents remains largely unexplored; only a few reports of two-photon PDT on cell culture systems exist [25], largely because of the complexity and expense of the lasers needed to implement a 2-photon protocol.

1.1.3 Radiotherapy

High Z contrast media, such as iodine, gadolinium or gold, can radiosensitize tissue in which they are present, leading to increased local tissue damage (within a several-micron radius). This is particularly relevant to low energy X-rays and gamma rays ($E_{avg} < 100$ keV) because the mode of interaction is primarily photoelectric [31, 32]. An early animal study used a combination of the EPR effect and radiosensitization to target mammary tumors in a mouse model [33]. Small Au nanoparticles (1.9 nm diameter) injected intravenously selectively accumulated in cancer tissue, with 2.7 g Au/kg body weight resulting in 7 mg Au/g in tumor. With a typical of 250 kVp X-ray therapy, one-year survival was 86% (compared to 20% with X-rays alone and 0% with gold alone). This remarkable study was followed by numerous theoretical and experimental studies investigating the mechanism of Au nanoparticle action as well as attempting to optimize Au particle concentration, size, and targeting as well as the energy and dose of applied X-rays [34, 35, 36, 37].

The result is several on-going clinical trials of gold-nanoparticle assisted radiation therapy (GNRT) for cancers treatable by kV X-rays, particularly locally advanced breast cancer, which is life-threatening despite its local nature. Dose enhancement using 140 kVp X-rays is at least a factor of 2 at 7 mg Au/g tumor; for MV X-rays, enhancement is only 1-7%. For brachytherapy using ^{192}Ir gamma rays ($\sim$380 keV), enhancement is up to 30%. Dose enhancement is increased when particles are taken up by tumor cells. Uptake can be maximized by reducing particle size, using intratumoral delivery, or targeting the particles to cells using specific receptors [36, 38].

There are two important barriers to GNRT: first, the large concentrations of Au required are prohibitive for humans in terms of both cost and potential toxicity (2.7 g/kg corresponds to over 100 g of Au injected for even the smallest adult); and second, the degree of dose enhancement is not sufficient for radiotherapy-resistant cancers. Other agents are being sought that use additional mechanisms besides the photoelectric effect to enhance radiosensitivity.

1.1.4 Hybrid Photodynamic and Radiotherapy

The concept of nanoparticle-assisted hybrid of radiation therapy PDT has attracted a good deal of attention over the past five years [39]. PDT and radiation treatment may work in synergy, with their combined effects greater than additive [40]. The concept is simple: use a dye sensitizer that may be excited with ionizing radiation rather than light, or attach an ordinary photosensitizing dye to a nanoparticle that emits light when excited by therapeutic radiation (scintillates). If this light

overlaps the absorbance spectrum of the dye, then the dye will work effectively as shown in Figure 1–4 .

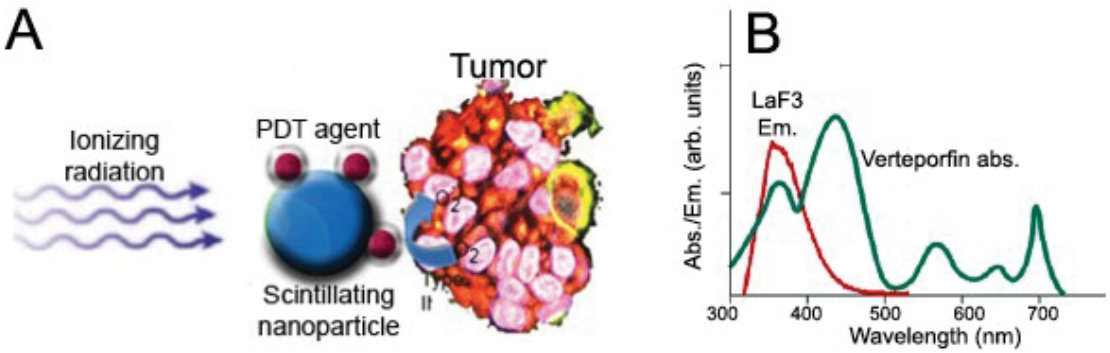

Figure 1–4: Concept of hybrid radio/photodynamic therapy. (a) In the hybrid concept, ionizing radiation is used to excite a scintillating nanoparticle whose emission spectrum overlaps the absorbance of the PDT dye. The dye then functions as in PDT. (b) Emission of a typical scintillation emission (LaF_3:Ce nanoparticles) with verteporfin, an FDA-approved PDT agent.

LaF_3:Ce particles are a type of scintillating nanoparticle whose emission (350−500 nm) overlaps the absorption of many photosensitizing agents, including chlorins, phthalocyanines, porphyrins, and the clinical photodynamic therapy drug Photofrin (porfimer sodium), promising excellent energy transfer and therefore efficient singlet oxygen generation. Modeling of realistic energy-transfer efficiencies vs. X-ray energy suggests that X-ray energies of < 200 keV are optimal to excite LaF_3:Ce-photosensitizer conjugates, with doses < 100 Gy required to generate a killing amount of singlet oxygen. Thus, brachytherapy alone may lead to efficient cell death using these new particles for a variety of cancers. In addition, for intracavitary brachytherapy, or brachytherapy on lesions < 5 mm deep such as many head and neck cancers

(HNCs), use could even be made of electronic kV sources (currently FDA approved) that would further improve the dose enhancement.

Lanthanum (III) ions are of low toxicity in humans; lanthanum carbonate is currently being used as a drug for dialysis patients in managing excess phosphate levels [41]. However, the *in vivo* toxicity of lanthanum-based nanoparticles remains unknown, and animal models comparing the effectiveness of scintillating particles with and without photosensitizers have not yet been reported.

1.1.5 Photothermal Therapy

Photothermal therapy uses localized heating to kill cells. Mild hyperthermia ($40 - 46\,^{\circ}\mathrm{C}$) can induce apoptosis; higher temperatures rupture cell membranes, leading to necrosis. IR light, ultrasound, and microwaves may all be used to effect local heating, though the degree of damage to surrounding normal tissue must be considered for each method. The addition of a nanoparticulate agent that can increase heating in response to the chosen stimulus has been investigated for several years. Au nanoparticles excited by light at their plasmonic resonance relax nonradiatively within 100 ps to produce a local temperature increase. In vitro, EGFR-antibody-targeted Au nanoparticles bind more densely to squamous carcinoma cells than to benign cells, so that less than half the energy is needed to eliminate the malignant cells than to kill the benign cells [42].

Spherical Au particles have plasmon peaks in the visible wavelengths, however, making them impractical for use *in vivo*. In order to penetrate tissue, excitation wavelengths in the near-IR are needed. Red-shifting of the plasmon peak can occur by elongating the particles into rods, with the wavelength proportional to the aspect

ratio of the rod, or by creating Au nanoshells or nanocages [43]. The absorbance of shells can be tuned by adjusting the ratio of size to shell thickness; the shells may be hollow or may surround a core of another material. Nanocages are created by creating vacancies in the crystal with another, less-noble metal, usually Ag; the displacement of the Au leads to plasmonic red-shift [44, 45]. Other shapes, such as nanohexapods, have also been proposed [46]. These particles and their success in *in vitro* and small animal studies have been well reviewed elsewhere [43, 47, 48, 49]. Both nanorods and nanoshells are moving into clinical use in humans. The company Nanospectra Biosciences has received an Investigational Device Exemption (IDE) from the FDA for a pilot study of Au nanoshells in patients with head and neck cancer. The National Cancer Institute Alliance for Nanotechnology in Cancer has sponsored a gold nanorod study; the project will involve full preclinical toxicity testing of the nanomaterials.

Other materials, such as carbon nanotubes (CNT) and graphene, also absorb in the NIR and generate heat, so may potentially be used for photothermal therapy. The barrier to their clinical use is greater than for Au, but promising studies have been done on mice using PEGylated untargeted CNTs [50], as well as CNTs targeted to mitochondria [51] or to annexin [52]. Graphene oxide is a newcomer to the field, but a recent study showed impressive results in mouse U87MG glioblastoma xenografts [53].

1.1.6 Multifunctionality

One of the greatest strengths of nanoparticles is that they can be made to provide contrast in multiple imaging modes and to be indicators and therapeutic agents

simultaneously. Both the core material and the particle surface may be made multifunctional. Sometimes adjustment of the core shape and size is all that is needed to create multifunctionality; for example, ultrasmall Au nanoclusters (1.9 nm) show NIR fluorescence along with the usual contrast properties of gold [54, 55]. Core materials may also be doped or shelled with other materials to provide imaging contrast - for example, a quantum dot may be capped with a gold shell [56], or an iron oxide core may be capped with fluorescent semiconductor material [57]. Semiconductors may be doped to improve fluorescence or enable new imaging modalities. For example, cadmium-free QDs may be doped with Mn to improve optical properties, or ZnO doped with lanthanum [58, 59]. Doping CdSe with Mn or Gd can render the particles super-paramagnetic for MR contrast [60]. For all of these hybrid structures, the synthesis procedures are often challenging, since the properties of one or both core materials may be lost unless the parameters are carefully optimized.

The surface chemistry also contributes to the multifunctionality of nanoparticles. Depending on the size of the particle, tens to thousands of ligands may be coupled to the surface. These ligands may include tracers (such as radiotracers for positron emission tomography) [61], fluorescent dyes, or multiple targeting agents. The concentration of tracers usually does not have to be high, and so they may be combined with targeting and therapeutic moieties. In some cases, exact stoichiometries can be obtained by functionalizing the particle with different active groups. Such control of synthesis is important for regulatory approval [62, 63, 64]. Figure 1–5(a) shows a schematic of a theoretical multifunctional particle.

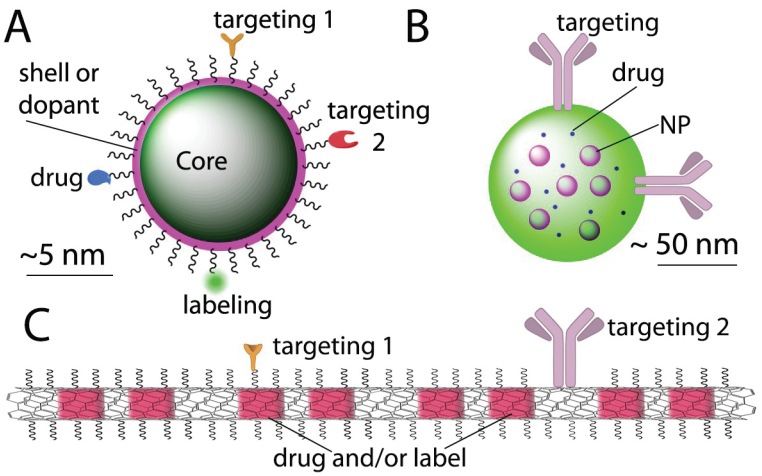

Figure 1–5: Some general types of multifunctional nanomaterials. (a) The small size of a nanoparticle can be retained by shelling or doping with a different material to provide additional physicochemical properties. The hybrid material may then be conjugated to one or more targeting or therapeutic agents; agents for additional contrast, such as PET isotopes, may also be attached. (b) Multiple nanoparticle types and/or small molecules may be embedded into larger organic capsules. The overall size of the construct is increased, but many variations are possible. (c) Carbon nanotubes lend themselves readily to conjugation to different agents via π-stacking and direct conjugation.

Another way to achieve multifunctionality is to encapsulate a variety of different materials within a polymer or matrix. This matrix may be porous to allow drug molecules to diffuse out. One or more types of nanoparticles may be embedded within the structure; this can also serve to reduce toxicity of nanomaterials, particularly if the larger structures are readily excreted as shown in Figure 1–5(b). A large number of such structures have been described in the literature: some examples use liposomes [65, 66] solid lipid nanoparticles [67], and polymers [68, 69] containing one or more nanoparticle types along with anticancer drugs. Elongated nanomaterials such as nanotubes lend themselves readily to multiple types of functionalization.

More than one molecule may be attached via π-stacking; the nanotube may also be conjugated to one or more targeting agents as shown in Figure 1–5(c). For example, in one study, both doxorubicin and a fluorescent label (fluorescein isothiocyanate) were attached to the nanotubes by π-stacking, and folate was conjugated for targeting [70]. Nanotubes have also been conjugated to iron oxide [71] and gold particle [72] for multifunctional detection. Novel methods of solubilization of the nanotubes that facilitate conjugation of multiple labels are also being explored; one example is DNA amplification on the surface of the nanotube, creating a long single-stranded molecule that may be attached to multiple ligand [73].

1.2 Nanoparticles for Medical Imaging

The goal of cancer imaging is for early detection of tumour cells before the angiogenic switch or metastasis can occur [74, 75, 76], which has been shown to be fundamental for better prognosis and patient survival in cervical, breast, colorectal, prostate, and lung cancers, just to name a few [77]. There are currently many nanoparticle-based imaging technologies in research and development to improve upon the sensitivity and specificity of cancer imaging techniques. Common imaging modalities used in conjugation with nanoparticles for cancer diagnosis include optical imaging, x-ray computed tomography (CT), magnetic resonance imaging (MRI), and ultrasonography. It is also common for engineering nanoparticles to be compatible with multiple modalities of imaging, as well as to deliver therapeutics simultaneously. A table summarizing the use of nanoparticles as contrast agents in the various modalities of medical imaging is presented in Table 1–1.

Table 1–1: Nanoparticles for Various Medical Imaging Modalities

Imaging Modality	**Optical Imaging**	**Computed Tomography**	**Magnetic Resonance Imaging**
Type of wave	Visible of near-infrared light	X-ray	Radio-frequency waves
Tissue penetration depth [78]	$300 - 800$ μm	No limit	No limit
Spatial resolution [79]	30 μm $-$ 3 mm	$50 - 200$ μm	$25 - 100$ μm
Temporal resolution [79]	Seconds to minutes	Minutes	Minutes to hours
Solid nanoparticle contrast agents	Quantum dots, upconversion nanoparticles, nanocarriers with fluorescent dye	Metallic (Ta, Pt, Au, Bi) nanoparticles, lanthanide (Gd, Dy, Yb) nanoparticles, nanocarriers with iodine	Iron oxide-based nanoparticles, Gd-containing/doped nanoparticles
Nanoparticulate contrast mechanism	Luminescence (fluorescence or upconversion)	X-ray attenuation	Altercation of the relaxivities in surrounding water molecules
Concomitant cancer therapies	Photodynamic therapy, drug delivery	Drug delivery, dose-enhanced radiotherapy, photothermal therapy	Magnetic drug targeting, AMF-induced hyperthermia, drug delivery

1.2.1 Optical Imaging

Optical imaging for *in vivo* cancer detection is typically performed by intravenous or intradermal administration of fluorescent contrast agents followed by near-infrared fluorescence (NIRF) imaging and tomography [80], fluorescence endoscopy [81], spectrofluorometry [82], or laparoscopy [83]. Preclinical (and potential clinical) applications of optical imaging for cancer include sentinel lymph node mapping, noninvasive lymph node staging, neoplasm visualization, and image-guided surgery. Near-infrared fluorescence emission of wavelengths between 650-900 nm are the most useful as biological tissues display low absorption in this regime [84]. There are many fluorescent dyes used for cancer diagnosis, such as cyanine dyes, squaraine, phthalocyanines, porphyrin derivatives, and borondipyrromethane analogues, but they generally suffer from the disadvantages of low fluorescence quantum yields in the near-infrared wavelengths, high reactivity, and poor photostability [85, 86]. Engineered semiconductor nanocrystals (also known as inorganic quantum dots), upconversion nanoparticles, and fluorescent-dye loaded silica nanoparticles have been developed to be used as better alternatives in optical imaging for cancer detection.

Semiconductor nanocrystals, also known as inorganic quantum dots, are typically core-shell architecture nanoparticles of group II/VI and III/V elements stabilized and capped with an organic functional layer [85]. Inorganic quantum dots have broad excitation spectra, sharp and size tunable emission profiles, as well as robust signal strength [87]. The size dependent emission characteristics of inorganic quantum dots arise due to quantum confinement, which occurs in semiconductor materials when the physical dimensions of the crystal structure are smaller than a critical value

known as the exciton Bohr radius (usually 2 - 10 nm in diameter) [88]. Depending on the elemental composition and size of the QDs, their emission wavelengths can be tuned to the near-infrared region for *in vivo* and deep tissue imaging [89]. The sharp emission profiles of QDs minimize spectral overlap in multicolor fluorescence systems and their broad excitation spectra allow the possibility of using a single excitation source [87]. These optical properties make QDs amendable for a wide variety of multicolor fluorescence applications as demonstrated by Kobayashi *et al.* in multicolor imaging by a single excitation source in investigating multiple lymphatic basins simultaneously in mice *in vivo* [90]. Improving upon previous lymphatic drainage studies, which used X-ray or magnetic resonant lymphangiography capable of only studying one lymphatic basin at a time, Kobayashi *et al.* injected carboxyl CdSe and CdTe QDs with different emission peaks intracutaneously into mice at different locations of the neck and upper trunk to study the lymphatic network and predict the route of cancer metastasis into lymph nodes [90]. The carboxyl QDs also maintained strong fluorescence signal for up to 3 hours and did not show up in secondary draining lymph nodes, which make them excellent probes for sentinel lymph node identification in cancer staging and prognosis [90]. Another application of QDs to optical cancer imaging is tumour imaging for image-guided surgery. Surgical removal of tumours prior to metastasis is often the most effective method to cure cancer, but is complicated by ill-defined tumor margins and poor visibility of microscopic tumours in surrounding healthy tissues [89]. Li *et al.* administered NIR-emitting cyclic RGD-peptide conjugated CdTe QDs intravenously to mice bearing U87MG glioblastoma tumours on the front flank [91]. The conjugated quantum dots actively targeted the

xenograft tumour and when Li *et al.* used intraoperative NIR fluorescence imaging to visualize the tumour, they were able to perform complete image-guided resection to precisely remove the tumour mass [91]. There has been extensive debate around the toxicity of QDs *in vivo*, mostly due to contrary results from a lack of standardized toxicity protocol and multifarious quantum dot designs [92]. However, it is generally agreed upon that the desorption of Cd, Se, Zn, Te, Hg, and Pb from the nanoparticle core and generation of ROS are the major sources of QD related toxicity [92]. To address these issues, it has been shown that InP and InP/ZnS quantum dots are safer alternatives to Cd-containing QDs in terms of *in vitro* and *in vivo* cytotoxicity [93, 94].

Upconversion nanoparticles (UCNPs) are rare earth-doped ceramic nanomaterials which exhibit anti-Stokes shift optical characteristics, where long wavelengths (like near-infrared light) are converted to shorter wavelengths (such as visible light) via non-linear sequential absorption of two or more photons [95]. UCNPs offer distinct advantages over quantum dots and organic dyes in optical imaging manly because they can be excited by near-infrared wavelengths. UCNPs have excellent signal-to-noise ratios and improved detection sensitivity due to reduced biological autofluorescence, deep tissue penetration, and reduced tissue photodamage [96]. Rare earth components in UCNPs are also approximately one-thousand fold less toxic than the heavy metals within conventional inorganic quantum dots [97]. Xiong *et al.* have developed RGD-peptide labeled Yb, Er, and Tm-doped $NaYF_4$ UCNPs that actively target $\alpha_\nu\beta_3$ integrin receptors for upconversion luminescence *in vitro*, *ex vivo*, and *in vivo* imaging [98]. Xiong *et al.* were able to demonstrate *in vivo* and *ex vivo* imaging

of U87MG glioblastoma tumours within nude mice and achieve penetration depths of 600μm in tissue slices [98]. Recently, Pan *et al.* reported the use of folic acid-conjugated silica-modified Gd and Tm-doped NaYbF4 nanocrystals for targeted *in vivo* luminescence imaging of folate receptors on MGC-803 cells in a gastric cancer tumour xenograft nude mice model [99]. Despite the obvious advantages of upconversion nanoparticles in *in vivo* imaging, it is important to note that their development is still in the early stage with many questions regarding their cytotoxicity, biodistribution, and excretion routes remaining to be investigated systematically [100].

Aside from the aforementioned nanoparticles, other classes of nanoparticles have also been developed for cancer detection by optical fluorescence imaging, such as aggregation-induced emission nanoparticles [101], NIR fluorescent albumin nanoparticles [102], fluorophores in polymer, dendrimer, or liposome nanocarriers [103].

1.2.2 X-ray Computed Tomography

X-ray computed tomography (CT) imaging is one of the most convenient imaging and diagnostic tools available in hospitals due to its availability, high efficiency, and low cost [104]. Conventionally, CT is used for structural imaging for tumour location, size, and spread by injecting into patients intravenously or intraarterially small iodinated molecules such as iopromide and iodixanol as contrast agents [104, 105]. While these iodine agents are effective at absorbing x-rays, they undergo rapid renal clearance and vascular permeation, which limit imaging time [104]. Furthermore, they cannot be used in molecular or functional imaging as it is difficult to deliver sufficient concentration of their conjugates with antibodies and targeting moieties [106].

Nanoparticles are emerging as new contrast agents due to (1) their prolonged circulation time, (2) specific molecular targeting capabilities for differential uptake in tumours, and (3) tunable size and composition of high atomic number elements with K-shell electron binding energy (K-edge) values within the clinical use X-ray spectrum for improved x-ray attenuation and necessitating lower patient doses [104, 107]. The primary types of nanoparticulate x-ray contrast agents include the metallic nanoparticles containing $_{73}$Ta, $_{78}$Pt, $_{79}$Au, or $_{83}$Bi, lanthanide nanoparticles containing $_{64}$Gd, $_{66}$Dy, or $_{70}$Yb, and binary contrast agents containing multiple elements with differential K-edge values [107].

Gold nanoparticles as an x-ray contrast agent were first reported by Hainfeld *et al.* [106]. Gold nanoparticles have high x-ray attenuation due to its high atomic number, high density, and high absorptivity due to its favourable k-edge energy in the range of clinical CT operating voltages [106, 108]. Further advantages of gold nanoparticles are its relative ease of synthesis, multifarious methods of surface modification and functionalization, as well as its good biocompatibility and nontoxicity [105, 108]. Reuveni *et al.* demonstrated the use of molecular cancer imaging with clinical CT and gold nanoparticles by using PEGylated and anti-EGFR antibody conjugated gold nanoparticles to target A341 human head and neck tumour cells in mice *in vivo* [109]. Reuveni *et al.* reported significant and specific contrast enhancement from the actively targeted nanoparticles even with a clinical CT for mice [109]. Although the high price of gold coupled with the need for high dosage of gold nanoparticles to achieve sufficient contrast represents a challenge in the commercialization and widespread use of gold nanoparticles as CT contrast agents [106, 107].

Bismuth sulfide (Bi_2S_3) nanoparticles are less expensive than gold nanoparticles and have been shown to be equal or superior to iodinated contrast agents by Rabin *et al.* [107, 110]. Controlled synthesis and surface modification of Bi_2S_3 nanoparticles is still relatively unexplored, but ligand exchange methods with poly(vinylpyrrolidone) and thioether formation methods between PEG-maleimide and cysteine moieties have been demonstrated thus far [111, 112]. Specifically, Kinsella *et al.* has demonstrated the use of LyP-1 peptide-labeled Bi_2S_3 nanoparticles for targeted CT imaging of 4T1 breast cancer in mice *in vivo* [112]. Kinsella *et al.* reported that their bismuth-based nanoparticle contrast agent yielded sufficient tumour contrast up to 1 week after injection, and the nanoparticles primarily undergo a fecal clearance [112]. However, the intrinsic toxicity of bismuth remains a concern [113]. Tantalum oxide nanoparticles (TaO_x) are also inexpensive, can be modified by silane derivatives, and are generally considered non-toxic and bioinert [104, 113]. Oh *et al.* have demonstrated the use of PEGylated and rhodamine-labeled TaO_x nanoparticles in sentinel lymph node mapping with CT 2 hours after intradermal injection [113]. There are advances in the development of TaO_x nanoparticles to reduce the viscosity of concentrated particle solutions and decrease their tissue retention *in vivo* [114].

Lanthanide nanoparticles are often designed as multimodal upconversion fluorescence/MRI/CT imaging contrast agents [105, 107]. Doping with gadolinium in lanthanide nanoparticles provides strong T_1 and T_2 relaxation times for MRI contrast, which will be described in the next section. Lanthanides, especially ytterbium, have proper K-edge energies within the higher-intensity region of the x-ray spectrum used in clinical CT, providing greater intrinsic CT contrast and lower radiation exposure

to patients as compared to iodine and other metallic elements [115]. Experiments by Liu *et al.* showed PEGylated Yb nanoparticles provides better CT signal and longer circulation time than conventional iobitridol, and also has a reduced dose requirement, which suggests they can be used for detecting cancer metastasis by lymph node mapping [115]. However, the relatively large size of the PEGylated lanthanide nanoparticles have slow elimination and may be a source of concern [115].

Binary contrast agents are nanoparticles that contain two CT contrast elements with differential K-edge values within the x-ray spectrum to have greater x-ray attenuation than conventional iodine agents over the entire operating voltage range of clinical CT [107]. The operating voltage of clinical CT ranges from 80 kVp when used on pediatric patients to 140 kVp for overweight patients, and this affects the x-ray attenuation of each element due to the location of the K-edge in relation to the intensity region of the x-ray spectrum generated at each operating voltage [116]. Liu *et al.* developed PEGylated and silica-coated BaYbF5 nanoparticles as binary CT contrast agents [116]. Their studies showed the binary contrast agents provides better contrast efficacy than lobitridol and single contrast element nanoparticles over the entire range of $80 - 140$ kVp and can be used for angiography in rabbits [116]. Whether these nanoparticles can be adapted for cancer imaging by CT remains to be shown. Nanoparticulate x-ray contrast agents have shown great promise in cancer detection, but much work is still required in preclinical development for targeted molecular and functional imaging of tumours and clinical validation, specifically determining biocompatibility, contrast efficacy, cost effectiveness, *in vivo* circulation time, and long term colloidal stability in physiological conditions [107].

1.2.3 Magnetic Resonance Imaging

Magnetic resonance imaging (MRI) is a powerful diagnostic tool for tumour detection because it can give high resolution anatomic images of soft tissues [117]. MRI can be performed with magnetic nanoparticles or nanocarriers encapsulating MRI contrast agents. Magnetic nanoparticles are typically ferrites with a general composition of MFe_2O_3 (where M is a divalent metal cation that includes nickel (Ni), cobalt (Co), magnesium (Mg), or zinc (Zn)), magnetite (Fe_3O_4), maghemite (γ-Fe_2O_3), or iron-platinum alloys (FePt) [118]. These contrast agents modify the relaxation rates of surrounding water proton spins to generate contrast in nanoparticle concentrated regions [119]. The relaxation rate is based on (1) longitudinal relaxation (also known as T_1 or spin-lattice relaxation), which is related to the energy exchange between spins and their surroundings, and (2) transverse relaxation (also known as T_2 or spin-spin relaxation), which is related to the loss of phase coherence of the spins due to spin-spin interactions [119]. Magnetite and maghemite-based ferromagnetic and superparamagnetic nanoparticles have been used clinically as T_2 contrast agents for around 20 years and are considered highly biocompatible with negligible toxicity concerns [119, 120].

Commercially available superparamagnetic iron oxide (SPIO) nanoparticles, such as ferumoxide and ferucarbotran, are taken up intrinsically by Kupffer cells and typically accumulate in the liver, spleen, and bone marrow [117, 120, 121]. If there are primary liver tumors or liver metastasis, the region will be devoid of Kupffer cells and have negligible accumulation of SPIO nanoparticles, therefore allowing MRI

detection of abnormal tissue [117]. Ultrasmall superparamagnetic iron oxide (USPIO) nanoparticles with diameter less than 50 nm, such as Combidex, are used in lymph-node imaging for tumor staging [117]. USPIO are only taken up by nodal macrophages in normal lymph nodes since nodes with metastasized malignant cells do not have macrophages, which results in different signal intensities on MR images [117, 122]. Modification of SPIO and USPIO nanoparticles to achieve greater relaxivities and add new targeted capabilities for improved tumour detection have been explored by using a variety of surface functionalization methods such as ligand exchange, organic coating, and inorganic coating [117, 119]. It is important to optimize the surface chemistry of magnetic nanoparticles as the MR relaxivity is decreased by excluding water molecules from the magnetic core, while conversely improved by increasing the residence time of water molecules due to hydrogen bonding to the ligands [123]. Xie *et al.* reported the use of lactoferrin-conjugated SPIO nanoparticles that cross the blood-brain barrier to detect brain gliomas in a C6 glioma-rat xenograft animal model with improved T_2 contrast of the tumour and surrounding vascular regions for up to 48 hours [124]. Wadajkar *et al.* demonstrated the use of thermo-responsive polymer-coated and R11 peptide conjugated iron oxide nanoparticles for active targeting and T_2 contrast MR imaging of prostate cancer *in vivo* in a PC3-KD prostate cancer xenograft SCID mouse model, with therapeutic potential for magnetic hyperthermia and temperature-dependent drug release [125].

More recently, nanoparticulate T_1 contrast agents for positive MR contrast are being developed as alternatives to negative T_2 contrast agents [117, 119]. The main advantage of T_1 contrast agents is their ability to enhance a signal-increasing imaging

effect for positive contrast to clearly distinguish nanoparticle-concentrated regions from pathogenic or other biological conditions [117]. Conversely, T_2 contrast agents produce signal-decreasing effects for negative contrast and result in dark signals that can potentially be misinterpreted as erroneous pathogenic conditions [117]. The use of T_2 contrast agents also suffers from susceptibility artifacts or the blooming effect due to their disruption of magnetic homogeneity in neighbouring normal tissues [117]. Examples of reported nanoparticulate T_1 contrast agents in development include nanocarriers encapsulating Gd^{3+} ions, as well as nanoparticles containing Gd_2O_3, GdF_3, $GdPO_4$, MnO, or FeCo [117]. However, these contrast agents suffer from complicated or expensive synthesis, difficulty in controlling of uniform size distribution, and a poor understanding of the underlying contrast mechanism in some cases [117]. There is also some concern regarding the toxic side effects of leached gadolinium ions from these nanoparticles, such as nephrogenic systemic fibrosis [123].

Interestingly, while there were numerous nanoparticulate MR contrast agents approved for clinical use, several of these products have been withdrawn from American and European markets [126]. It is believed that the development of multimodal clinical imaging contrast agents represents a more promising approach to accurate tumor diagnosis and nanoparticle commercialization [126]. For example, Madru *et al.* have reported the development of ^{99m}Tc-labeled superparamagnetic iron oxide nanoparticles for multimodal single-photon emission computed tomography (SPECT)-MRI and demonstrated for sentinel lymph node mapping [127]. Additionally, Ma *et al.* successfully performed *in vivo* breast tumour imaging by dual-modality NIR fluorescence imaging and MRI by their engineered MQQ-probes, which are multilayered,

core-shell silica nanoprobes of encapsulated quantum dots and magnetite nanoparticles, conjugated to anti-HER2 antibodies [128].

1.3 Nanoparticle Biodistribution

The biodistribution and clearance of nanoparticles in general is a very complex and important issue when discussing efficacy of nanomedicines or toxicity of nanoparticles in the human body for FDA approval [129]. The general scheme of nanoparticle clearance seems to be through three main mechanisms: renal, hepatic, and RES (reticuloendothelial system) [130].

In renal clearance through the kidneys and ultimately excretion into the urine, the glomerular capillary wall has fenestrated endothelium, highly negatively charged glomerular basement membrane and podocyte extensions of glomerular epithelial cells [131]. The size barrier is the filtration slit, with physiological pore size of 4.5 - 5 nm. Particles between 6 - 8 nm can still pass through based on charge interactions (positive NPs are more readily filtered due to the negative membrane) [131]. Particles may also become resorbed in the proximal tubule due to the negatively charged nature of the epithelial cells [131]. Renal clearance is the preferable pathway for nanoparticles to minimize intracellular catabolism and enzymatic modification leading to undesirable nanomaterial retention and cytotoxicity [131].

In hepatic clearance, hepatocytes in the liver eliminate foreign substances and particles by endocytosis, followed by enzymatic breakdown of the particles, and excretion into the bile via the biliary system [131]. Nanoparticles between 10 - 20 nm in size undergo rapid liver uptake, but the subsequent hepatic processing and biliary excretion is usually slow [131]. The prolonged retention of nanoparticles from this

relatively slow clearance pathway and associated complex catabolites represents a concern of toxicity to the liver parenchyma [131].

Clearance through the RES results from the removal of nanoparticles from the blood by phagocytic cells in the blood and tissues [132]. Examples of phagocytic cells of the RES include blood-circulating monocytes, hepatic Kupffer cells, splenic red-pulp and marginal zone macrophages, as well as bone marrow persinal macrophages and sinus endothelial cells [130]. Surface opsonization, where opsonins and other complement or immune proteins are deposited on the nanoparticle surface, mediate nanoparticle recognition and their clearance from the blood by the RES [1, 130]. Surface stabilization of nanoparticles with polyethylene glycol (PEG) represents the most popular and effective strategy to prevent surface opsonization via steric hindrance and improve blood circulation time of the nanoparticle [132]. Nanoparticles undergo intracellular degradation inside RES cells when phagocytosed, and if they cannot be broken by these intracellular processes they will remain within the cell and be retained by the body in mostly the spleen and liver [131, 133].

1.3.1 Parameters Affecting Nanoparticle Biodistribution

The chemical and physical properties of nanoparticles have a great effect on their cellular uptake, *in vivo* clearance, and biodistribution. The effect of nanoparticle size has been studied extensively and the general trend is that nanoparticles of size $30 - 50$ nm are best for cellular uptake by endocytosis as their ligand density is optimal to drive membrane wrapping while preventing depletion of local receptions [134]. Zhang *et al.* have reported that ultrasmall gold nanoparticles (diameters less than

5 nm) can enter cells and even the nucleus [9]. In vivo, nanoparticle size dictates tumour penetration and circulation time. There are many contradictory findings, but small nanoparticles (around 20 nm) have better tumour penetration, whereas large nanoparticles (100 nm) become trapped in the extracellular matrix after extravascating the blood vessel [134]. Nanoparticle surface charge is also an important physical factor in determining biodistribution as this affects the adsorption of opsonins and physical interaction with charged membranes and fenestrations. It has been found by Arvizo *et al.* that neutral and zwitterionic nanoparticles demonstrate longer circulation time via both intraperitoneal and intravenous administration, whereas negatively and positively charged nanoparticles have relatively shorter half-lives [135]. Nanoparticle surface charge also modulates their distribution, accumulation, and excretion. Nanoparticles with negative headgroups are more likely to be sequestered in the liver [135]. Negatively charged nanoparticles provide better systemic exposure than positively charged nanoparticles which are rapidly cleared [135]. The addition of targeting moieties on nanoparticle surfaces for active targeting can change the biodistribution of nanoparticles and is discussed later in greater detail. The geometry and shape of the nanoparticle can change the interaction of the nanoparticle with membranes, as well as its margination and tumour extravasation. It is possible to engineer nanoparticles into a variety of shapes and aspect ratios including spheres, rods, pyramids, stars, cages, plates, etc [136]. Some novel nanoparticle shapes include gold nanostarfruits [137], silver nanocarrots [138], silica nanomatryoshkas [139], and platinum multicore-cesium oxide shell nanopomegranates [140]. The shape of the

nanoparticle affects its binding affinity to ligands on a surface because flat nanoparticles support more numerous ligand interactions through greater surface contact, increased effective local concentration, and relieves conformational stresses imposed on ligands interacting between curved surfaces [141]. Molecular modelling of different shapes of nanoparticles interacting with cell membranes have shown that the shape affects both internalization rate and percentage [142, 143]. In vitro experiments of gold nanoparticles in HeLa cells confirm this shape-dependent effect, where uptake of nanorods is lower than nanospheres [144]. In the context of nanoparticle clearance by the RES, Champion *et al.* showed that particle shape plays a dominant role over size in macrophage phagocytosis [145]. Phagocytic cells are more adept at engulfing nanospheres due to their complete symmetry that requires less complex actin restructuring as opposed to nanoparticles with anisotropic presentation [145]. In the context of biodistribution and blood circulation, nanospheres are more likely to remain in the center of blood flow due to their more fluid dynamic isotropic shape; whereas nanorods are subject to torsional flow from their anisotropy and thus more likely to drift to vessel walls [146]. Computer simulations in microfluidic models confirm these margination effects and further suggest that increasing the aspect ratio of nanorods increases the adhesive forces between the nanoparticles and vessel walls [146, 147]. Smith *et al.* compared the tumour extravasation capability of spherical quantum dots and high-aspect ratio carbon nanotubes with similar zeta-potential, surface area, and surface modification against three different tumour types with different pore architectures [148]. Smith *et al.* reported that spherical nanoparticles undergo convective transport to extravasate into tumours, and is

therefore dictated by cut-off pore sizes [148]. On the other hand, high aspect-ratio nanoparticles can undergo slower diffusive transport to enter tumours with cut-off pore sizes smaller than their longest dimension (but still larger than their shortest dimension) [148]. Overall, nanorods have been shown to have longer circulation time in the blood due to reduced phagocytosis by macrophages and decreased elimination, which leads to more passive accumulation into solid tumours [149].

1.3.2 Methods of Determining Biodistribution

It is important to study the interaction of nanoparticles in *in vivo* biological systems such that a more accurate assessment of the relationship between physical and chemical properties of nanoparticles with their distribution, clearance, immunological responses, and metabolism can be achieved [150]. In typical biodistribution studies, nanoparticles are injected into test animals, which are subsequently sacrificed and have their organs harvested to perform elemental analysis [150]. In the context of gold nanoparticles, instrumental neutron activation analysis (INAA) and inductively coupled plasma-mass spectrometry (ICPMS) are the "gold" standards for accurately determining the concentration and localization of gold nanoparticles in animal tissues [151]. In ICPMS, the sample is nebulized by a plasma torch and converted to plasma prior to quantification by a mass spectrometer system [152]. The limit of detection for gold using ICPMS can reach 0.001 μg/kg, which is more than sufficient for an accurate quantitative analysis of gold nanoparticle distribution [151, 152]. This type of biodistribution analysis is problematic because it is an endpoint sampling method that is costly, time-consuming, and yields only bulk organ-level resolution. Furthermore, it cannot be translated into human clinical research easily. Histology,

autometallography, and electron microscopy (including scanning electron microscopy and transmission electron microscopy with energy dispersive x-ray spectroscopy and its variants) are qualitative techniques that can improve the biological resolution of localizing gold nanoparticles in tissues. However, these methods also suffer from similar drawbacks of the need to sacrifice animals and intensive sample preparation [151]. It is evident that there is a need to develop new methods to evaluate *in vivo* biodistribution of nanoparticles quantitatively in real-time.

In vivo optical and optoacoustic techniques have been suggested and developed to supplement these conventional biodistribution study methods [151]. Gold nanoparticles can be made to be inherently fluorescent without conjugation to fluorophores [153]. Reported quantum yields for these gold nanoparticles range from 10^{-6} to 10^{-2}, and depends on the choice of capping ligand and size of the gold nanoparticle core [153]. There have been numerous examples in the literature of using fluorescent nanoparticles for *in vivo* whole animal and excised organs imaging. Liu *et al.* used in situ fluorescence imaging of tumour-bearing nude mice to quantitatively determine the pharmacokinetics and passive tumour targeting effects of NIR-emitting glutathione-coated luminescent gold nanoparticles [154]. Sykes *et al.* demonstrated the use of noninvasive and rapid skin biopsies coupled with optical imaging to analyze gold nanoparticle and quantum dot exposure in animals [155]. Novel non-imaging methods of assisting with nanoparticle biodistribution studies include an automated dosing/blood sampling system designed and verified by Wang *et al.* that can be used with awake and freely moving rats that may be applicable for studying the blood circulation of nanoparticles [156, 157].

1.4 Targeting Strategies for Nanoparticle Drug Delivery

1.4.1 Passive Targeting and the EPR Effect

One of the most compelling reasons to use nanoparticle formulations of chemotherapeutic agents is the enhanced permeability and retention (EPR) effect, first described in 1986. The EPR effect causes nanoparticles to accumulate passively in tumors because of the leaky vasculature and impaired lymphatic drainage in cancers. This can make non-toxic nanoparticles effective passive carriers of chemotherapeutic agents that otherwise cause significant morbidity in non-target organs [158, 159, 160]. The EPR effect has been demonstrated in a variety of animal xenograft models and is the basis of action for drugs such as Doxil. However, the extent to which it is useful in human cancers remains not fully understood [161]. Attempts to correlate EPR effect with a single biomarker, such as vascular endothelial growth factor (VEGF), have not been successful. Many features of tumors, including interstitial pressure, components of the extracellular matrix, and perhaps even hormones such as estradiol, can determine the degree of EPR effect seen in each particular cancer [162, 163, 164]. Clinical imaging can demonstrate the degree of EPR seen in a specific cancer and aid in the prediction of nanomaterial accumulation on a case-by-case basis [165].

1.4.2 Active Targeting

Cancers overexpress a number of surface molecules. Some are related to the generally increased metabolism of malignant tissue, such as the folate receptors; others are specific to the cell type of origin, such as estrogen receptors. The first generation of receptor-targeted drugs aimed to inhibit cell growth by inhibiting the receptors. Molecular blockade of epidermal growth factor receptor (EGFR) has shown clinical

efficacy in skin, thyroid, colon, ovarian, non-small cell lung and breast cancer [166]. Recent pre-clinical and clinical studies have shown that the EGFR blockade can work synergistically with radiation therapy in all of the forms of cancer in which EGFR is overexpressed [167, 168, 169, 170]. Another common target is VEGF, which permits angiogenesis [171]. Drug-antibody conjugates may improve targeting of cytotoxic drugs as well as create synergy between receptor blockade and drug action. There are over a dozen antibody-drug conjugates (without nanoparticles) in clinical trials [172]. However, when nanoparticles are added, it is not clear whether specific targeting necessarily improves results over the EPR effect alone. The analysis of results is complicated by the fact that targeting may be improved in two ways: by increasing delivery to the bulk of the tumor as opposed to non-target organs, or by improving uptake by cells once the agent is in the tumor.

These effects are rarely studied together and may in fact be influenced in opposite directions. One study, using 50 nm Au particles, showed that targeting the particles with transferrin did not lead to increased uptake by the tumor tissues relative to the liver and other organs. However, there was increased cellular uptake by tumor cells overexpressing transferrin receptors, proportional to the degree of transferrin conjugation to the particles [173]. Although those particles were not therapeutic, later studies indicated that particles bearing paclitaxel were more effective against a human prostate cancer cell line (PC3) when they were conjugated to transferrin [174]. Apart from antibodies, transferrin, and folate, other targeting moieties include peptides and aptamers. Peptides are an appealing alternative to antibodies because they are less immunogenic and do not require humanization. They are also easy

to synthesize. Although stability is often an issue, it can be addressed by altering the sequence, using artificial amino acids, or cyclization. Peptides specific to certain receptors have been discovered using combinatorial techniques [175, 176]. Aptamers are also widely investigated for targeting [177]. One study reported nanoparticle conjugates to the A10 aptamer for targeting the prostate specific membrane antigen (PSMA); the same researchers later found that a single intratumoral injection reduced tumor size in xenografts of LNCaP prostate cancer cells [178, 179].

The jury remains out on the value of targeting nanoparticles to tumors, though given the failure of some tumors to demonstrate a robust EPR effect, some method of targeting will doubtless develop as nanoparticle agents move into the clinic. The issue of targeting metastases is also a key one, as methods for treating large, visible, highly vascularized tumors are different for those targeting small clusters of cells [180]. A thorough review of targeting schemes used for nanoparticles may be found elsewhere [181].

1.5 Motivation and Project Background

1.5.1 Melanoma

Melanoma is an aggressive form of skin cancer that is responsible for 75% of all skin-cancer associated deaths [182]. It is a malignant neoplasm of melanocytes, which are specialized epidermal cells that produce the melanin pigment to give skin its color and protect it from ultraviolet (UV) radiation damage [183]. The oncogenesis of melanoma has been associated with environmental risk factors such as UV radiation exposure, as well as host factors such as the number of melanocytic nevi, familial history, and the pigmentary-related susceptibility gene MC1R [184, 185]. In the early

stages of melanoma, the tumour develops radially or laterally within the epidermis, and gradually forms microscopic extensions to invade the superficial papillary dermis and grow vertically and ultimately metastasize throughout the body [183]. Primary melanoma can originate anywhere over the body, but it is most commonly found in the trunk or extremities [186]. The incidence of melanoma in the developed world has been increasing for the past 50 years, specifically in the United States the incidence has increased from 6.8 per 100,000 people in 1973 to 20.1 per 100,000 people from 2003−2007 [183, 185].

Melanoma is highly curable if diagnosed in the early stages where the tumour depth is less than 1 mm [185]. The standard strategy for melanoma treatment is wide margin surgical excision [183]. In cases where wide margins are not possible such as melanomas of the head and neck, Mohs micrographic surgery is also an option [183]. However, advanced metastatic melanoma cases have significantly poorer survival rates (median survival ≤ 1 year) [187]. Metastatic melanoma lacks satisfactory treatment strategies as it is extremely resistant to conventional DNA-damaging chemotherapeutics, such as dacarbazine, cisplatin, carmustine, and tamoxifen, by overexpression of DNA repair genes [188]. Though approved by the FDA in the late 1990s, other treatments such as interferon-α adjuvant therapy and interleukin-2 immunotherapy only marginally improve survival rates and remission [183, 189]. In the last decade, there has been a resurgence of new therapies and drug agents in clinical development for melanoma. Antibody blockade of cytotoxic T-Lymphocyte-associated antigen 4 (CTLA-4) by tremelimumab and ipilimumab serve to prevent T-cell deactivation and enhance melanoma immune responsiveness for patients with

metastatic melanoma [187, 189, 190]. New chemotherapeutic agents that inhibit the mitogen-activated protein kinase (MAPK) pathway such as dabrafenib are also being investigated in mono- or combinational therapies to inhibit the most frequently mutated BRAF oncogene present in 60-70% of melanoma cases [187, 190, 191].

Nanoparticle-based therapeutic approaches have made huge advances in melanoma treatment. Combinational therapy with multiple chemotherapeutic drugs can overcome multidrug resistance in tumours. Combined BRAF and MEK inhibition of the MAPK pathway in melanoma patients by dabrafenib and trametinib in combinational therapy was approved by the FDA in 2013 [192]. Nanoparticulate drug delivery systems can be used in these therapies as a platform to standardize pharmacokinetic properties of the combinatorial drugs, as well as determine the appropriate dosing and administration route [193]. Nanoparticles have also been used in melanoma treatment to improve the tolerance of conventional chemotherapeutic agents.

1.5.2 Peptide Guidance of Nanoparticles

There are five main stages of nanoparticle-based delivery systems for cancer therapy: blood circulation, tumour neovasculature, tumour penetration, tumour cell recognition, and organelle targeting [194]. There have been many strategies to conjugate different types of targeting moieties on nanoparticles to guide them through these stages, including amphiphilic polymers, polyethylene glycol coating, streptavidin-biotin systems, antibodies, affibodies, aptamers, and ligands [195]. Peptide guidance of nanoparticles is advantageous compared to other bioconjugation-based approaches because peptides have a higher binding affinity and specificity to receptors [194, 196]. Furthermore, it is possible to rationally combine peptide

sequences to form multi-targeting and multi-staging ligands. Agemy *et al.* ligated a mitochondrial localization peptide (CGKRK) with a proapoptotic peptide ($_D$[KLAKLAK]$_2$) and conjugated the combined peptide sequence onto iron oxide nanoworms for enhanced delivery and treatment of glioblastoma [197].

1.6 Project Goals and Specific Aims

The two main goals and respective specific aims of this project are:

1) To elucidate whether the EPR effect alone is sufficient for tumour targeting or active targeting moieties are necessary when using ultrasmall gold nanoparticles for drug delivery in melanoma treatment
   a) Synthesize and characterize ultrasmall, water-soluble gold nanoparticles functionalized with PEG and targeting peptides
   b) Evaluate and compare the *in vivo* biodistribution of gold nanoparticle conjugates in B16 melanoma tumour-bearing C57/BL6 mice using inductively coupled plasma mass spectrometry
2) To correlate the cellular uptake and *in vivo* biodistribution of the ultrasmall gold nanoparticles using a variety of imaging modalities *in vitro* and *in vivo*
   a) Evaluate the *in vitro* cellular uptake of ultrasmall gold nanoparticles in excised B16 melanoma tumours using environmental scanning electron microscopy (ESEM) and scanning transmission electron microscopy (STEM)
   b) Evaluate the *in vivo* biodistribution of ultrasmall gold nanoparticles in excised organs using photoacoustic and fluorescence imaging

CHAPTER 2
Materials and Methods

2.1 Synthesis and Functionalization of Gold Nanoparticles

2.1.1 Gold Nanoparticle Synthesis

Gold nanoparticle synthesis was performed as outlined in Zhang *et al.* [9]. 0.19 g of N-2-mercaptopropionylglycine (common name: tiopronin) and 280 μL of gold (III) chloride (wt. 30% in HCl) was added into a 250 mL round-bottom flask filled with solvent (2.85 mL of glacial acetic acid and 17.15 mL of methanol). By changing the ratio of gold atoms to tiopronin ligands, the size of synthesized gold nanoparticles can vary from 2.7 nm (tiopronin 3:1 Au) to 1.9 nm (tiopronin 5:1 Au). The flask was stirred in the fume hood until homogeneous for about 30 minutes and the solution changed to a pale yellow color. 0.3 g of sodium borohydrate was added to 7.5 mL of Milli-Q ultrapure water and mixed well before being slowly added to the round-bottom flask. The new solution became jet black in color and was continuously stirred for about 1 hour to become completely homogeneous The solvent was removed by rotary evaporation in a 40 °C water bath for approximately 1 hour. The dense solution was diluted to 15 mL by distilled water. The pH of the solution was adjusted to pH 1 by adding hydrochloric acid drop-wise. The solution was pipetted into dialysis tubing (cellulose membrane, molecular weight cut-off of 14 kDa) then dialyzed for 72 hours in 4 L of distilled water, changing water approximately every 12 hours. The gold nanoparticle solution was then filtered 3 times using a 3 kDa

centrifuge filter with distilled water. The concentration of the gold nanoparticle solution was determined by taking the optical density at 420 nm by a spectrometer in a cuvette and interpolating from a standard curve.

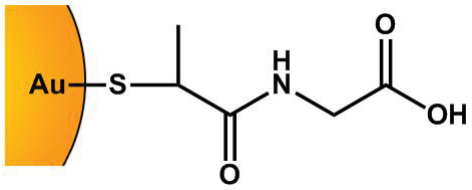

Figure 2–1: Schematic of tiopronin-capped gold nanoparticles

2.1.2 PEGylation of Gold Nanoparticles

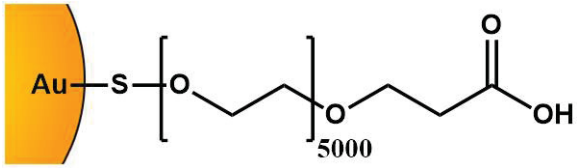

Figure 2–2: Schematic of Au-PEG-COOH nanoparticles

A ligand exchange reaction was used to functionalize tiopronin-capped gold nanoparticles with various types of bifunctional thiolated polyethylene glycol (PEG). It was previously determined by ICPMS that there are approximately 207 tiopronin ligands and 169 gold atoms per tiopronin-capped gold nanoparticle. PEG at a 4:1 ratio of PEG ligands to tiopronin ligands on gold nanoparticles was dissolved in dH_2O. Gold nanoparticles were subsequently added and stirred for 72 hours in a 10 mL glass vial at room temperature. The PEGylated gold nanoparticle solution was then filtered 3 times using a 10 kDa Millipore centrifuge filter at a temperature of 4 °C and speed of 8,000×g for 20 minutes. Filtered PEGylated gold nanoparticle

solution was stored at 4 °C. The concentration of the Au-PEG nanoparticle solution was determined by using

$$C_{Au}V_{Au} = C_{Au-PEG}V_{Au-PEG} \tag{2.1}$$

C_{Au} is the concentration of gold nanoparticles added at the beginning of the conjugation reaction. V_{Au} is the volume of gold nanoparticle solution added at the beginning of the conjugation reaction. C_{Au-PEG} is the unknown concentration of Au-PEG nanoparticles to be calculated. V_{Au-PEG} is the volume of Au-PEG nanoparticle solution after filtration.

2.1.3 Conjugation of Gold Nanoparticles with Doxorubicin

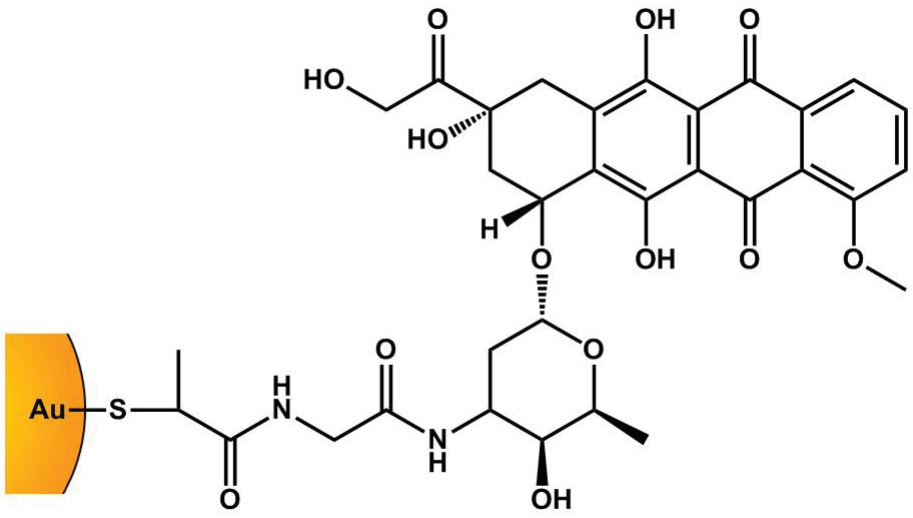

Figure 2–3: Schematic of Au-Dox nanoparticles

Doxorubicin was conjugated onto tiopronin-capped gold nanoparticles using carbodiimide crosslinker chemistry. In a typical reaction, tiopronin-capped gold nanoparticles, doxorubicin, and EDC at a molar ratio of 1:25:2500 were mixed in

1× PBS (pH 7.4). The conjugation reaction was performed in a 15 mL Falcon tube at room temperature and agitated on a shaker for 4 hours. Au-Dox nanoparticles were subsequently filtered with 1× PBS (pH 7.4) using a 10 kDa centrifuge filter at room temperature and speed of 8,000×g for 20 minutes.

2.1.4 Conjugation of Gold Nanoparticles with Peptides

Gold nanoparticles were further functionalized by peptide conjugation using carbodiimide crosslinker chemistry between the carboxyl group in tiopronin or SH-5KPEG-COOH ligands and the primary amine group of the N-terminus of the peptide or lysine residue in the peptide sequence. Typical Au-peptide conjugation reaction was carried out in 1× PBS (pH 7.4) or 1× borate buffer (pH 8) depending on the peptide by mixing Au nanoparticles or Au-PEG-COOH, peptide, EDC, and NHS at a molar ratio of 1:20:5000:10000. MSH and cRGD peptides dissolve readily in 1× PBS (pH 7.4). FREG peptide is acceptably dissolvable in 1× PBS (pH 7.4). Myx peptide is not soluble in 1× PBS (pH 7.4), acceptably soluble in 1× HBSS, and readily soluble in borate buffer (pH 8 or above). The conjugation reaction was performed in a 10 mL glass vial at room temperature inside a fume hood with stirring for 24 hours. Au-peptide or Au-PEG-peptide nanoparticles were subsequently filtered using a 3 kDa or 10 kDa centrifuge filter at room temperature and speed of 8,000×g for 20 minutes.

Targeting peptides used in this project and their corresponding physicochemical properties are summarized in Table 2–1. Schematics of some of the peptide-conjugated gold nanoparticles are shown in Figure 2–4.

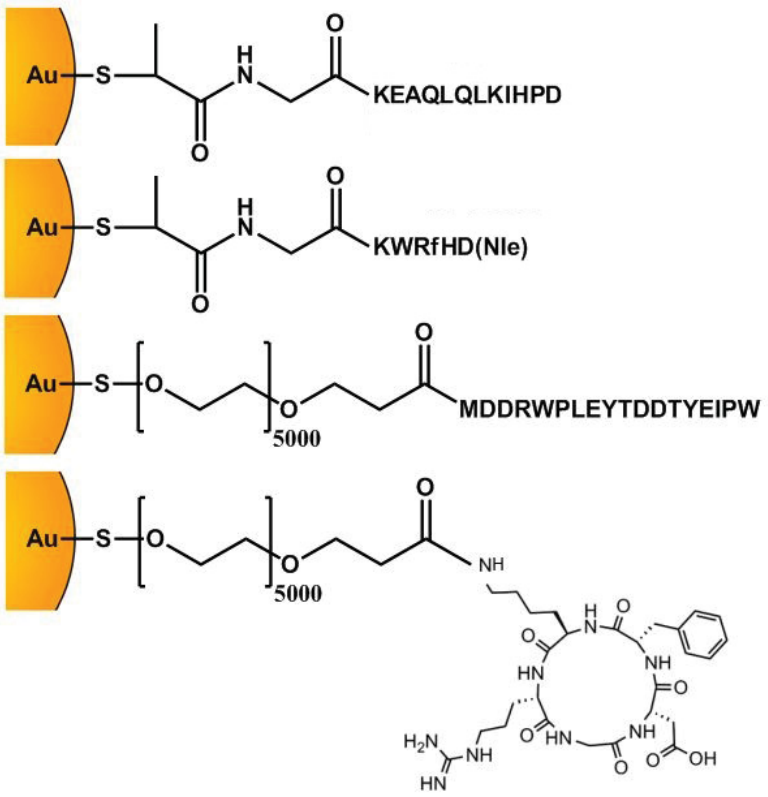

Figure 2–4: Schematic of possible products formed by conjugation between proposed peptides and gold nanoparticles. From top to bottom: Au-FREG, Au-MSH, Au-PEG-Myx, and Au-PEG-cRGD

2.2 Cell Culture

B16 murine melanoma cells were cultured with 10% fetal bovine serum and 1% penicillin-streptomycin supplemented Dulbecco's Modified Eagle Medium (DMEM). SK-MEL-28 human melanoma cells, BJ-1 human skin fibroblasts, and H1299 human non-small cell lung carcinoma cells were cultured with 10% fetal bovine serum and 1% penicillin-streptomycin supplemented Roswell Park Memorial Institute medium (RPMI). All cell lines were cultured on tissue culture dishes at 37 °C and 5% CO_2 atmospheric environment and passaged as necessary.

Table 2–1: Targeting Peptides Used in this Project

Peptide	**Sequence** (N-terminal to C-terminal)	**Molecular Weight** (g/mol)	**Charge**	**Molecular Target**
FREG	KEAQLQLKIHPD	1419.63	+1	FGF-2
MSH	KWRfHD(Nle)	1001.15	+2	Melanocortin receptor type-1
Myx	MDDRWPLEYTDDTYEIPW	2345.55	−5	Akt
cRGD	cyclic(RGDfK)	603.7	+1	$\alpha_\nu\beta_3$ integrins

2.3 Mouse Models of Cancer

2.3.1 Induction of B16 tumours in C57/BL6 mice

A few days prior to tumour induction, the right flank of C57/BL6 mice were shaved with a razor. On the day of tumour induction, C57/BL6 mice were injected subcutaneously in the right flank with 200 μL of B16 cells at a concentration of 5×10^6 cells/mL. The tumour growth was monitored and measured every 2-3 days. Animals were euthanized when the tumour volume exceeds 2 cc. To sacrifice animals, the mice were transferred to a transport cage and euthanized by carbon dioxide asphyxiation as per animal handling protocol.

2.3.2 Induction of Lewis lung carcinomas in C57/BL6 mice

Lewis carcinoma-bearing C57/BL6 mice were induced by Andrew Heinmiller from VisualSonics Inc. (Toronto, ON). Fixated samples from Lewis carcinoma-bearing C57/BL6 mice for experiments were obtained as gifts from Andrew Heinmiller.

2.4 Transmission Electron Microscopy

2.4.1 Sample Preparation

For nanoparticle samples, a droplet of nanoparticle solution was pipetted onto PELCO carbon type B on 200 copper mesh transmission electron microscopy grids (model number 01811) and left to air dry.

Tumours were fixed in 2.5% (v/v) EM-grade glutaraldehyde at 4 °C for 12 hours. Tumours were then cut into approximately 1 mm × 1 mm cross-sectional pieces using a sterile razor blade. For staining, pieces were first placed into a glass test tubes and immersed in 2% osmium tetroxide solution for 1 hour and washed three times with MilliQ water. Pieces were further stained with 2% uranyl acetate for 1 hour and washed three times with MilliQ water. Subsequently, the pieces were immersed for 15 minutes in 25%, 50%, 75%, and 100% ethanol solution sequentially for dehydration. For embedding, the pieces were immersed for 15 minutes in 100% ethanol; 50% ethanol, 50% acetone; and 100% acetone solution sequentially. The pieces were then immersed in 50% acetone, 50% resin solution at 4 °C overnight. Next, the pieces were embedded with 100% resin solution in TEM blocks and placed in a 60 °C oven to cure overnight. Resin solution is prepared from PELCO Eponate 12^{TM}Kit, specifically a mixture of 9.136 mL Eponate-12 resin, 6.142 mL dodecenyl

succinic anhydride (DDSA), 4.415 mL nadic methyl anhydride (NMA), and 0.31 mL tris(dimethylaminomehtyl)phenol (DMP-30).

For thin sectioning, blocks were trimmed and leveled with a sterile razor blade to expose the embedded sample. The block was secured with an Allen clamp onto a MT-X Ultramicrotome and thin sectioned into 90 nm thick slices with a 45 ° Diatome diamond knife. 2 or 3 thin sections were dabbed onto PELCO carbon type B on 200 copper mesh transmission electron microscopy grids (model number 01811).

2.4.2 Imaging procedures

Biological samples were imaged at the Micro-Environmental Imaging & Analysis Facility at the University of California - Santa Barbara with the FEI Co. XL30 environmental scanning electron microscope operating in various modes with different detectors. For ESEM of whole tumour samples, the gaseous secondary electron detector was used. For STEM of tumour thin sections, the scanning transmission electron microscopy detector was used instead in conjunction with a Bruker energy-dispersive spectrometer for X-ray microanalysis.

2.5 Characterization of Gold Nanoparticles

2.5.1 Fluorescence Measurement

200 μL of 17.5 μL gold nanoparticles was pipetted into a black-bottom 96-well microplate. Molecular Devices i3 multi-mode microplate reader and SoftMax® Pro software was used to measure and generate the excitation vs. emission heat map.

2.5.2 Zeta Potential Measurement

Zeta potential of gold nanoparticle conjugates were measured with Brookhaven Instruments Corporation zetaPALS apparatus. 1.3 mL of Au-conjugates at an approximately concentration of 1 μM in 1 $\times$ PBS (pH 7.4) was pipetted into a cuvette and inserted into the apparatus. The measurement was made using the "water" setting and averaged over 10 runs.

2.5.3 Gel Shift Assay

0.5 g of agar powder was dissolved in 50 mL of 1$\times$ TAE buffer and poured slowly into a gel tray enclosed by gel casting gates. Subsequently, a fixed height comb was placed into the comb slot close to one side of the gel tray. The agarose solution was left to cool and solidify for approximately 30 minutes at room temperature on a flat surface. The comb and gel casting gates were removed, and the gel tray with the agarose gel was placed into the gel electrophoresis apparatus in the orientation such that the wells were closest to the anode of the apparatus. The apparatus was filled with 1$\times$ TAE buffer until the gel is beneath 5 mm of liquid. 20 μL of gold nanoparticle conjugates were loaded into the wells of the gel using a pipette. The apparatus was run at 10 V/cm for approximately 45 minutes at steady current. The gel was subsequently imaged using a white light transilluminator to visualize the bands and photographed using a Canon EOS 600D digital single-lens reflex camera.

2.6 Toxicity of Gold Nanoparticle Conjugates and Peptide Ligands

2.6.1 Sulforhodamine B colometric assay

Cells were plated on 96-well cell culture plate and incubated at 37 °C in 5% CO_2 for the required incubation period. The medium was subsequently removed and

the cells were incubated with the approximate stimulus (nanoparticles, nanoparticle conjugates, peptides, or small molecular drugs) for the required incubation period. Cells were fixed with an effective concentration of 10% (wt/vol) trichloroacetic acid (TCA) overnight at 4 °C. The culture medium was discarded and the wells were rinsed 4 times with tap water, shaken vigorously to remove residual water, and left to air-dry in a fume hood. 100 μL of sulforhodamine B (SRB) stain (0.057% SRB powder in 1% acetic acid) was added into each well, and incubated for 30 minutes at room temperature protected from light with aluminum foil. Cells were washed 4 times with 1% acetic acid using a squirt bottle, shaken vigorously to remove residual acetic acid and left to air-dry in a fume hood. 100 μL of 10 mM Tris-base un-buffered (pH 8.4) was added to each well and the plate was agitated on a rocker until the stain completely dissolves. The optical density of wells was read at 510 nm on a plate reader.

2.7 Confocal Imaging of Gold Nanoparticle Conjugates in Cells

Cells were plated onto glass-bottom dishes at a low concentration (approximately 75,000 cells/mL). Approximately 2 μM of fluorescent Au-conjugates or fluorescent peptide were added to the cell culture directly and left to incubate for 3 hours or 24 hours at 37 °C and 5% CO_2 atmosphere. 1 hour prior to imaging, the dishes were washed with 1× PBS (pH 7.4), and the media was replaced with 25 nM LysoTracker Red solution in OptiMEM. Immediately prior to imaging, the OptiMEM solution was replaced with 1× PBS (pH 7.4) during imaging. Cells were imaged on ZEISS LSM 510 META with 488 nm laser excitation for FAM fluorescence and 543 nm laser

excitation for LysoTracker Red; 500-530 BP filter was used for FAM fluorescence emission, and 560 LP filter was used for LysoTracker Red fluorescence emission.

2.8 Biodistribution of Gold Nanoparticle Conjugates

2.8.1 Sample preparation for inductively coupled plasma mass spectroscopy

250 μL of 10 μM gold nanoparticle conjugates were injected into the tail veins of mice after warming mice with a heat lamp. Mice were given water and food *ad libitum* for 1 h or 24 h depending on the sample group and experiment prior to sacrificing. To sacrifice animals, the mice were transferred to a transport cage and euthanized by carbon dioxide asphyxiation as per animal handling protocol. Urine was collected into a weighing boat before and during asphyxiation by massaging the lower abdomen of the mouse gently. Blood was collected in EDTA-coated microtubes by cardiac puncture with a needle. The following organs were collected into sterile polystyrene tubes: heart, lungs, liver, spleen, pancreas, kidneys, tumour, left flank muscle, and brain. Harvested organs and bodily fluids were stored at $-20\,^{\circ}$C. Harvested organs were weighed (while frozen) and their masses were recorded. The organs and bodily fluids were placed into individual glass tubes. Approximately 2 - 3 mL of *aqua regia* (nitric acid and hydrochloric acid at a volumetric ratio of 1:3) was directly added into each glass tube for organ digestion. *Aqua regia* is extremely corrosive and should be handled with the utmost care and only in a well-ventilated fume hood. The glass tubes with organs and *aqua regia* were put into a Styrofoam holder and into a 55 °C warm water bath inside the fume hood. When there was no more solid bits floating in the tube and no more bubbling, the heat was turned up to 95 °C to allow the remaining acid to boil off. This entire process took up to 5 hours. Once there was

no more liquid, the tubes were removed from the water bath and allowed to cool. 10 mL of 1% nitric acid and 1% hydrochloric acid in MilliQ water was added into each tube to collect all non-biological remnants into 15 mL tubes. Digested samples were stored at $-20\,^{\circ}\mathrm{C}$.

2.8.2 Inductively coupled plasma mass spectroscopy

Germanium in 1% nitric acid and 1% hydrochloric acid was added to all samples as an internal standard at 10 ppb for ICPMS. Germanium was chosen as the internal standard element due to its rarity in biological samples, low detection limit by ICPMS (1 - 10 ppt), and low probability of a contaminant in our laboratory space. Well-mixed samples were loaded into the autosampler racks and analyzed using the Thermo Scientific iCAP Q ICPMS apparatus. Glass Expansion (Pocasset, MA) nickel/copper base sampler cone and nickel skimmer cone with insert were used. Sample uptake time of 30 seconds and wash time of 60 s was used. Gold standards at 0.1, 1, 10, 50, 100, and 500 ppb were used to generate a standard curves for each set of organs. Counts of ^{197}Au were normalized to the average counts of ^{72}Ge from the standards.

2.8.3 In vivo fluorescence imaging

Excised mouse organs from Lewis lung carcinoma-bearing C57/BL6 mice were imaged using the IVIS Spectrum imaging apparatus and associated Living Image® software in fluorescent mode with fluorescent lamp level set to high. The 675 nm excitation and 780 nm emission filters were used for optimal signal generation from the injected gold nanoparticles. The exposure time was adjusted such that the resultant images had a signal between 600 to 60,000 counts. Autofluorescence from

organs was subtracted from images using control non-injected organs as a reference. ROIs within each sample were generated using the automatic software function and compared.

2.8.4 Photoacoustic Imaging

For photoacoustic imaging, the excised organs from Lewis lung carcinoma-bearing C57/BL6 mice were embedded in ultrasound transmission gel and imaged using the VevoLAZR photoacoustic imaging system. Spleens, kidneys, livers, and tumours were imaged with "Spectro mode" (images at multiple wavelengths from 680 to 970 nm). Regions of interest within each sample were drawn and spectral curves (photoacoustic signal vs wavelength) were generated and compared. Based on differing spectral properties, spectral unmixing was performed to distinguish two "components" in each image. Spectrally unmixed images show with high resolution the location and relative amount of each component within the sample.

2.9 Solutions and Reagents

Peptides were purchased from Bio Basics Inc. (Markham, ON) at more than 95% purity as confirmed by HPLC. Carboxymethyl-PEG-Thiol (molecular weight 5 kDa) was purchased from Lysan Bio Inc. (Arab, AL). All cell media and associated supplements were purchased from Wisent Bioproducts Inc. (Saint-Bruno-de-Montarville, QC). LysoTracker Red was purchased from Life Technologies (Burlington, ON). TEM embedding resin kit was purchased from Ted Pella, Inc. (Redding, CA). TraceMetal^{TM} grade nitric acid and hydrochloric acid for ICPMS analysis were

purchased from Thermo Fisher Scientific Inc. Gold and germanium ICPMS standards were purchased from SCP Science (Baie D'Urfé, QC). All other chemical solutions and reagents were purchased from Sigma-Aldrich and used as delivered unless otherwise stated.

CHAPTER 3
Peptide-Guided Nanosystems for Optimizing the EPR Effect: Results and Discussion

3.1 Peptide-based Melanoma Targeting Strategies

A total of four types of peptides (FREG, MSH, myxoma, and cRGD) were used in this project as targeting moieties bioconjugated to gold nanoparticles to investigate the EPR effect.

FGF-2, also known as basic fibroblast growth factor (bFGF), is a protein that induces fibroblast growth factor receptors (FGFRs) to dimerize and activate their kinase activity to achieve physiological responses [198]. FGF-2 and its corresponding FGFR1 receptor have been found to be strongly expressed in primary melanomas and the FGF/FGFR/ERK and FGF/FGFR/PDGF-Rα pathways have been suggested to be viable targets for controlling melanoma progression [199, 200]. FGF-2 plays an important role in the melanoma tumour microenvironment as its production is essential to initiate melanomagenesis and maintain the malignant phenotype [201]. Facchiano *et al.* reported that the FGF-2-derived peptide - FREG was able to specifically inhibit FGF-2 induced proliferation, migration, and angiogenesis [202]. Aguzzi *et al.* further found that FREG-peptide inhibits melanoma growth *in vitro* and melanoma metastasis development *in vivo* in a mouse melanoma model [199]. As such, FREG-peptide was selected to be conjugated to gold nanoparticles in this

project as an active targeting moiety to ameliorate the malignant tumour microenvironment by preventing FGFR dimerization. An inherent advantage in therapeutic targeting of the tumour microenvironment is that the target molecule is typically involved in multiple signaling pathways or cell types, such that its blockage can have an effect on the primary tumour as well as prevent the development of secondary tumours [203].

αMSH (alpha melanocyte stimulating hormone) is a 13-amino acid long peptide hormone secreted by the pituitary gland whose primary function is melanogenesis, which is the process of skin pigmentation [204, 205]. Sawyer *et al.* reported the synthesis of an αMSH analog with a norleucine substitution in position 4 and a D-phenylalanine substitution in position 7 that is a strong agonist of the melanocortin type-1 receptor [204, 206]. The high affinity of the peptide analog to its receptor suggests that it can be an effective active targeting moiety for melanoma, as more than 80% of human melanoma tumour samples from metastatic melanoma patients express melanocortin type-1 receptors [205, 206, 207]. In fact, there have been numerous instances in the literature reporting the use of the αMSH analog peptide for tumour targeting. Chen *et al.* demonstrated the use of ^{99m}technetium-labelled αMSH peptide as a radiolabel to diagnose melanoma [205]. Lu *et al.* developed αMSH-peptide conjugated hollow gold nanospheres for use as melanoma-targeting agents for photothermal ablation [206]. In addition to being an excellent targeting moiety, it has been reported that αMSH can protect malignant melanocytes from the proinflammatory effects of TNF-α by suppressing melanoma cell attachment, invasion, and integrin expression [208].

Myxoma is a rabbit-specific poxvirus that causes lethal myxomatosis [209]. Interestingly, myxoma virus is unable to cause disease in other mammals (including humans), yet it is effective at infecting and killing around 70% of all human cancer cell lines, including gliomas and melanoma [209, 210]. The ability of the myxoma virus to replicate in human cancer cells is related to the NM-T5 viral ankyrin-repeat protein, which specifically targets the serine/threonine kinase Akt [209, 210]. NM-T5 binds to Akt, which is overexpressed and dysregulated in a wide variety of human cancers, and promotes its phosphorylation and activation to affect cell survival, proliferation, and cell death [209, 210]. Stanford *et al.* have shown that the myxoma virus can be used as an oncolytic virus against primary and metastatic B16F10 mouse tumours *in vivo* with minimal side effects [211]. Istivan *et al.* developed a short therapeutic peptide from the myxoma virus using the resonant recognition model (RRM) with high specificity and apoptotic activity against B16 melanoma cancer cells while sparing normal cells [210, 212].

RGD (arginine-glycine-aspartic acid) is a tripeptide sequence that was initially identified in the 1980s in fibronectin to be responsible for cellular recognition and adhesion [213]. Since then, the RGD sequence has been found in a wide variety of extracellular matrix components that are recognized by integrins on endothelial cells [214]. The $\alpha_\nu\beta_3$ integrin is an important cancer therapeutic target as it is essential for tumour angiogenesis and metastasis [215]. $\alpha_\nu\beta_3$ integrins are overexpressed in invasive tumour cells (including glioblastoma, melanoma, breast, ovarian, and prostate cancers) and the accompanying tumour neovasculature, but not in the healthy non-dividing endothelium and normal tissues [215]. As most cancers induce and sustain

neoangiogenesis to maintain their overproliferation, there is an abundance of tumour endothelial cells in the neovasculature surrounding the tumour for RGD peptides to target [216]. The cyclic forms of the RGD-sequence-containing short peptides, such as the cyclo(Arg-Gly-Asp-(D-Phe)-Lys) used in this project, have greater affinity for $\alpha_\nu\beta_3$ integrins, and as such have better tumour-targeting properties than their linear counterparts [217]. Dubey *et al.* have demonstrated the use of cyclic RGD-peptides on liposomes for drug delivery to angiogenic tumours [218]. Gormley *et al.* have evaluated the use of cyclic RGD-gold nanorod conjugates to selectively target prostate tumours for localized photothermal therapy [217]. Similar to peptides discussed previously, in addition to its role as a targeting moiety, cyclic RGD-peptide has been therapeutically implicated in the inhibition of its target $\alpha_\nu\beta_3$ integrins to reduce angiogenesis, tumour progression, and metastasis [214, 218].

3.2 Characterization of Gold Nanoparticles Conjugates

3.2.1 Optimizing Conjugation Conditions and Efficiency

To determine the optimal bioconjugation reaction, gel shift assays were performed on conjugates made with varying molar ratios of Au-PEG-COOH nanoparticles and EDC, while maintaining the same molar ratio of 1 Au-PEG-COOH to 20 peptides and 1 EDC to 2 NHS. In gel shift assays, gel electrophoresis is used to detect the change in electrophoretic mobility of the nanoparticles as a result of increased hydrodynamic size and altered charge from bioconjugation of various moieties onto the particle surface [219]. The optimization of molar ratios used in nanoparticle carbodiimide crosslinker-based conjugation is necessary to form robust, colloidally stable, and monodisperse peptide-coated nanoparticles [219, 220]. If too

much crosslinker is used, the EDC and NHS promotes the polymerization between peptides, thus preventing their proper conjugation to the gold nanoparticles [219]. A representative gel shift assay is shown in Figure 3–1 for the myxoma peptide. As the ratio of EDC to Au-PEG-COOH increased, the distance travelled by the conjugates decreased. The band shift distance achieved its maximum value at the EDC/Au-PEG-COOH ratio of 5000, and remained at a similar shift distance when the ratio was 10000. The result suggests that a higher conjugation efficiency, where more peptides become attached to the nanoparticle, was achieved with an increasing amount of EDC, but only up to a ratio of approximately 5000 to Au-PEG-COOH. As such, a ratio of 1 nanoparticle : 20 peptides : 5000 EDC : 10000 NHS was selected to be used in bioconjugation of nanoparticles throughout all experiments.

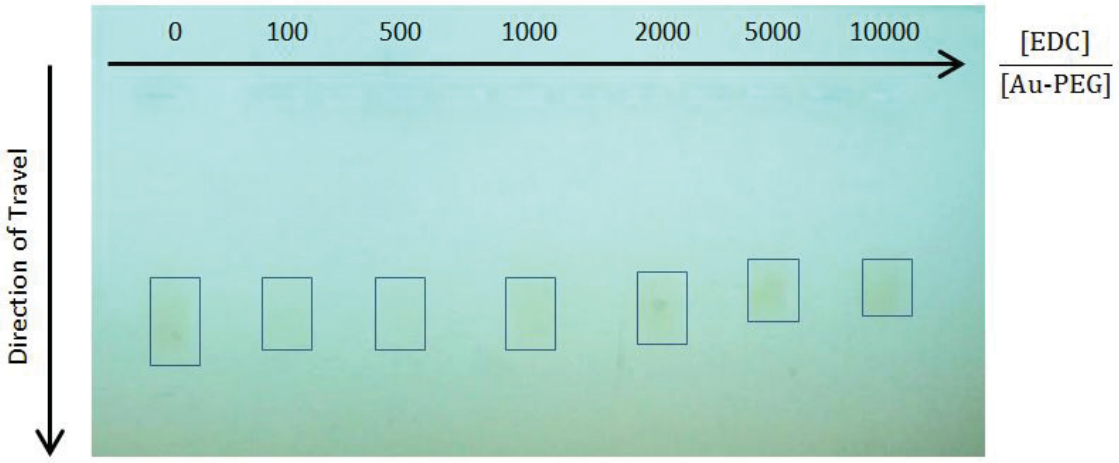

Figure 3–1: Representative gel shift assay of Au-PEG-Myx nanoparticles conjugated with varying ratios of EDC to Au-PEG-COOH nanoparticles. Boxes indicate the location and thickness of bands obtained per conjugation reaction. EDC to Au-PEG-COOH nanoparticle ratio of 5000 or above yields the greatest band shift.

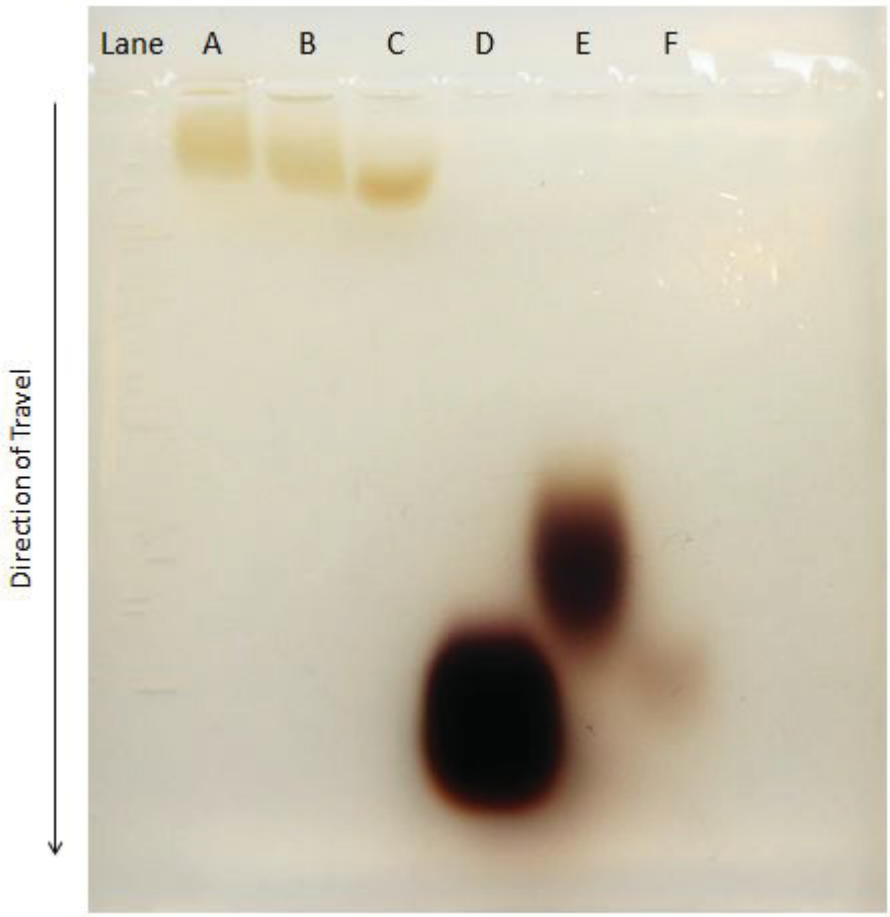

Figure 3–2: Gel shift assay of gold nanoparticle conjugates with Au-PEG-cRGD in lane A, Au-PEG-Myx in lane B, Au-PEG-COOH in lane C, tiopronin-capped Au in lane D, Au-Myx in lane E, and Au-cRGD in lane F.

Gel shift assay was performed on tiopronin-capped Au, Au-PEG-COOH, Au-Myx, Au-PEG-Myx, Au-cRGD, and Au-PEG-cRGD nanoparticles as shown in Figure 3–2. Non-PEGylated gold nanoparticles (lane D-F) travelled further down the gel than

their PEGylated counterparts (lane A-C), which suggest that the ligand exchange reaction between tiopronin and SH-5KPEG-COOH was successful. The significant difference in electrophoretic mobility between PEGylated and non-PEGylated nanoparticles can be mainly attributed to the increase in hydrodynamic radius due to the 5 kDa mass of each PEG molecule as compared to the 163 Da mass of each tiopronin molecule. Among the non-PEGylated gold nanoparticles, tiopronin-capped gold nanoparticles (lane D) travelled the furthest, followed by Au-cRGD (lane F), and Au-Myx (lane E) travelled the least distance. Au-cRGD and Au-Myx both had less electrophoretic mobility than tiopronin-capped gold nanoparticles, which indicates that the peptide was successfully conjugated to the nanoparticles. The reason that Au-cRGD travelled further than Au-Myx is most likely because of the smaller mass of cRGD-peptide as compared to myxoma-peptide. Among the PEGylated gold nanoparticles, Au-PEG-COOH (lane C) travelled the furthest, followed by Au-PEG-Myx (lane B), and Au-PEG-cRGD (lane A) travelled the least distance. Au-PEG-Myx an Au-PEG-cRGD both had less electrophoretic mobility than Au-PEG-COOH, which shows that the peptide was successfully conjugated to the nanoparticles. However, the mobility trend of Au-PEG-Myx travelling further than Au-PEG-cRGD cannot be explained by peptide mass since myxoma-peptide is more massive than cRGD-peptide. In this case, it is possible that there were more cRGD-peptides conjugated onto the Au-PEG-COOH nanoparticles than myxoma-peptides so the total hydrodynamic radius of Au-PEG-cRGD was less than that of Au-PEG-Myx. The gel shift assay for nanoparticles is primarily a mobility assay based on size, albeit the charge of the nanoparticle also contributes to the electrophoretic mobility

of the nanoparticle [221]. Since cRGD-peptide has a charge of +1, as the number of cRGD-peptides conjugated to the gold nanoparticle increases, the distance travelled towards the anode of the gel increases as well.

3.2.2 Quantification of Conjugation

To further confirm and quantify the bioconjugation of nanoparticles, zeta potential measurements were performed. The zeta potential of the gold nanoparticle conjugates was measured to investigate the electrical charge characteristics of the nanoparticles, as well as to gain an idea about their colloidal stability. The zeta potential of tiopronin-capped gold nanoparticles was measured to be -16.79 ± 1.94 mV. Ligand exchange of the tiopronin with PEG-COOH ligands decreased the zeta potential significantly ($p = 0.0083$) to -42.33 ± 8.39 mV, which can be attributed to increased colloidal stability from the high hydrophilicity of the corona and reduced aggregation from steric repulsion between particles [222, 223]. The increase in the standard error of the mean in the zeta potential measurement for Au-PEG-COOH suggests that there was increased polydispersity in the number of PEG ligands on each nanoparticle. Conjugation of myxoma peptide to tiopronin-capped gold nanoparticles decreased the zeta potential slightly to -22.10 ± 3.55 mV due

Table 3–1: Zeta Potential Measurements of Au-Conjugates

Au-Conjugate	**Zeta Potential (mV)**
Au@Tiopronin	-16.79 ± 1.94
Au-PEG-COOH	-42.33 ± 8.39
Au-Myx	-22.10 ± 3.55
Au-PEG-Myx	-25.56 ± 4.10
Au-cRGD	-16.58 ± 4.57
Au-PEG-cRGD	-18.40 ± 4.64

to the acidic nature of the myxoma peptide, with an isoelectric point of 3.51 and a negative charge of −5 at pH 7.4. On the other hand, conjugation of cRGD peptide to tiopronin-capped gold nanoparticles caused essentially no change to the zeta potential due to the peptide's high isoelectric point of 9.71 and +1 positive charge at pH 7.4. Au-PEG-Myx and Au-PEG-cRGD nanoparticles had zeta potentials of -25.56 ± 4.10 mV and -18.40 ± 4.64 mV respectively, which is not statistically different from their non-PEGylated counterparts. Among all the nanoparticle conjugates, Au-PEG-COOH had the greatest colloidal stability due to its high (magnitude) zeta potential. The other nanoparticle conjugates had acceptable stability and did not coagulate or flocculate up to 1 month when stored at 4 °C.

3.3 In vitro Experiments of Gold Nanoparticle Conjugates

3.3.1 Toxicity of Gold Nanoparticle Conjugates and Peptide Ligands

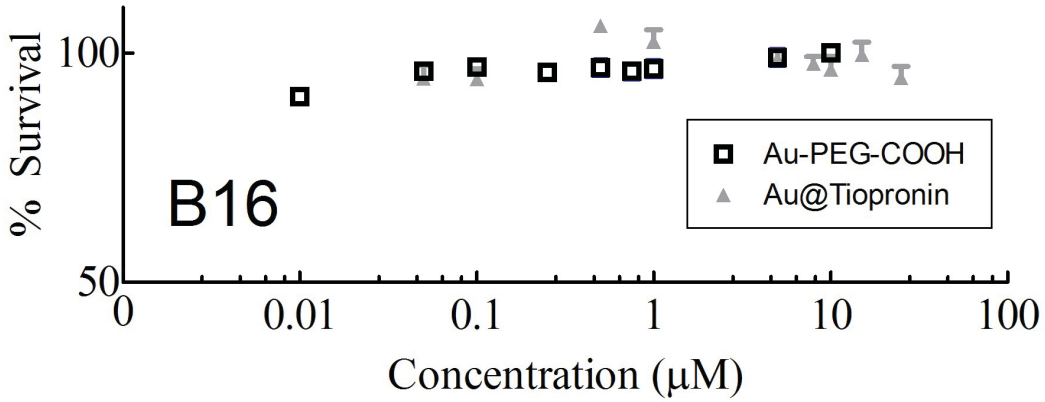

Figure 3–3: In vitro toxicity of Au and Au-PEG-COOH nanoparticles to B16 melanoma cells by sulforhodamine B (SRB) assay (shown as mean ± SEM with n=6).

In vitro toxicity of Au and Au-PEG on B16 melanoma cells was performed using the SRB assay, with the cell survival curves shown in Figure 3–3. No decrease in cell viability was observed for all concentrations of Au or Au-PEG-COOH nanoparticles up to 50 μM after 24 hours of incubation, which is well above the concentrations used in this project. This suggests that Au and Au-PEG-COOH nanoparticles are inherently non-toxic.

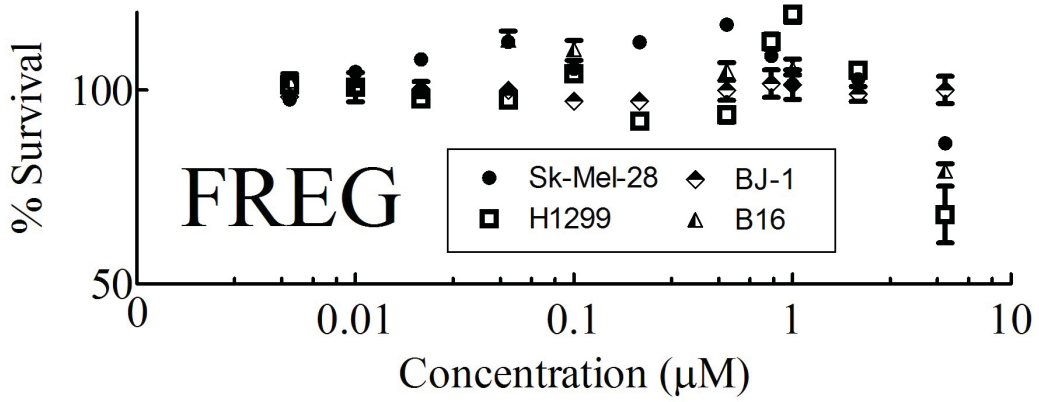

Figure 3–4: In vitro toxicity of FREG peptide to B16 murine melanoma cells, SK-MEL-28 human melanoma cells, H1299 human non-small cell lung carcinoma, and BJ-1 human skin fibroblasts by sulforhodamine B (SRB) assay (shown as mean ± SEM with n=6).

The SRB assay was also used to determine the toxicity of the peptides used in this project. For FREG-peptide, no decrease in cell viability was observed for peptide concentrations up to 1 μM in all tested cell types as shown in Figure 3–4. There was some decrease in cell viability at 5 μM for SK-MEL-28 human melanoma cells, B16 murine melanoma cells, and H1299 human lung cancer cells. However,

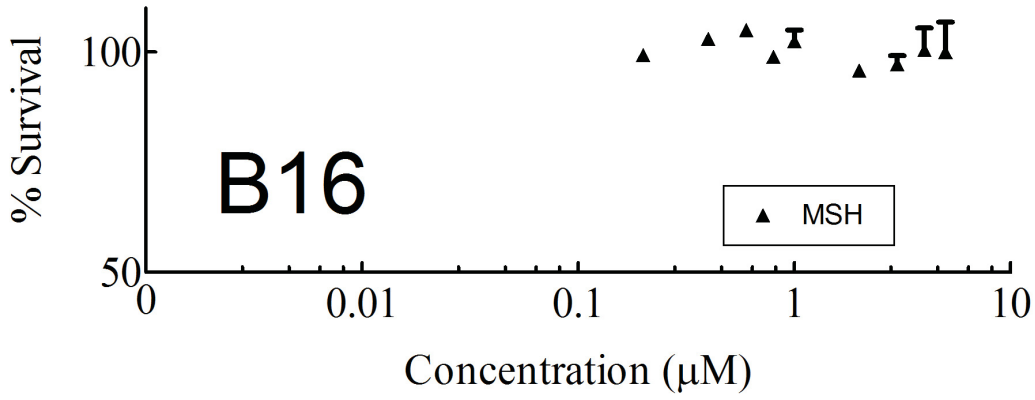

Figure 3–5: In vitro toxicity of MSH peptide to B16 melanoma cells by sulforhodamine B (SRB) assay (shown as mean ± SEM with n=6).

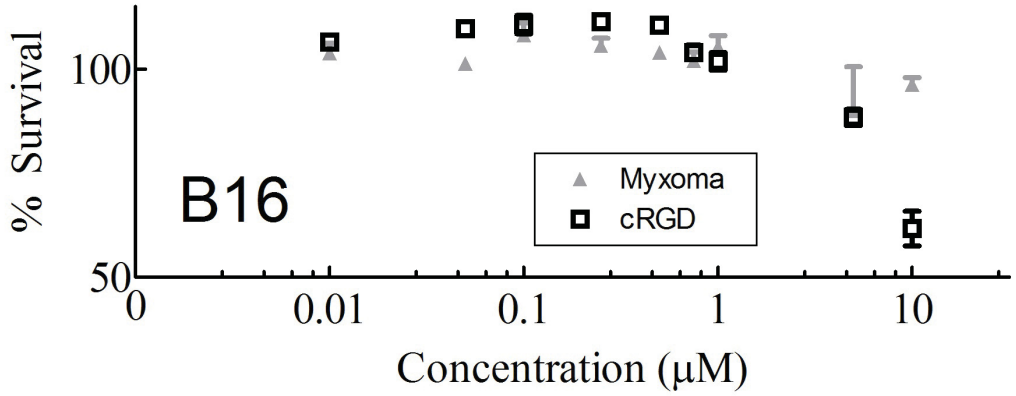

Figure 3–6: In vitro toxicity of Myxoma and cRGD peptides to B16 melanoma cells by sulforhodamine B (SRB) assay (shown as mean ± SEM with n=6).

inhibitor response curves could not be well fit to the data. The experimental toxicity results disagreed with the IC_{50} values reported by Facchiano *et al.* and Aguzzi *et al.* [199, 202]. For MSH-peptide, as expected, no decrease in cell viability was

observed in B16 melanoma cells up to 5 μM as shown in Figure 3–5. For cRGD-peptide, decrease in cell viability was only observed in B16 melanoma cells at 10 μM after 24 h as shown in Figure 3–6. The SRB assay results call into question the antitumoural properties of the FREG-peptide and myxoma-peptide as reported in the literature. However, this may be due to an insufficient incubation time, poor selection of the 24 h time point, as well as differences in the type of toxicity assay used. It is suggested that further toxicity studies be done using image-based real-time growth curves to ascertain the dynamics of the purported cytotoxicity of the selected peptides.

3.3.2 Determining Uptake of Gold Nanoparticle Conjugates

Tiopronin-capped gold nanoparticles have been previously shown to enter cell nuclei spontaneously [9]. To determine if conjugation of targeting peptides to the gold nanoparticles would affect their ability to be taken up into cells, fluorescein-labelled FREG-peptide (FAM-FREG, emission wavelength: 520 nm) was conjugated to gold nanoparticles and used in confocal imaging of B16 cells after 24 h of incubation, as shown in Figure 3–7. LysoTracker Red (emission wavelength: 590 nm) was used to label lysosomes. In panel A, FAM-FREG peptide alone was unable to enter the cell nucleus (outlined by the dotted white line) as there is no green fluorescence in the central region of the cells. In panel B, Au-FAM-FREG nanoparticles co-localized with LysoTracker inside the cell as the green and red fluorescence signals overlapped, suggesting that the conjugates were taken up into the cell by endocytosis. Furthermore, there was green fluorescence signal inside the cell interior, which demonstrates that FREG-peptide did not alter the ability of gold nanoparticles to be taken up

into B16 melanoma cells. A stack of confocal images of Au-FAM-FREG in cells was recorded and rendered in 3D as shown in panel C, there was no fluorescence observed in the central region of the cell, which indicated that the Au-FAM-FREG did not enter into the cell nucleus.

A similar experiment was performed with fluorescein-labelled MSH-peptide (FAM-MSH) and FAM-MSH-conjugated gold nanoparticles (Au-FAM-MSH) after 3 hours and 24 hours of incubation as shown in Figure 3–8. In panel A, FAM-MSH peptide localized in the B16 cytoplasm and not in the nucleus. In panel B, there was essentially no green fluorescence inside the cells. This suggests that FAM-MSH peptide was quickly taken up by cells within 3 hours, but was quickly degraded by the cells by the 24 hour time point. The FAM-MSH peptide also cannot enter into the nucleus alone. In panel C, there was essentially no green fluorescence inside the cells. In panel D, green fluorescence overlapped with the red fluorescence inside the cytoplasm of the cells only. These results suggest that the Au-FAM-MSH was not as readily taken up by cells as compared to the FAM-MSH peptide alone. At the same time, the conjugation of FAM-MSH to the gold nanoparticles may protect the peptide from being degraded inside the cell as rapidly. Interestingly, there was no green fluorescence inside the cell nucleus for Au-FAM-MSH incubated cells at 3 hours or 24 hours.

It is possible that both FREG-peptide and MSH-peptide prevented the nuclear entry of the gold nanoparticles. Another explanation is that the FAM-FREG-peptide and FAM-MSH-peptide decoupled from the gold nanoparticles and became retained in the cytoplasm, while the gold nanoparticles entered into the nucleus but were

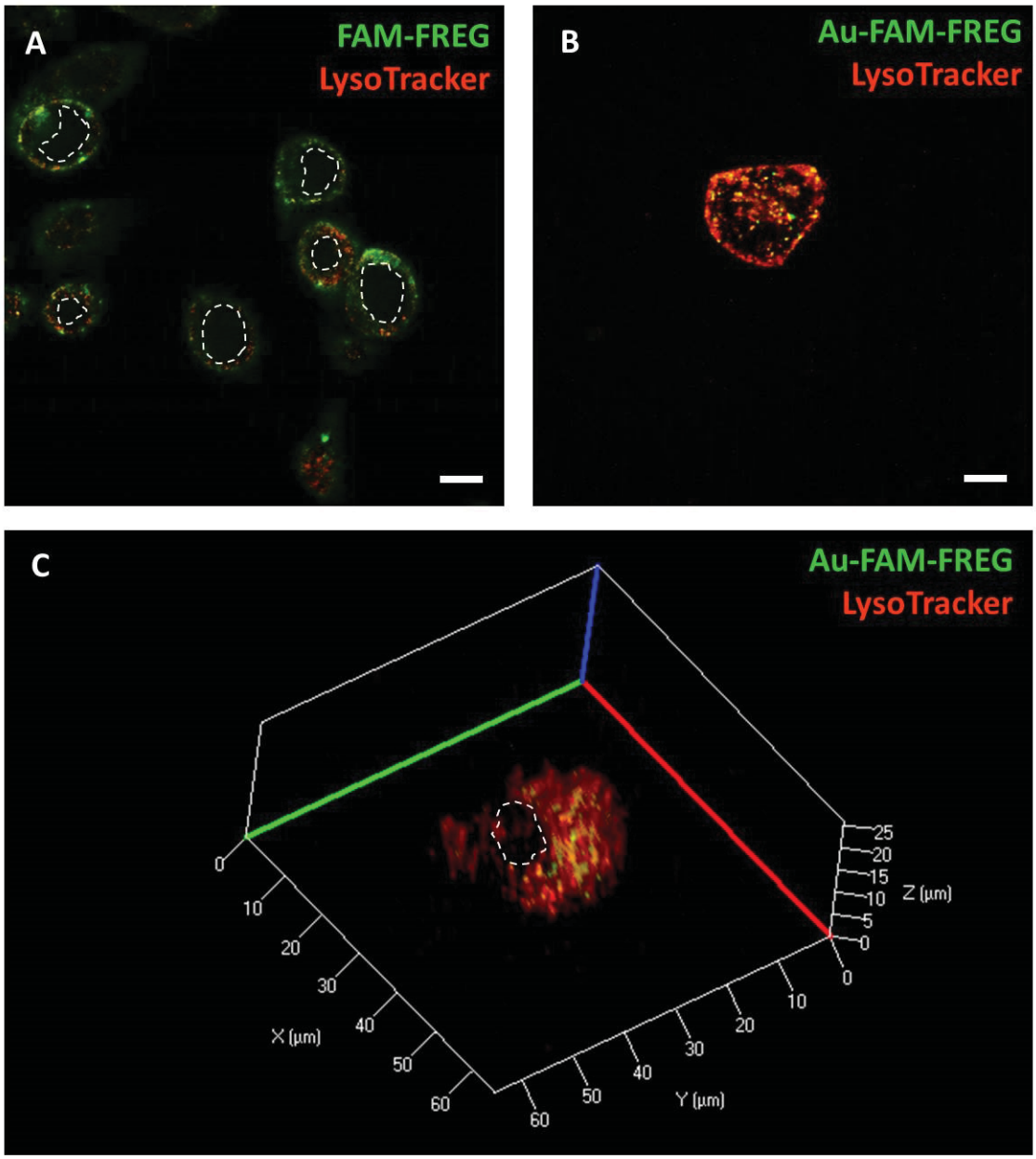

Figure 3–7: Confocal fluorescence microscopy images of B16 melanoma cells treated for 24 h with: (A) FAM-FREG-peptide, and (B) Au-FAM-FREG. (C) A 3D render of a B16 melanoma cell treated with Au-FAM-FREG for 24 h. Red fluorescence signal is from LysoTracker Red. Green fluorescence signal is from fluorescein (FAM). White dotted line indicates the cell nucleus. Scale bar is 10 μm.

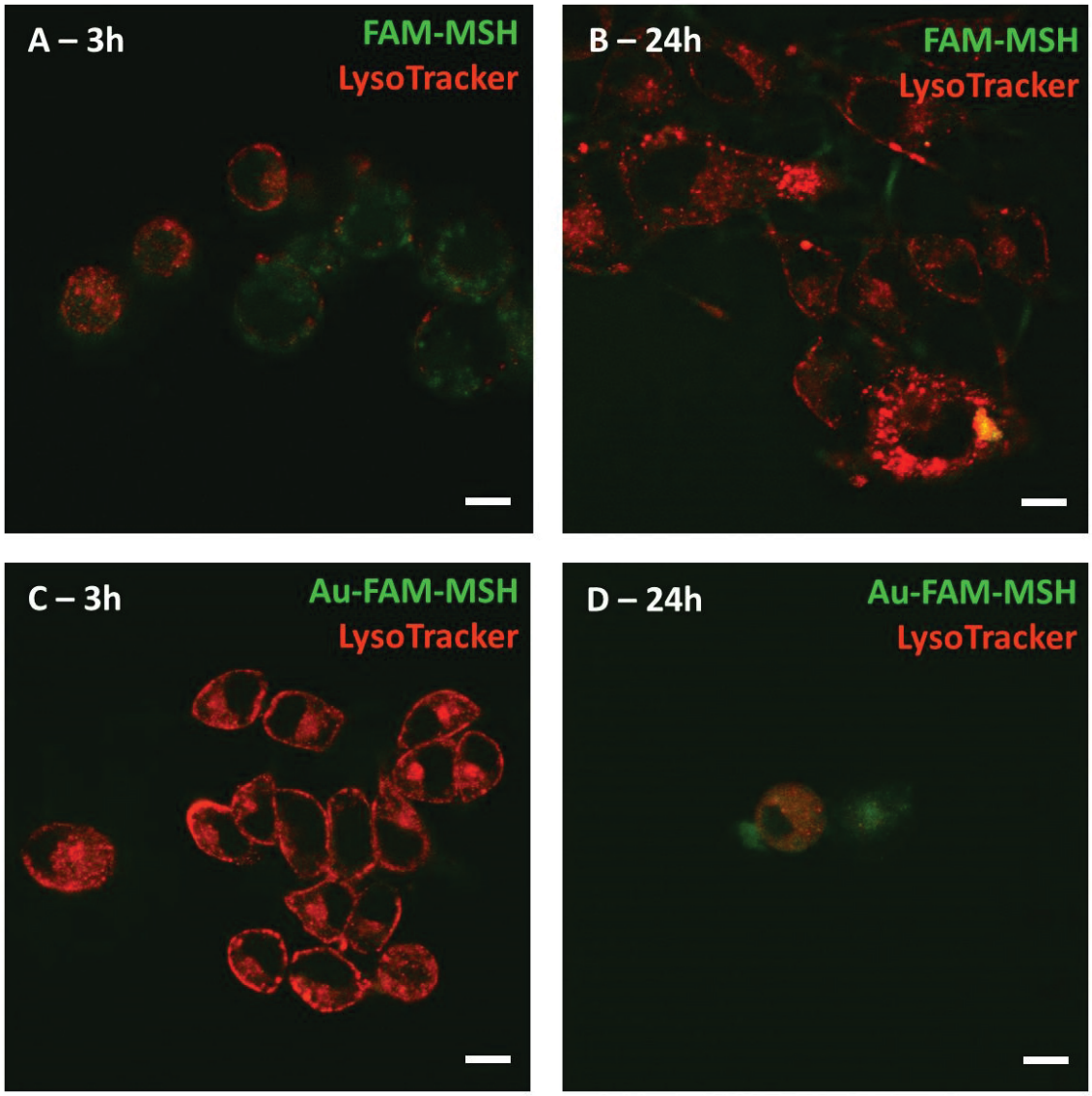

Figure 3–8: Confocal fluorescence microscopy images of B16 melanoma cells treated for (A) 3 hours with FAM-MSH-peptide, (B) 24 hours with FAM-MSH-peptide, (C) 3 hours with Au-FAM-MSH, and (D) 24 hours with Au-FAM-MSH. Red fluorescence signal is from LysoTracker Red. Green fluorescence signal is from fluorescein (FAM). Scale bar is 10 μm.

unable to be visualized using confocal microscopy. At the very least, these results showed that the FAM-peptide and MSH-peptide can altered the cell uptake dynamics of gold nanoparticles into B16 melanoma cells.

3.4 Biodistribution of Gold Nanoparticles Conjugates by ICPMS Analysis

3.4.1 Concentration of gold nanoparticle conjugates per tissue weight

An initial biodistribution study of Au, Au-FREG, and Au-MSH in B16 tumour-bearing C57/BL6 mice was performed at time points of 1 hour and 24 hours post injection of nanoparticles. The results (normalized to the weight of the organ or bodily fluid) are summarized in Figure 3–9.

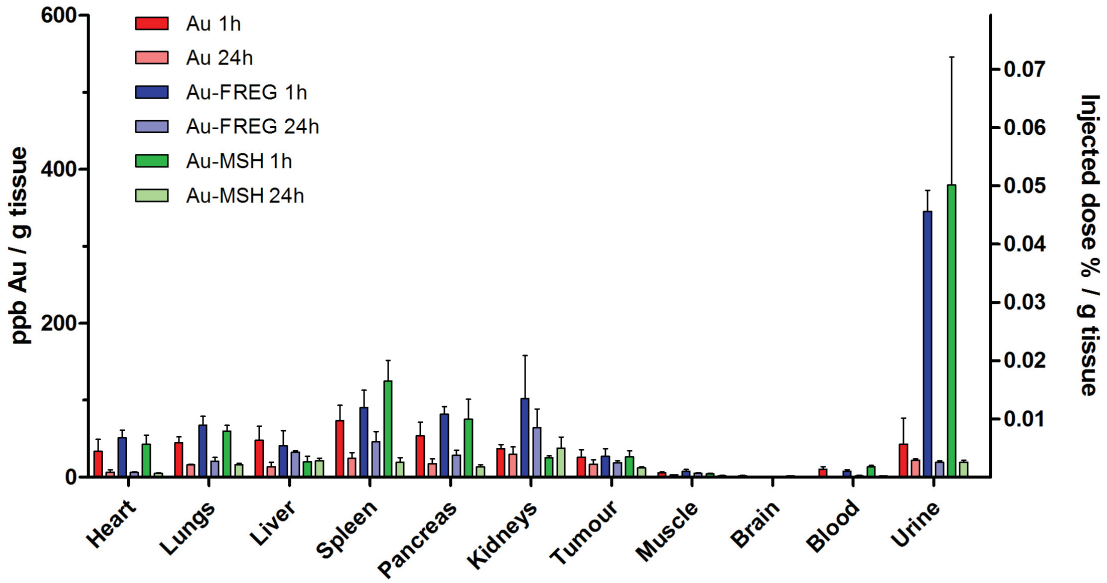

Figure 3–9: Biodistribution of Au, Au-FREG, and Au-MSH nanoparticles in B16 tumour-bearing C57/BL6 mice at 1 h and 24 h post-injection by ICPMS analysis (shown as mean ± SEM with n=3).

During this initial biodistribution study, it was evident that 2 time points were insufficient to determine the distribution dynamics of the gold nanoparticles. Furthermore, the 1 hour time point proved difficult to standardize across all injected mice because there was not enough time to dissect and collect large groups of mouse organs within 1 hour of gold nanoparticle injection. These results also indicated that the gold nanoparticle conjugates were being rapidly cleared from the blood and out of the body. As such, for the second biodistribution study, we decided to PEGylate the gold nanoparticles to improve their bioavailabilty. We also adjusted the first time point to 4 hours and add in a third time point at 72 hours post injection.

A second biodistribution study with Au, Au-PEG, Au-Myx, Au-PEG-Myx, Au-cRGD, and Au-PEG-cRGD was performed by ICPMS analysis in B16 tumour-bearing C57/BL6 mice at 4 h, 24 h, and 72 h. The results (normalized to the weight of the organ or bodily fluid) are summarized in Figure 3–10, Figure 3–11, and Figure 3–12.

In the case of tiopronin-capped gold nanoparticles, the highest concentration of gold is observed in the urine at 4 h and 24 h. At 72 h, the highest concentration of gold is observed in both the liver and the tumour. As expected, there was negligible detection of gold in the heart, lungs, pancreas, muscle, and brain up to 72 hours. The concentration of gold remained relatively constant in the kidneys and tumour up to 72 hours, whereas the concentration increased over the 72 h for the liver and spleen at the expense of the concentration in the blood and urine. This implies that the tiopronin-capped gold nanoparticles experienced a high rate of excretion via urine in

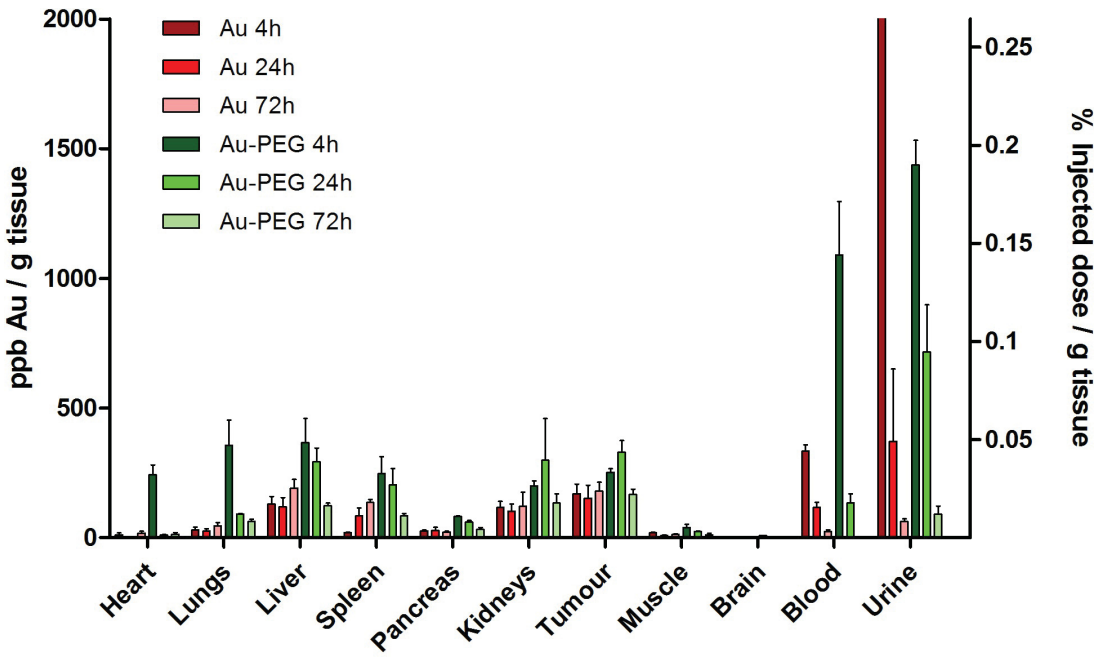

Figure 3–10: Biodistribution of Au vs Au-PEG nanoparticles in B16 tumour-bearing C57/BL6 mice at 4 h, 24 h, and 72 h post-injection by ICPMS analysis (shown as mean ± SEM with n=3). Note that the value for Au in the urine at 4 h is above the maximum of the y-axis at 3480 ± 832 ppb Au /g tissue (or approximately 0.4599 ± 0.1099% injected dose / g tissue).

the first 24 h post administration, and then gradually modulated to a hepatic and RES system clearance up to 72 h post administration.

In the case of Au-Myx nanoparticles, the highest concentration of gold is similarly observed in the urine at 4 h and 24 h. At 72 h, the highest concentration of gold is observed in the kidneys and tumour. In contrast to the tiopronin-capped gold nanoparticles, the concentration of gold remained relatively constant in the liver. In the kidneys, the concentration of gold reached a minimum at 24 h, and seemed to

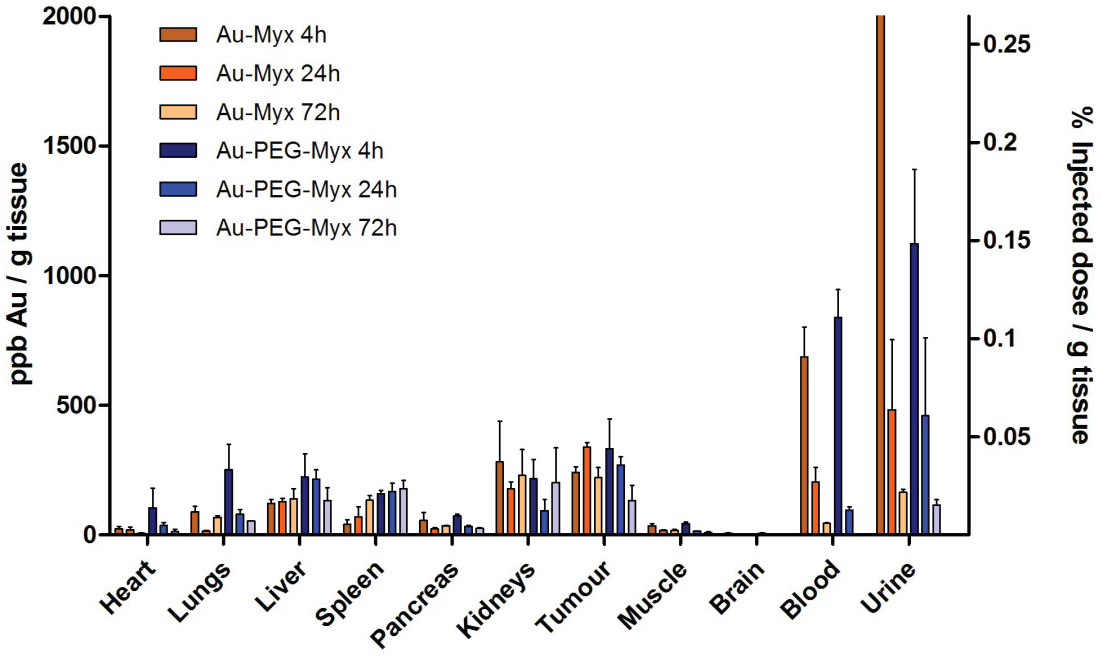

Figure 3–11: Biodistribution of Au-Myx vs Au-PEG-Myx nanoparticles in B16 tumour-bearing C57/BL6 mice at 4 h, 24 h, and 72 h post-injection by ICPMS analysis (shown as mean ± SEM with n=3). Note that the value for Au-Myx in the urine at 4 h is above the maximum of the y-axis at 3787 ± 1853 ppb Au / g tissue (or approximately 0.5004 ± 0.2449% injected dose / g tissue).

increase up to 72 h. In the tumour, the concentration of gold increased for the first 24 h, and then decreased at 72 h. The concentration of gold in the tumour at 24 h for Au-Myx nanoparticles was significantly higher ($p = 0.02$) than the tiopronin-capped gold nanoparticles. These results suggest that the myxoma peptide improved the targeting of the gold nanoparticles towards the tumour, and modulated the elimination of gold nanoparticles to favour a renal over hepatic clearance.

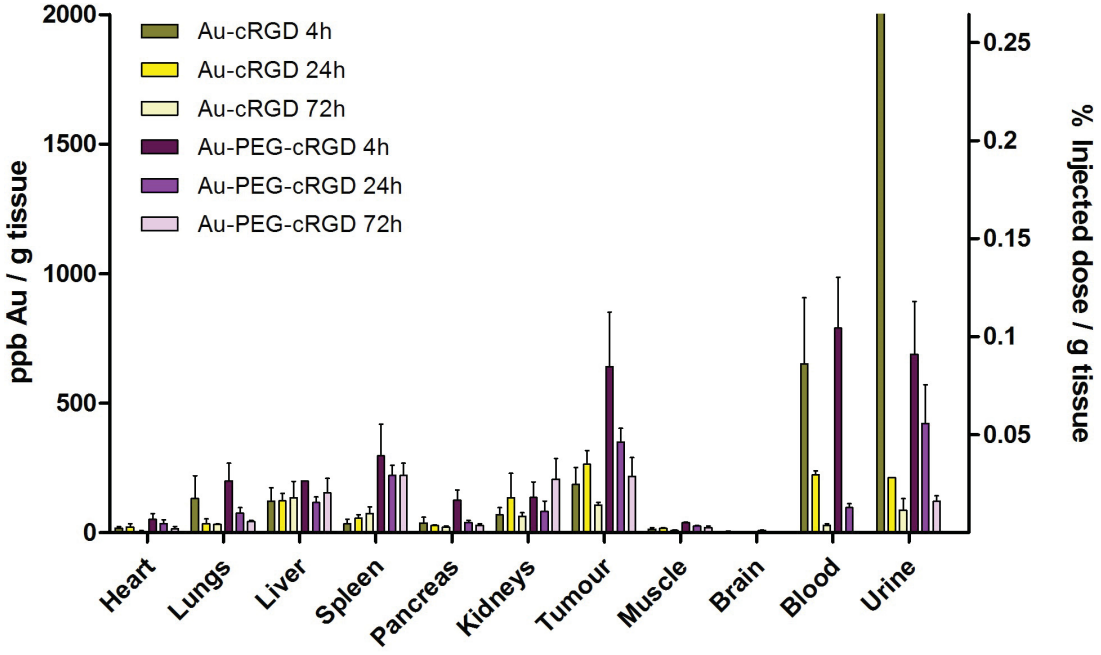

Figure 3–12: Biodistribution of Au-cRGD vs Au-PEG-cRGD nanoparticles in B16 tumour-bearing C57/BL6 mice at 4 h, 24 h, and 72 h post-injection by ICPMS analysis (shown as mean ± SEM with n=3). Note that the value for Au-cRGD in the urine at 4 h is above the maximum of the y-axis at 8022 ± 4167 ppb Au / g tissue (or approximately 1.060 ± 0.551% injected dose / g tissue).

For Au-cRGD nanoparticles, the highest concentration of gold is also similarly observed in the urine at 4 h However, at 24 h, the highest concentration is observed in the tumour; and at 72 h, it was the liver. At 24 h, the concentration of Au-cRGD in the tumour seemed to be higher than that of tiopronin-capped gold nanoparticles (but not statistically significant, $p = 0.20$). At 72 h, the concentration of Au-cRGD fell significantly compared to 24 h ($p = 0.04$). The cRGD peptide seemed to reduce the RES-uptake of gold nanoparticles as the concentration in the spleen was lower

at 72 h after injection. However, in general, the Au-cRGD seemed to be eliminated from the body quite quickly as the concentration of gold in the urine at 4 h was more than twice that of tiopronin-capped gold nanoparticles and Au-Myx.

Overall, PEGylation of gold nanoparticles significantly reduced the renal clearance as the gold concentration in the urine was approximately $\frac{1}{3}$ of non-PEGylated gold nanoparticles at 4 h. Correspondingly, the gold concentration in the blood and other organs were almost twice as much as their counterparts injected with non-PEGylated gold nanoparticles. However, the increased blood circulation time granted by PEGylation seemed to be short. At 24 hours after injection, the gold concentration in the blood and other organs returned to levels comparable to non-PEGylated gold nanoparticles. The PEG ligands also seemed to dominate the clearance modulation effects of the peptides on the gold nanoparticles as all PEGylated gold nanoparticles with or without peptides seemed to have a preferential renal clearance as seen through decreasing gold concentration in the liver, and static concentration in the spleen over the 72 h period post injection. Interestingly, PEGylation of Au-cRGD seemed to improve its retention in the tumour over the 72 h period as its gold concentration in the tumour was always higher or approximately equal to its non-PEGylated counterpart. However, there were no significant differences between the concentration of gold in the tumour from Au-cRGD and Au-PEG-cRGD for the same time points (for 4 h, $p = 0.10$; for 24 h, $p = 0.32$; for 72 h, $p = 0.21$). For Au-PEG and Au-PEG-Myx nanoparticles, PEGylation seemed to improve the gold concentration in the short term up to 4 h, but at 24 h and 72 h, the retention in the tumour was lower than that of their non-PEGylated counterparts. Nevertheless,

there were no significant differences between the concentration of gold in the tumour from Au-Myx and Au-PEG-Myx for the same time points.

Table 3–2: Summary of p-values for tumour Au concentrations among PEGylated gold nanoparticles

	Au-PEG		
	4 h	**24 h**	**72 h**
Au-PEG-Myx	0.53	0.33	0.61
Au-PEG-cRGD	0.14	0.79	0.54

Table 3–3: Summary of p-values for tumour Au concentrations among non-PEGylated gold nanoparticles

	Au		
	4 h	**24 h**	**72 h**
Au-Myx	0.17	0.02	0.47
Au-cRGD	0.84	0.20	0.12

Comparing the effect of the peptide tumour targeting among non-PEGylated and PEGylated gold nanoparticles, there was no significant difference between the gold concentrations at the same time points for PEGylated gold nanoparticles as summarized in Table 3–2, nor was there a significant difference for the non-PEGylated gold nanoparticles as summarized in Table 3–3, with the exception of Au vs Au-Myx at 24 h as stated previously. Comparing the effect of PEGylation as summarized in Table 3–4, there was also no statistically significant difference in the tumour gold concentrations between PEGylated and non-PEGylated gold nanoparticles for the same time points. However, the p-values in these cases tended more towards significance (defined at $p < 0.05$) than comparing the effect of peptides. This suggests that

Table 3–4: Summary of p-values for tumour Au concentrations among PEGylated and non-PEGylated gold nanoparticles

		Au	**Au-Myx**	**Au-cRGD**
Au-PEG	**4 h**	0.10		
	24 h	0.06		
	72 h	0.77		
Au-PEG-Myx	**4 h**		0.48	
	24 h		0.12	
	72 h		0.27	
Au-PEG-cRGD	**4 h**			0.11
	24 h			0.32
	72 h			0.21

PEGylation had a greater effect of improving nanoparticle delivery to the tumour than the addition of targeting moieties. However, the addition of targeting peptides did not negatively impact the enhanced delivery by PEGylation either.

3.4.2 Non-specific targeting properties of peptides

To investigate the non-specific targeting properties of the peptides, we normalized the gold concentration of the spleen, liver, and kidneys to that of the tumour in each mouse. We define the ratio to be:

$$\text{Ratio} = \frac{[\text{Au}]_{organ}}{[\text{Au}]_{tumour}} \tag{3.1}$$

The ratios of the spleen, liver, and kidneys will be referred to as splenic, hepatic, and renal indices respectively. These results are summarized in 3–13.

A ratio of less than 1 is preferable because this indicates that the gold concentration in the tumour is higher than that of the organ of interest. The general trend

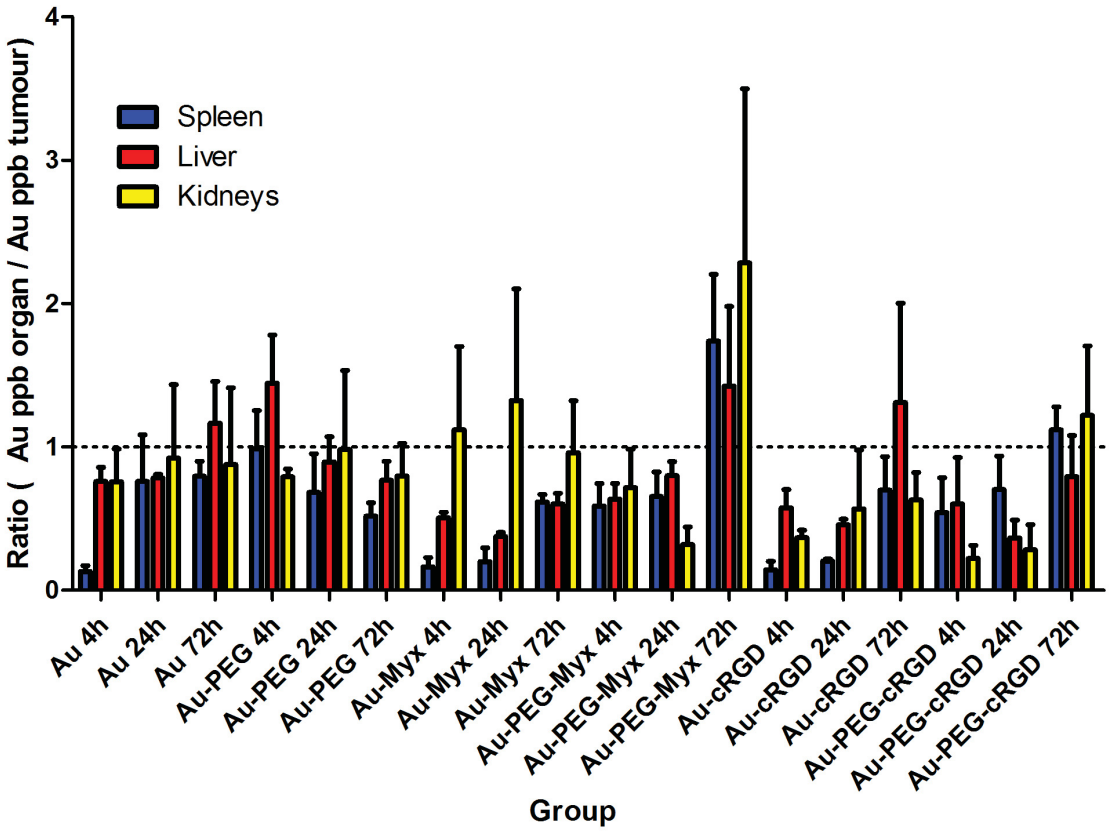

Figure 3–13: Concentration of Au in ppb in major organs of accumulation normalized to tumour (shown as mean ± SEM with n=3)

was that all indices start low at 4 h and increase at 24 h and 72 h. Au-PEG nanoparticles were the exception to this trend as their indices were above or around 1 at 4 h, which then decreased at 24 h and 72 h. Au-Myx had improved splenic and hepatic indices compared with tiopronin-capped gold nanoparticles, but a worsened renal index which increased above 1 at 4 h and 24 h. Au-cRGD had improved splenic and renal indices, but the hepatic index still increased to above 1 at 72 h. Au-PEG-Myx

and Au-PEG-cRGD also had improved indices up to 24 h, but not as much as their non-PEGylated counterparts. At 72 h, both Au-PEG-Myx and Au-PEG-cRGD had all indices above 1. For Au-PEG-Myx at 72 h, the renal index increased substantially to be above 2. Overall, the peptides improved the targeting of the gold nanoparticles for up to 24 h to the tumour while decreasing non-specific targeting accumulation in the spleen, liver, and kidneys. PEGylation appeared to slightly attenuate the specificity of the peptides for the first 24 h and then non-specificity dominated at 72 h.

3.4.3 Retention of gold by mass and total injected dose

Figure 3–14 shows the average total mass of gold per mouse broken down per solid organ for each gold nanoparticle formulation. Blood and muscle were not included into this analysis because their entirety was not completely harvested from each animal. Also, blood volume and muscle mass are quite variable among mice due to differences in age and gender. Urine was also not included in this analysis because not all the urine excreted by the mice were collected during the time points as we did not have access to metabolic cages. The range of mass accumulation of gold ranged from 2 - 8 % of the total administered dose depending on the conjugate and time after injection, of which 0.75 - 2 % of the total administered dose was found in the tumour (solid black bars). The liver was the organ where most of the gold by mass were found, ranging from 1.25 - 4.5 % of the total administered dose. A full tabularized breakdown of Au (in dose percent mass) per solid organ and time point for the nanoparticle conjugates can be found in Table 5–1 in the Appendix.

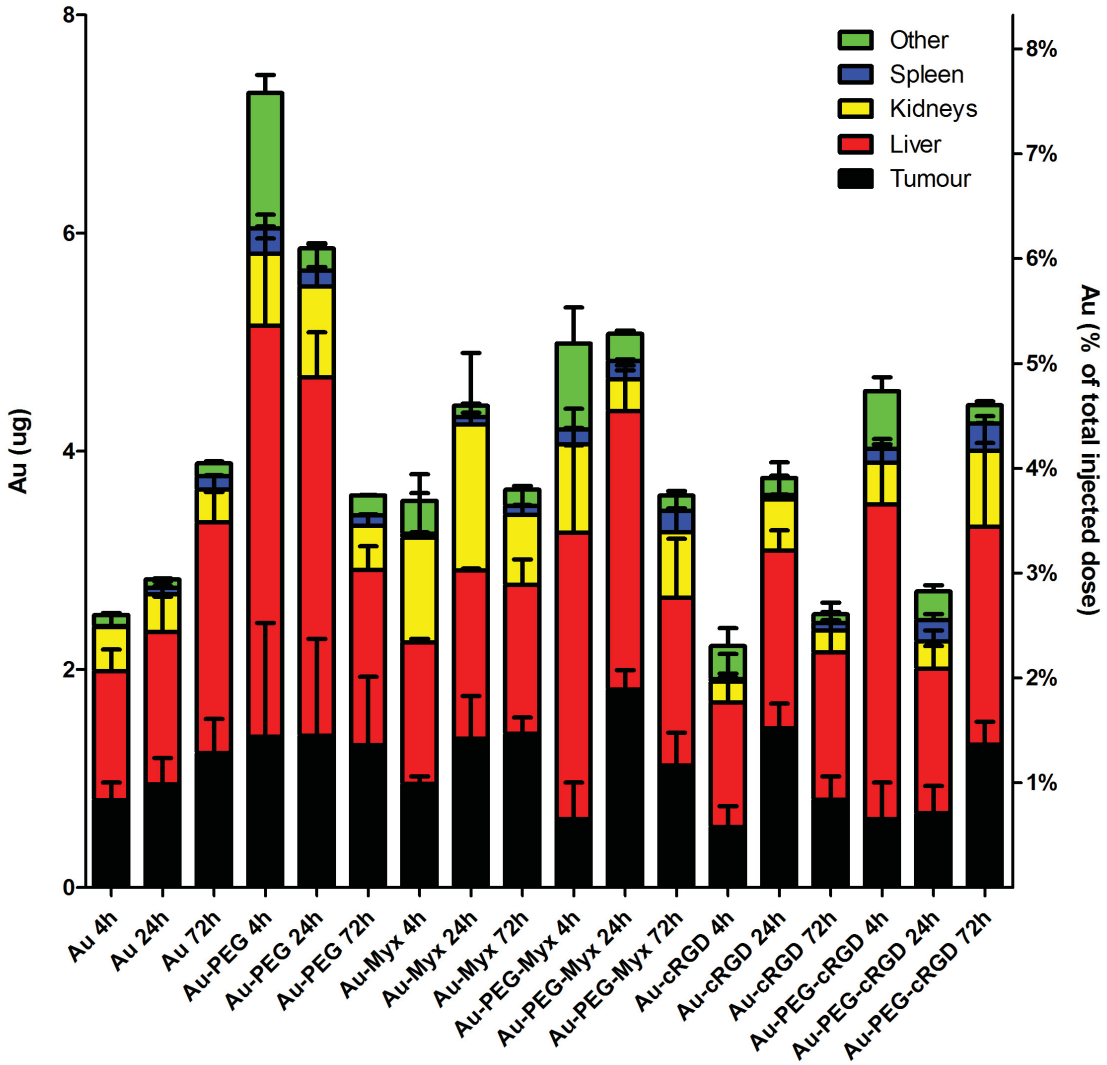

Figure 3–14: Breakdown of Au (in mass and percent of total injected dose) per solid organ and time point for Au, Au-PEG, Au-Myx, Au-PEG-Myx, Au-cRGD, and Au-PEG-cRGD conjugates (shown as mean ± SEM with n=3). Other category includes heart, lungs, pancreas, and brain only. Blood, urine, and muscle are not included in this analysis.

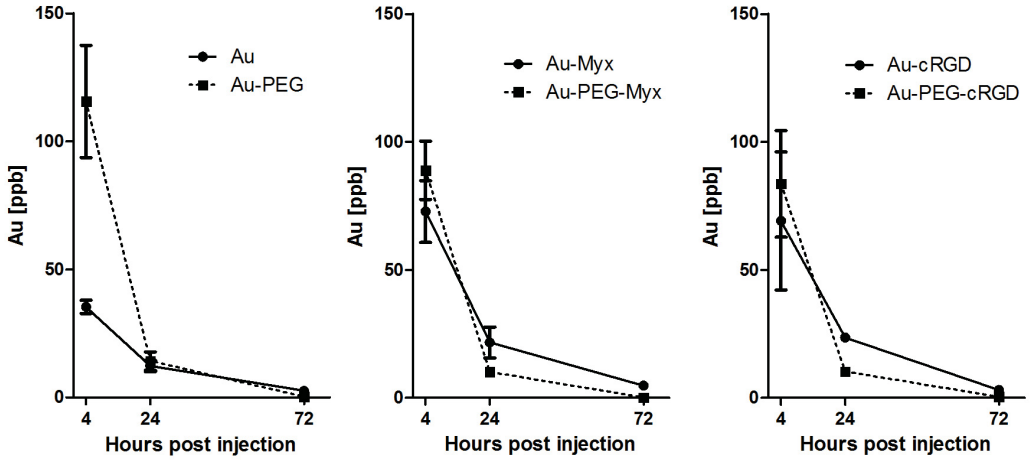

Figure 3–15: Plasma Au concentration-time curve for Au vs Au-PEG (left), Au-Myx vs Au-PEG-Myx (centre), and Au-cRGD vs Au-PEG-cRGD (right) shown as mean ± SEM with n=3.

Table 3–5: Area Under the Curve Measurements of Au-Conjugates

Au-Conjugate	**Area under the Curve (μg·h/L)**	**Clearance (L/h)**
Au@Tiopronin	835	9.97×10^{-2}
Au-PEG-COOH	1646	5.06×10^{-2}
Au-Myx	1578	5.28×10^{-2}
Au-PEG-Myx	1235	6.74×10^{-2}
Au-cRGD	1566	5.32×10^{-2}
Au-PEG-cRGD	1195	6.97×10^{-2}

3.4.4 Area under the curve and clearance analysis

The plasma Au concentration is plotted against time for Au vs Au-PEG, Au-Myx vs Au-PEG-Myx, and Au-cRGD vs Au-PEG-cRGD as shown in Figure 3–15.

The area under the curve (AUC) gives a measure of the actual gold nanoparticle-conjugate exposure of the gold nanoparticle conjugates and is tabulated in Table 3–5. The AUC values are calculated from using the "trapezoidal rule" with the mean value of each data point [224]. Clearance refers to the volume of plasma cleared of Au per unit time and is related to AUC for intravenous injection dosing by the following formula [224]:

$$\text{Clearance} = \frac{\text{Dose}}{\text{Area under curve}} \tag{3.2}$$

The dose (in μg) of Au injected into each mouse is calculated by the following equation:

$$\begin{aligned} \text{Dose} &= \text{Concentration} \times \text{Volume} \times \text{Mass of Au per nanoparticle} \\ &= 10\ \mu\text{M} \times 250\ \mu\text{L} \times 33.296\ \text{kg/mol} \\ &= 83.24\ \mu\text{g} \end{aligned} \tag{3.3}$$

Au-PEG showed the highest AUC at 1646 μg·h/L and slowest clearance at 5.06×10^{-2} L/h , whereas tiopronin-capped gold nanoparticles had the smallest AUC at 835 μg·h/L and fastest clearance at 9.97×10^{-2} L/h. Au-Myx and Au-cRGD had comparably high AUC values at around 1570 μg·h/L. Interestingly, PEGylation of Au-peptides decreased the AUC, which implies that PEGylation increased the clearance of the gold from the plasma. However, this decrease in AUC may be explained by the targeting effect of the peptides drawing the gold nanoparticles out of the plasma and into the tumour at 24 h. As such, we can conclude that PEGylation alone and

peptide conjugation alone significantly decreased the clearance of tiopronin-capped gold nanoparticles so they are retained in the plasma volume. PEGylation and peptide conjugation combined together decreased the first pass clearance of gold nanoparticles, giving the peptide more time in the plasma to target and become retained in the tumour.

CHAPTER 4
Determination of Nanoparticle Biodistribution by Imaging and Microscopy: Results and Discussion

Optical and optoacoustic methods of determining nanoparticle biodistribution are being sought for real-time *in vivo* quantitative analysis. In the context of this project, there is also need to correlate across different length scales of how gold nanoparticles behave *in vivo* as merely accumulating into the tumour but not localizing inside the tumour cells is not sufficient for effective nanoparticle-based therapies. The fluorescent and electron-opaque properties of gold nanoparticles make it amendable to be detected using fluorescence imaging and electron microscopy. Gold nanoparticles are also good contrast agents in photoacoustic imaging, where pulsed laser illumination is used to induce optical absorption and heating of the light-absorbing gold nanoparticles. The gold nanoparticle undergoes thermo-elastic expansion and generates acoustically-detectable pressure waves. The acoustic signal is detected and used to generate an image. The advantage is inherently co-registered high spatial resolution with high sensitivity in real time. The photoacoustic effect converts photons into ultrasonic waves, which allows photoacoustic imaging to have greater imaging depths as acoustic scattering in tissue is approximately three orders of magnitude less than optical scattering [225]. Furthermore, photoacoustic imaging allows the excitation of different molecules at different optical wavelengths as a means to differentiate between materials of different chemical compositions [225]. Mallidi

et al. showed that photoacoustic imaging was able to discern between anti-EGFR gold nanoparticles, non-conjugated gold nanoparticles, and an NIR dye in mouse tissue *ex vivo* [226]. Depending on the implementation of the optical excitation and ultrasonic detection setup, photoacoustic imaging has the unique advantage of being able to conduct multiscale biological structural imaging at high resolution including organelles, cells, tissues, and organs [225]. This is because photoacoustic imaging can scale spatial resolution and imaging depth across both optical and ultrasonic dimensions [225]. These features of photoacoustic imaging make it an attractive modality to develop for determining the quantitative biodistribution of nanoparticles in real-time and at multiple length scales. Cook *et al.* have reported the use of photoacoustic imaging for quantitative assessment of gold nanoparticle biodistribution in cells and xenograft tumour tissue sections [227].

4.1 Fluorescence Imaging of Gold Nanoparticles in Excised Mouse Organs

To determine the optimal dosing for signal in the in vivo fluorescence microscope, different concentrations of gold nanoparticles were injected into a raw chicken thigh as an imaging phantom as shown in Figure 4–1.

At high concentration, the gold nanoparticles had decreased fluorescence signal due to the increased opacity of the injected solution attenuating the emission and excitation light. Next, optimization of the imaging system filter sets was performed by measuring the fluorescence photon counts of an Eppendorf tube of 17.5 μM Au nanoparticles using the ROI tool over different combinations of excitation and emission filters. As a starting point, filters with wavelength cutoffs closest to the optimized values obtained from the excitation vs. emission heat map measured on

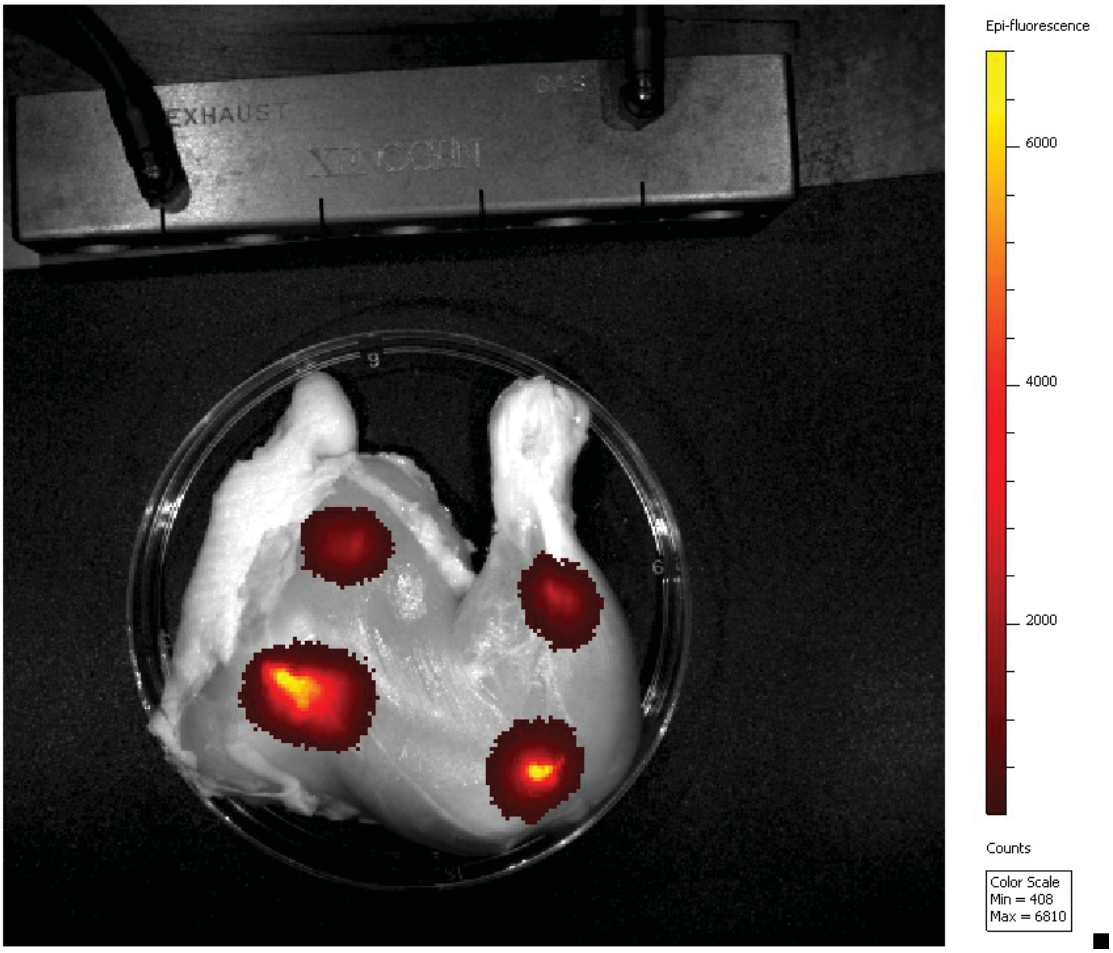

Figure 4–1: Optimization of gold nanoparticle fluorescence in IVIS Spectrum using a raw chicken thigh as an imaging phantom.

a plate reader (as shown in Figure 4–2) were used (480 nm excitation and 735 nm emission). Interestingly, as summarized in Table 4–1, the optimized set of emission and excitation filters for the IVIS Spectrum in vivo fluorescence imaging system was found to be 675 nm excitation and 780 nm emission, which were very different from

the values obtained from the plate reader. Background corrected fluorescence intensity of the optimized excitation and emission sets from the plate reader and IVIS Spectrum imaging system were 9400 and 87.03 respectively, a difference of roughly 1800-fold. These discrepancies may be related to variations in optical setup between the two apparatuses. The plate reader uses monochromatic light with a wavelength bandwidth of 4.0 nm and is optimized for fluorescence measurements of reagents in a multi-well plate (capable of a field of view of approximately 2 mm^2). On the other hand, the IVIS Spectrum imaging apparatus uses a scanning laser assembly optimized for a larger range of area measurements (field of view can range from 15 - 506.25 cm^2). The IVIS Spectrum imaging apparatus also has greater excitation and emission filter bandwidths of 30 nm and 20 nm respectively. In addition, the quantum efficiencies of the two imaging systems are different, with the IVIS Spectrum imaging apparatus specifications reporting as much as a 50% difference in efficiency between the 500 - 700 nm and 700 - 900 nm ranges. The

Table 4–1: Fluorescence Intensities of Different Emission and Excitation Filters on the IVIS Spectrum

		Emission (nm)			
		740	**760**	**780**	**800**
Excitation (nm)	**465**	4.41×10^6	5.33×10^6	5.88×10^6	5.33×10^6
	500			7.79×10^6	
	535			9.96×10^6	
	570			1.27×10^7	
	605			1.56×10^7	
	640			1.67×10^7	
	675			1.78×10^7	
	710			1.16×10^7	

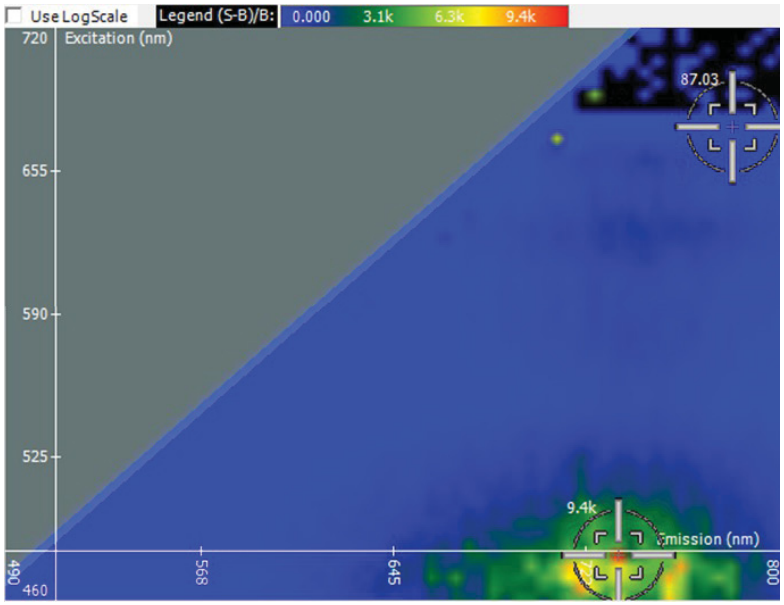

Figure 4–2: Heat map of gold nanoparticle fluorescence with varying excitation and emission wavelengths on the i3 SpectraMax plate reader. The maximum fluorescence signal was achieved at 480 nm excitation and 735 nm emission (indicated by crosshairs in bottom right corner). As a comparison, optimal excitation and emission set values from the IVIS Spectrum imaging system (indicated by crosshairs in top right corner) was roughly 1080 times weaker.

250 μL of Au nanoparticles at a concentration of 17.5 μM was injected intravenously via tail vein into a Lewis lung carcinoma tumour-bearing C57/BL6 mouse. The Lewis lung carcinoma model was used instead of a B16 melanoma tumour model because the Lewis lung carcinomas do not produce melanin to interfere with optical measurements. After 24 hours, the mouse were sacrificed and their organs (liver, tumour, kidneys, and spleen) were harvested for imaging with the IVIS Spectrum imaging system. Organ autofluorescence signal was subtracted from the injected organs by simultaneously imaging the injected organs with organs from a control

mouse with no administration of nanoparticles. Figure 4–3 shows the relative fluorescence signal intensities from all imaged organs. The injected liver gave the highest signal, which masked the signal coming from other organs. Autofluorescence from the kidney was very strong as both the injected and control kidneys showed similarly strong signals. The individual organs were imaged from different angles to avoid fluorescence signal masking by the liver and to localize the nanoparticle distribution within the organ. Organs were imaged using the optimized filter sets as determined previously with an exposure time of 0.25 - 3 seconds. Figure 4–4 showed that the Au fluorescence signal was strong throughout the entire liver, weak throughout the entire spleen, and concentrated mostly in the center of the tumour respectively. The autofluorescence signal from the kidneys made it difficult to localize the Au nanoparticles. The kidneys were sliced open coronally, then imaged with a 520 nm excitation and 780 nm emission filter set at longer exposure times for better signal acquisition. Figure 4–5 shows that the Au nanoparticle fluorescence signal of the kidneys was mostly concentrated in the renal cortex.

4.2 Photoacoustic Imaging of Gold Nanoparticles in Excised Mouse Organs

Photoacoustic imaging of tiopronin-capped gold nanoparticles was performed in excised organs from Lewis lung carcinoma tumour-bearing C57/BL6 mice using the VevoLAZR photoacoustic imaging system. Photoacoustic intensity versus optical wavelength in regions of interested was graphed for the kidneys, liver, and spleen as shown in Figure 4–6.

The kidneys seemed to have different spectral curve types. The light blue and red curves showed a similar trough shape with a minimum at around 750 nm, whereas

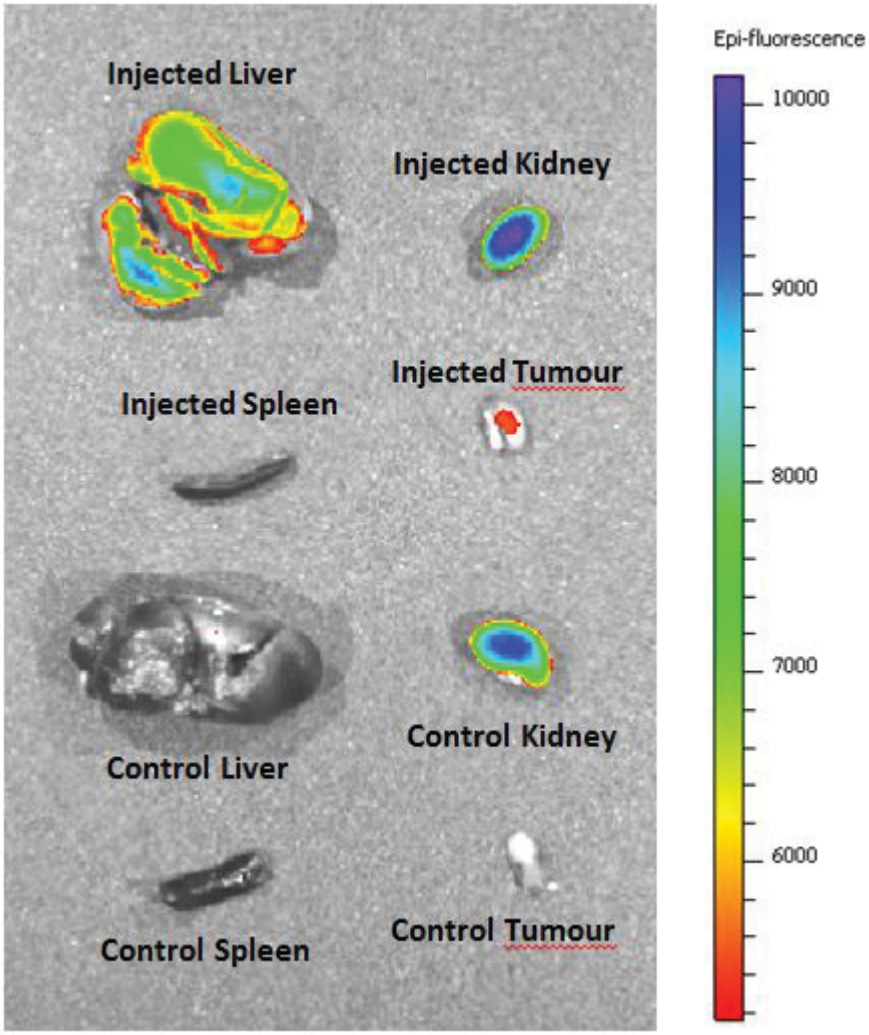

Figure 4–3: IVIS Spectrum fluorescence micrograph showing the relative fluorescence intensity of Au nanoparticles between all injected and control mouse organs

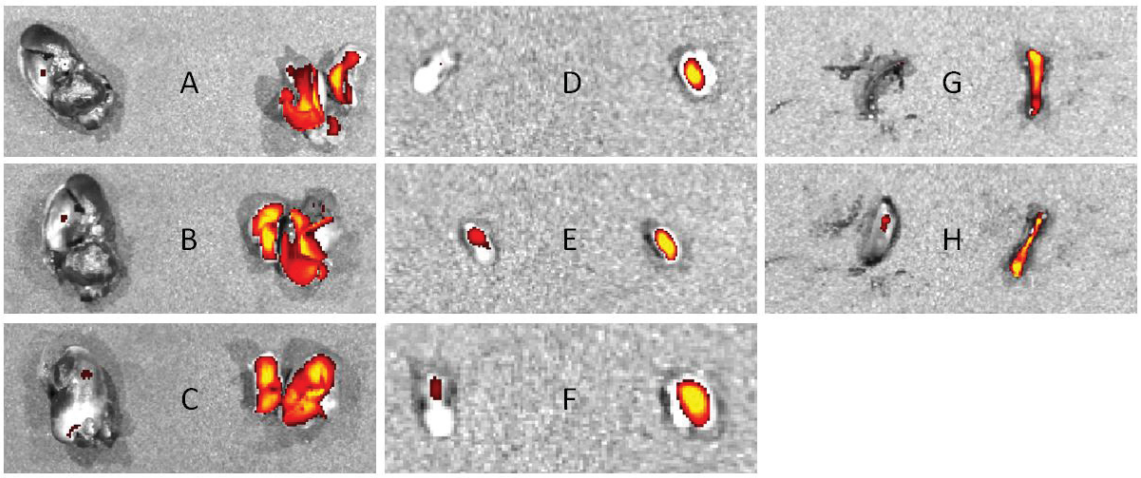

Figure 4–4: IVIS Spectrum fluorescence micrographs showing the fluorescence intensity of Au nanoparticles between control (left side of each panel) and injected (right side of each panel) organs from different orientations. (A) apical view of liver, (B) side view of liver, (C) basal view of liver, (D) apical view of tumour, (E) side view of tumour, (F) basal view of tumour, (G) apical view of spleen, and (H) basal view of spleen.

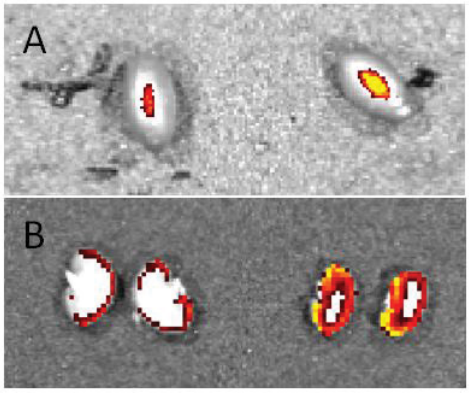

Figure 4–5: IVIS Spectrum fluorescence micrographs showing the fluorescence intensity of Au nanoparticles between control (left side of each panel) and injected (right side of each panel) kidneys from (A) apical side, and (B) sliced coronally.

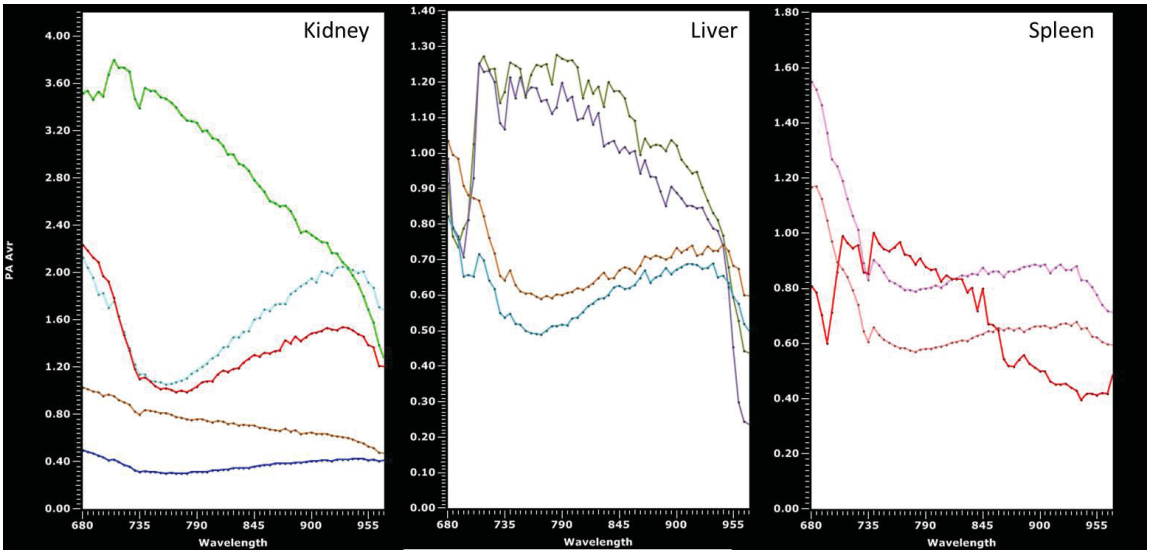

Figure 4–6: Photoacoustic curves of kidneys, liver, and spleen of Lewis lung carcinoma tumour-bearing C57/BL6 mice

the green curves shows higher absorption at lower wavelengths. The liver and spleen also show similar curve shapes to what was observed in the kidneys. From these results, two distinct curve shapes were identified from the subsets of regions of interest in all organs, as shown in Figure 4–7. Spectral unmixing was performed on all organ samples using these two distinct curves, and the signals were multiplexed and displayed as red being component 1 and yellow being component 2.

Component 2 was the photoacoustic signal from the gold nanoparticles because it was not seen in control non-injected organs or imaging phantom. The source of component 1 was unknown, but seemed to be endogenous to all of the excised organs. The spectrally unmixed photoacoustic images of control and injected organs are shown in Figure 4–8, and Figure 4–9 respectively. In the control kidneys, there was negligible photoacoustic signal. In the control liver, spleen, and tumour, there was

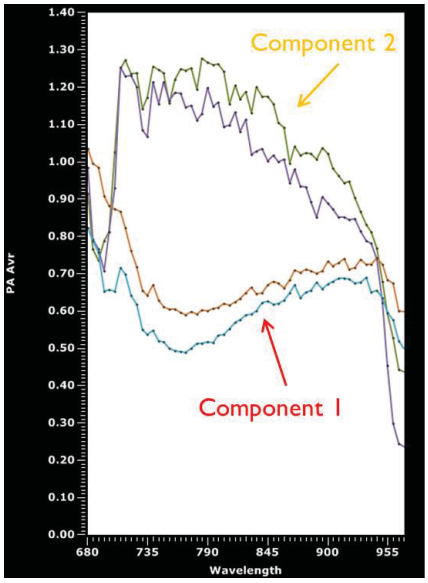

Figure 4–7: Identification of two distinct photoacoustic curves, labelled as red for component 1 and yellow for component 2

only component 1 signal. In the injected kidneys, component 2 signal was seen on the surface. In the injected liver, there was sporadic component 2 signal throughout the entire organ. In the injected spleen, there was strong component 2 signal throughout the organ interior, and also some component 1 signal near the edges/apices of the spleen. In the tumour, the component 2 signal was mostly concentrated only in the apical half of the tumour.

4.3 Environmental Scanning Electron Microscopy of Gold Nanoparticles in Excised Mouse Tumours

Environmental scanning electron microscopy (ESEM) was performed on glutaraldehyde-fixed tumour samples excised from B16 tumour-bearing C57/BL6 mice 24h after intravenous injection with Au-Dox nanoparticles via the tail vein. ESEM allows for biological samples to be imaged in non-vacuum conditions and therefore does not

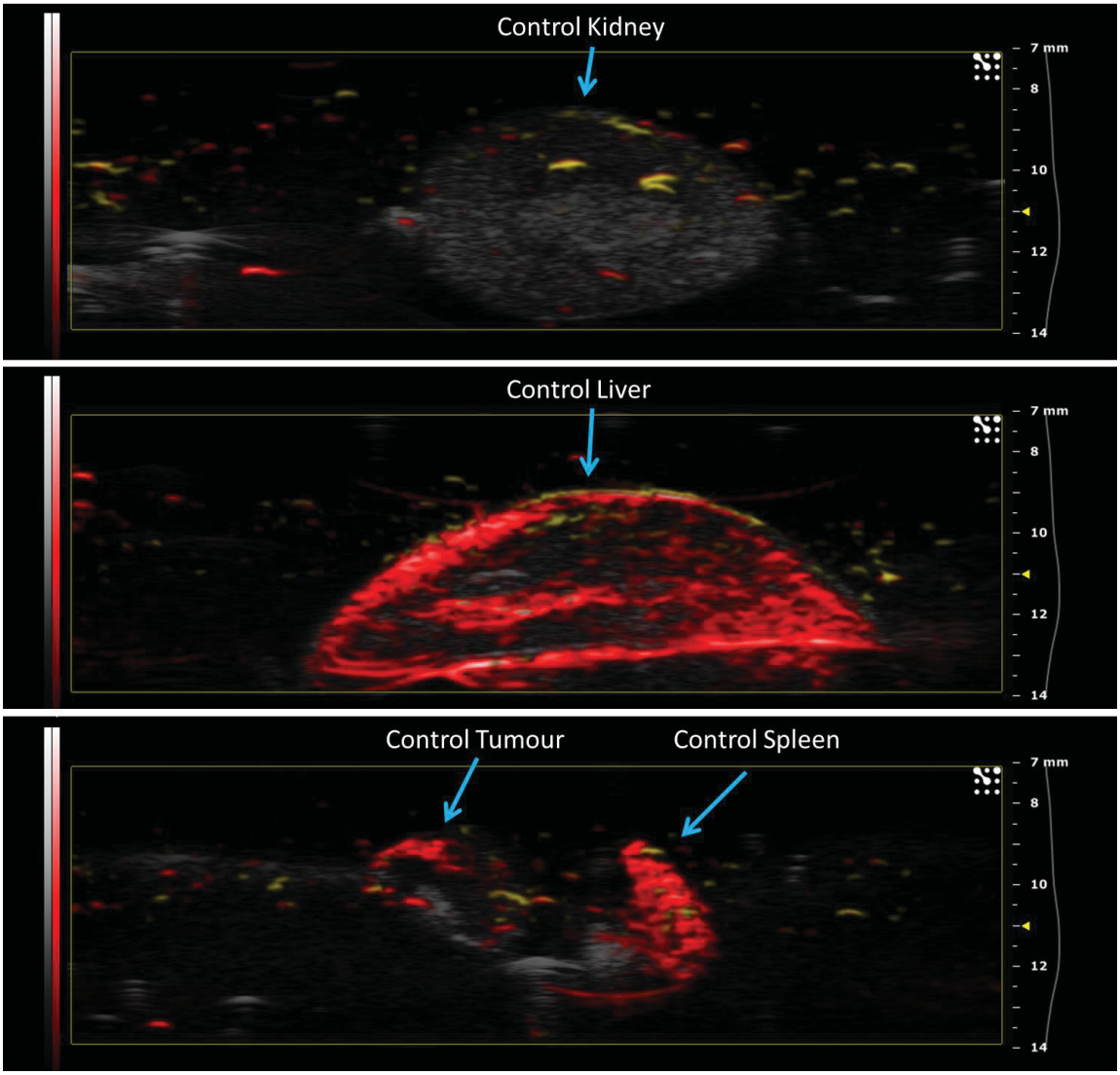

Figure 4–8: Spectrally unmixed photoacoustic images of control kidney (top panel); control liver (centre panel); and control tumour with control spleen (bottom panel). Red color indicates component 1 signal and yellow color indicates component 2 signal.

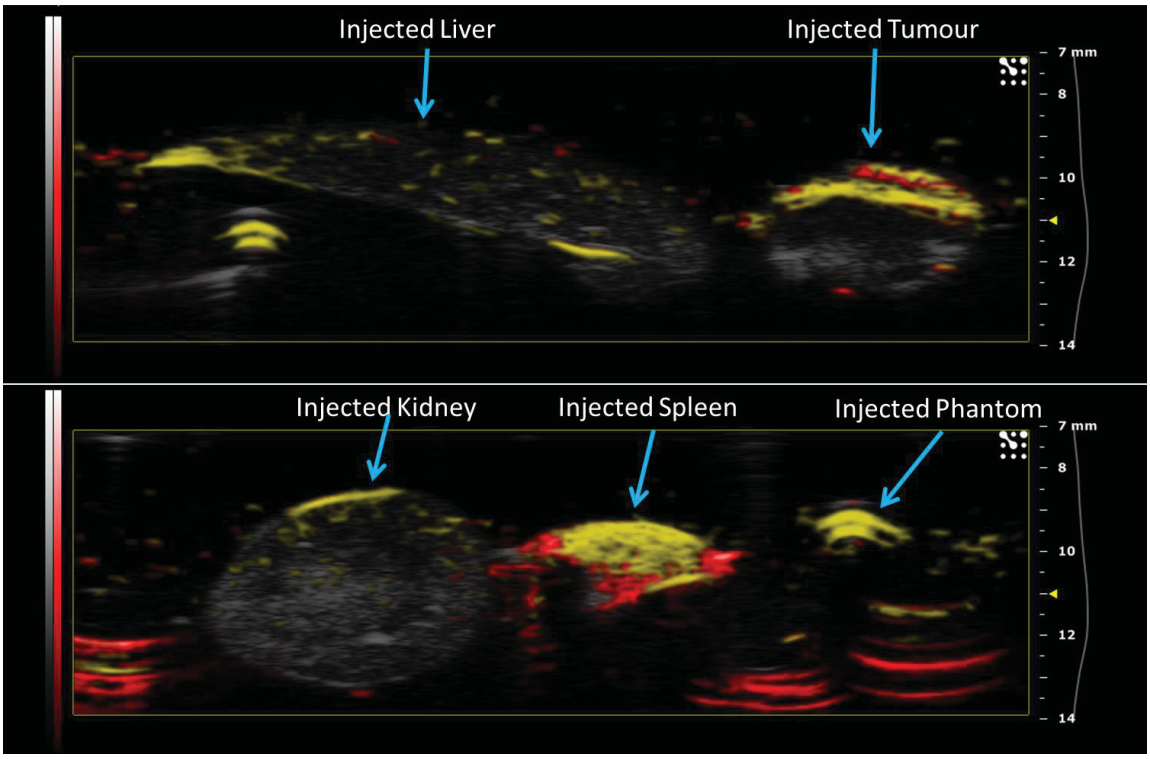

Figure 4–9: Spectrally unmixed photoacoustic images of injected liver and tumour (top panel); and injected kidney, spleen, and tissue phantom (bottom panel). Red color indicates component 1 signal and yellow color indicates component 2 signal.

require extensive or damaging sample preparation techniques. Figure 4–10 shows a typical low magnification ESEM image obtained from the tumour samples, where the clumps of gold nanoparticles had higher contrast signal (brighter white color) due to their high atomic weight number as compared to the mainly carbon biological background. Figure 4–10 suggests that *in vivo* injected Au-Dox nanoparticles were successful in penetrating into the tumour. Au-Dox nanoparticles seemed to also enter cells only at selected locations on the cell membrane or became sequestered in

cells over time as gold nanoparticles could only be seen as large clusters instead of dotted throughout the tumour cell membrane.

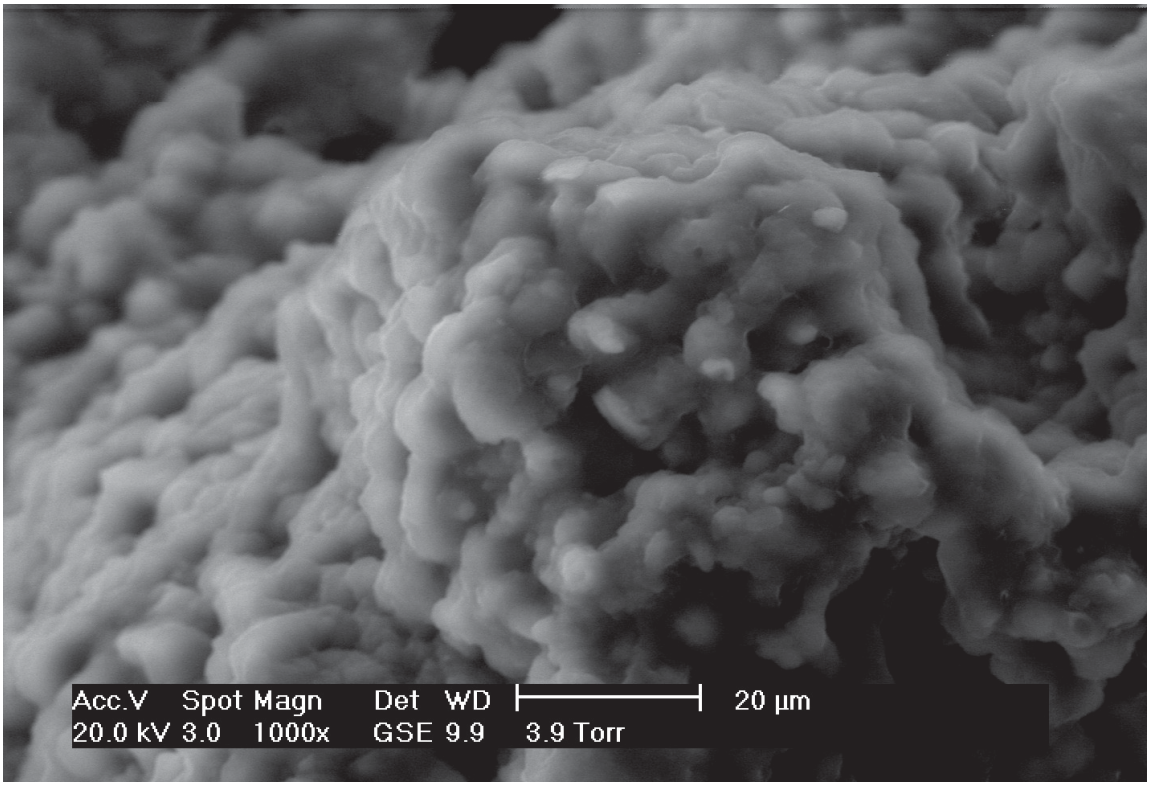

Figure 4–10: ESEM image of Au-Dox nanoparticles inside B16 tumours excised from a C57/BL6 mouse

To ascertain whether the gold nanoparticles aggregated inside the tumour, gold nanoparticle clusters were imaged by ESEM at higher magnification. A typical example is shown in Figure 4–11. Individual dots of gold nanoparticles could be discerned within the larger gold cluster and this suggests that the gold nanoparticles were not aggregating but are simply collected together by the cell via an unknown mechanism.

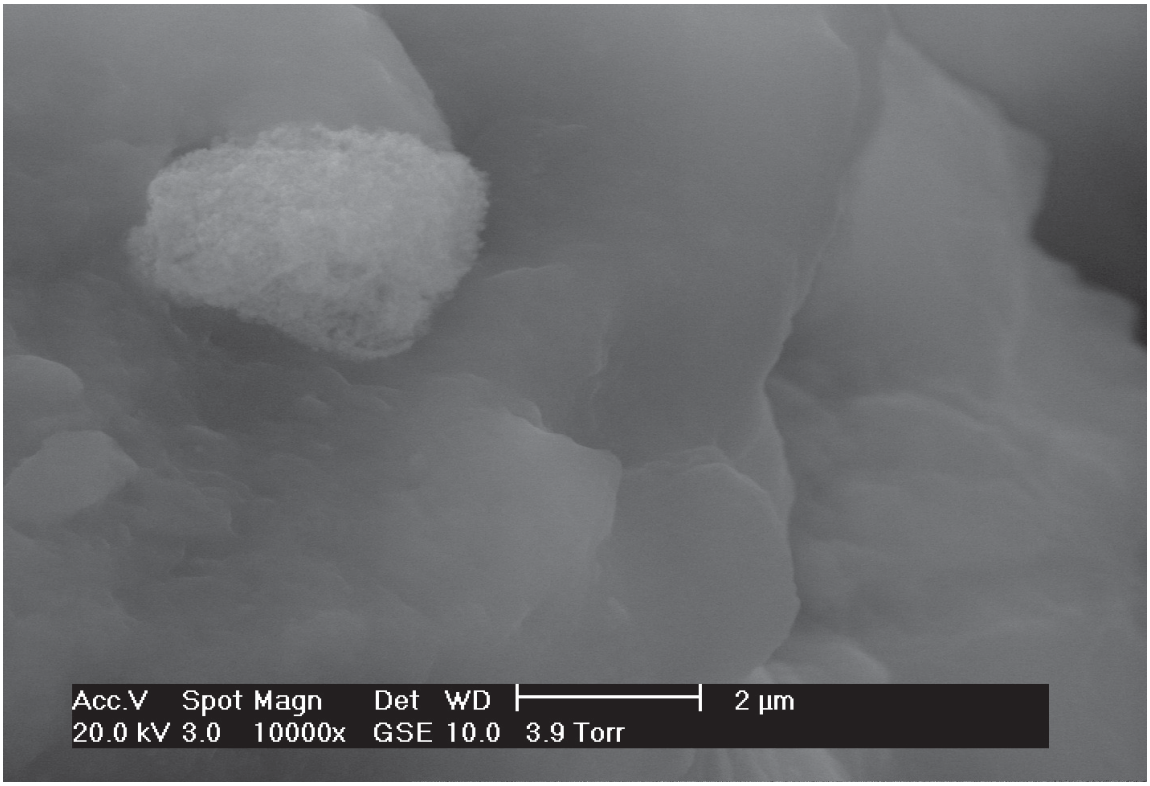

Figure 4–11: ESEM image of Au-Dox nanoparticles inside B16 tumours excised from a C57/BL6 mouse

4.4 Scanning Transmission Electron Microscopy of Gold Nanoparticles in Excised Mouse Tumours

To further investigate the *in vivo* presence of gold nanoparticles inside tumour cells, thin sectioning of the tumour samples was performed and used for scanning transmission electron microscopy (STEM) coupled with elemental microanalysis by energy-dispersive spectrometry (EDS). Typical STEM micrographs and accompanying EDS spectra are shown in Figure 4–12 and Figure 4–13. Table 4–2 shows a summary of the elemental makeup of the sample.

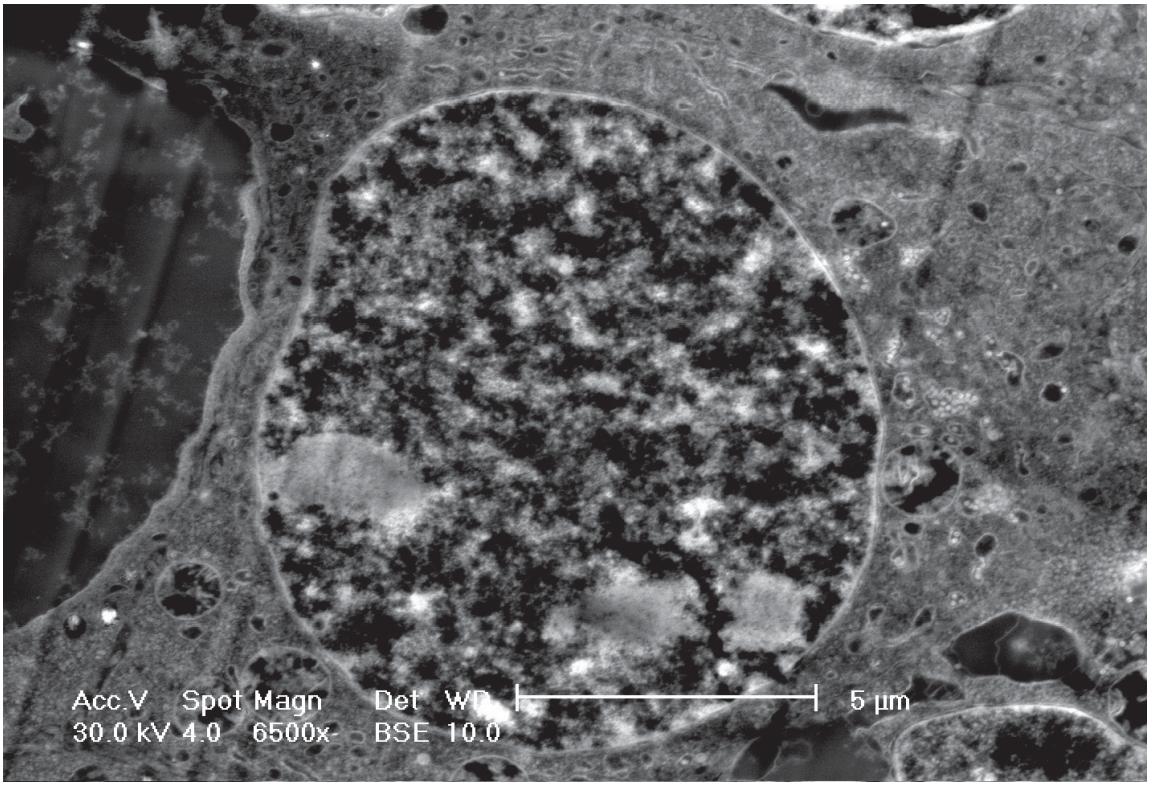

Figure 4–12: Typical STEM image of thin sections of Au-Dox treated B16 tumours excised from a C57/BL6 mouse.

Some STEM micrographs of potential gold nanoparticles were observed at high resolution such as the one shown in Figure 4–14. It was difficult to localize individual gold nanoparticles or clusters in the STEM micrographs as the resolution of the EDS mapping did not correlate to bright spots in the micrograph. However, EDS did confirm the presence of gold inside the B16 tumour thin sections, which supports that the gold nanoparticles were taken up into the tumour cells.

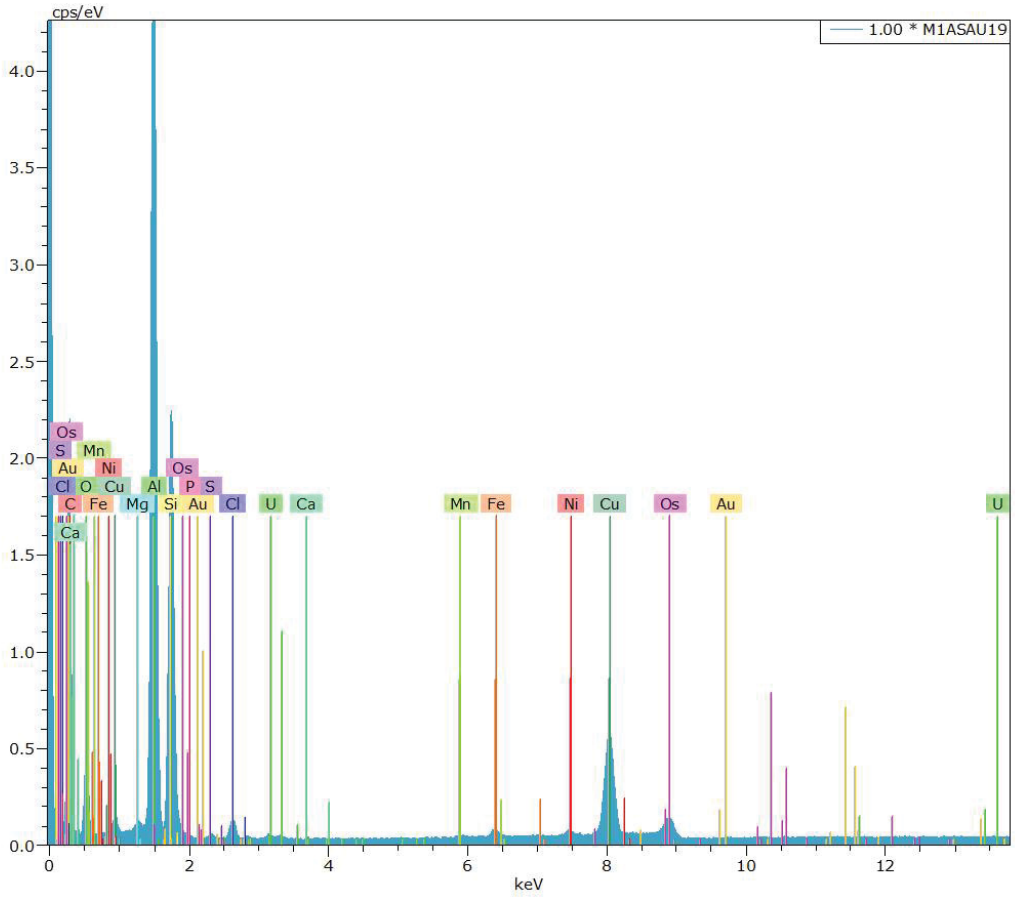

Figure 4–13: Accompanying EDS spectra of Figure 4–12 with a 30 kV electron beam, acquisition time of approximately 6 minutes for a total of n >10,000 counts

Table 4–2: Summary of the Elemental Composition of Sample from Figure 4–12

Element	**Atomic Number**	**Series**	**Normalized concentration** [wt. %]	**Atomic concentration** [wt. %]	**Error (1σ)** [wt. %]
Aluminum	13	K-series	31.87	27.49	0.98
Carbon	6	K-series	23.51	45.56	0.74
Copper	29	K-series	17.47	6.40	0.56
Silicon	14	K-series	15.56	12.90	0.08
Osmium	76	L-series	3.47	0.42	0.38
Oxygen	8	K-series	3.35	4.87	0.13
Nickel	28	K-series	1.26	0.50	0.07
Iron	26	K-series	0.95	0.40	0.06
Chlorine	17	K-series	0.94	0.62	0.06
Magnesium	12	K-series	0.41	0.39	0.04
Uranium	92	L-series	0.30	0.03	0.07
Gold	79	L-series	0.28	0.03	0.06
Manganese	25	K-series	0.24	0.10	0.04
Sulphur	16	K-series	0.21	0.15	0.03
Phosphorus	15	K-series	0.12	0.09	0.03
Calcium	20	K-series	0.06	0.04	0.03
		Total:	**100.00**	**100.00**	

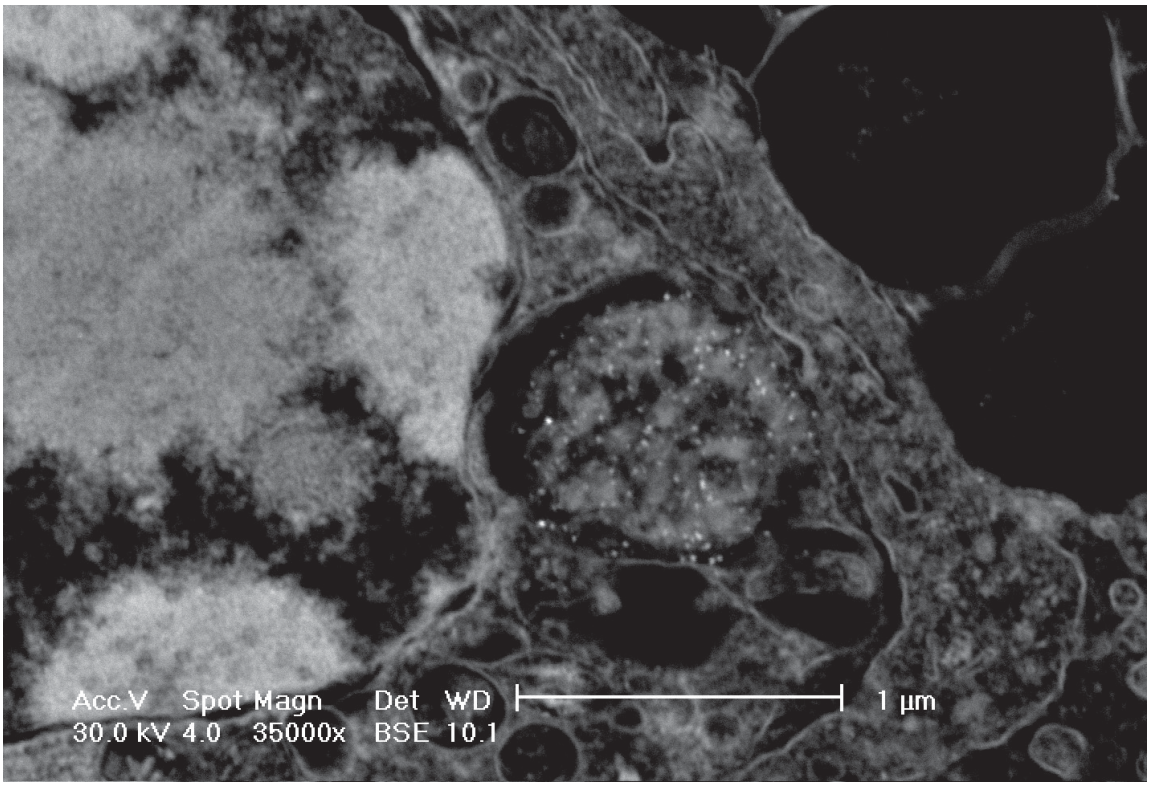

Figure 4–14: STEM image of potential gold nanoparticles inside thin sections of Au-Dox treated B16 tumours excised from a C57/BL6 mouse

CHAPTER 5
Conclusions

The goals of my research as presented in this thesis are to investigate the enhanced permeability and retention effect of ultrasmall gold nanoparticles in cancer as well as to develop new methods of quantifying their biodistribution using microscopy and imaging techniques. The advantages of developing multifunctional nanoparticles as both drug delivery and imaging contrast agents for simultaneous cancer treatment and diagnosis are examined in great detail. A thorough review of current strategies in the literature for targeting and imaging in nanomedicine further demonstrates the significance for this project.

The methodology for the synthesis and bioconjugation of gold nanoparticles and conjugates in this project is optimized and discussed. Various characterization methods, including zeta potential measurement and gel electrophoresis, are developed and utilized to confirm bioconjugation success. A wide variety of optical, electron, and acoustic imaging and microscopy techniques are used to investigate the *in vitro* cell uptake and *in vivo* biodistribution of gold nanoparticle conjugates.

The EPR effect is investigated by comparing the biodistribution of PEGylated and non-PEGylated Au-peptide conjugates in C57/BL6 mice at various time points by ICPMS. The ICPMS biodistribution results showed that PEGylation and peptide-conjugation improved the delivery of gold nanoparticles to the tumour albeit not to statistically significant levels. To this end, the results suggest that the enhanced

permeability and retention effect supplemented by the stealth capabilities of PEGylation and the active targeting by the investigated peptide sequences (FREG, MSH, myxoma, and cRGD) are both valid targeting strategies for ultrasmall gold nanoparticles. Peptide-conjugation to Myx and cRGD was shown to decrease the non-specific targeting to the spleen and liver, as well as modulate the excretion of the nanoparticles to the more preferable renal clearance. These observations suggest that the presence of peptide active targeting moieties on nanoparticles are of therapeutic and pharmacological importance. Follow-up work with normalized ligand and active targeting moiety density on nanoparticles may elucidate whether EPR accumulation of nanomaterials is different than targetted accumulation. Furthermore, a thorough multi-variate statistical model would be useful in finding evidence in support of a time-dependent two-phase clearance involving renal and RES mechanisms, which could have implications in medical scenarios other than cancer involving elevated macrophage activity such as inflammation and diseases with impaired autoimmune responses.

Microscopy and imaging-based techniques to determine the localization of gold nanoparticles *in vitro* and *in vivo* are explored. The biodistribution of gold nanoparticles by fluorescence imaging and photoacoustic imaging of gold nanoparticles in excised organs correlated well with the ICPMS data. There was also good agreement between the two imaging modalities at the sub-organ level of nanoparticle localization. However, more work needs to be done to translate the correlative imaging of gold nanoparticles to an *in vivo* quantitative real-time technique. At the cellular level, both environmental scanning electron microscopy and scanning transmission

electron microscopy showed evidence of gold nanoparticles inside cancer cells. All of these results demonstrate that gold nanoparticles can be visualized with many different techniques and these should be leveraged in cancer diagnosis by imaging.

Appendix

Table 5–1: Tabularized breakdown of Au (in dose percent mass) per solid organ and time point for Au, Au-PEG, Au-Myx, Au-PEG-Myx, Au-cRGD, and Au-PEG-cRGD conjugates, shown as mean ± SEM with n=3

		Heart	Lungs	Liver	Spleen	Pancreas	Kidneys	Tumour	Brain
Au	**4 h**	0.0227±0.0161	0.0558±0.0217	1.421±0.239	0.0142±0.00199	0.0347±0.00665	0.484±0.156	0.963±0.195	0.00772±0.000489
	24 h	0.0059±0.0033	0.0503±0.0194	1.676±0.392	0.0701±0.02109	0.0362±0.01686	0.419±0.141	1.139±0.290	0.00263±0.001893
	72 h	0.0258±0.0120	0.0843±0.0228	2.544±0.336	0.1503±0.01029	0.0333±0.00714	0.363±0.147	1.480±0.377	0.00069±0.000402
Au-PEG	**4 h**	0.4589±0.1150	0.8696±0.3058	4.529±1.220	0.2761±0.02649	0.1241±0.00677	0.794±0.166	1.663±1.254	0.04102±0.000508
	24 h	0.0190±0.0041	0.1461±0.0360	3.950±0.496	0.1759±0.03839	0.0668±0.01453	1.001±0.477	1.672±1.070	0.01353±0.002379
	72 h	0.0241±0.0135	0.1380±0.0213	1.928±0.263	0.1122±0.01155	0.0564±0.01040	0.490±0.125	1.570±0.752	0.00488±0.001091
Au-Myx	**4 h**	0.0482±0.0207	0.2188±0.0798	1.563±0.039	0.0442±0.01757	0.0625±0.02774	1.153±0.698	1.141±0.084	0.03462±0.005419
	24 h	0.0289±0.0159	0.0432±0.0049	1.851±0.022	0.0828±0.04622	0.0355±0.00534	1.612±0.785	1.641±0.472	0.01577±0.003502
	72 h	0.0106±0.0054	0.1154±0.0042	1.643±0.281	0.0989±0.00993	0.0488±0.00497	0.772±0.317	1.694±0.180	0.00471±0.001230
Au-PEG-Myx	**4 h**	0.2272±0.1681	0.5463±0.2261	3.153±0.963	0.1641±0.01826	0.1385±0.02958	0.976±0.390	0.755±0.403	0.03435±0.005280
	24 h	0.0668±0.0196	0.1637±0.0411	3.067±0.448	0.2030±0.01792	0.0566±0.00804	0.350±0.155	2.182±0.214	0.01349±0.001953
	72 h	0.0287±0.0214	0.0977±0.0077	1.850±0.648	0.2352±0.02755	0.0396±0.00404	0.723±0.455	1.346±0.362	0.00203±0.001689
Au-cRGD	**4 h**	0.0297±0.0096	0.2701±0.1821	1.374±0.534	0.0304±0.01688	0.0423±0.01947	0.229±0.091	0.668±0.230	0.02256±0.011374
	24 h	0.0351±0.0172	0.0915±0.0291	1.957±0.222	0.0501±0.00406	0.0489±0.01268	0.568±0.407	1.756±0.271	0.01233±0.002363
	72 h	0.0065±0.0044	0.0593±0.0096	1.624±0.549	0.0838±0.02899	0.0306±0.01139	0.245±0.089	0.970±0.256	0.00149±0.000759
Au-PEG-cRGD	**4 h**	0.0832±0.0371	0.4033±0.1482	3.464±0.723	0.1563±0.01314	0.1052±0.00509	0.461±0.205	0.755±0.403	0.04445±0.012115
	24 h	0.0669±0.0270	0.1745±0.0486	1.593±0.251	0.2379±0.06597	0.0675±0.01497	0.301±0.125	0.820±0.300	0.00759±0.001303
	72 h	0.0344±0.0218	0.1061±0.0156	2.399±0.923	0.3036±0.07921	0.0540±0.01241	0.838±0.308	1.577±0.251	0.00562±0.001867

References

[1] Frank Alexis, Eric Pridgen, Linda K. Molnar, and Omid C. Farokhzad. Factors affecting the clearance and biodistribution of polymeric nanoparticles. *Molecular Pharmaceutics*, 5(4):505–515, 2008.

[2] Yechezkel (Chezy) Barenholz. Doxil the first FDA-approved nano-drug: Lessons learned. *Journal of Controlled Release*, 160(2):117 – 134, 2012. Past, current and future applications of liposomes - Grand Challenges and Opportunities in Nanomedicine.

[3] Jana Drbohlavova, Jana Chomoucka, Vojtech Adam, Marketa Ryvolova, Tomas Eckschlager, Jaromir Hubalek, and Rene Kizek. Nanocarriers for anticancer drugs-new trends in nanomedicine. *Current drug metabolism*, 14(5):547–564, 2013.

[4] Ruth Duncan. Polymer conjugates as anticancer nanomedicines. *Nature Reviews Cancer*, 6(9):688–701, 2006.

[5] Larken E Euliss, Julie A DuPont, Stephanie Gratton, and Joseph DeSimone. Imparting size, shape, and composition control of materials for nanomedicine. *Chemical Society Reviews*, 35(11):1095–1104, 2006.

[6] Wen Jiang, Betty YS Kim, James T Rutka, and Warren CW Chan. Nanoparticle-mediated cellular response is size-dependent. *Nature nanotechnology*, 3(3):145–150, 2008.

[7] Sarah D Brown, Paola Nativo, Jo-Ann Smith, David Stirling, Paul R Edwards, Balaji Venugopal, David J Flint, Jane A Plumb, Duncan Graham, and Nial J Wheate. Gold nanoparticles for the improved anticancer drug delivery of the active component of oxaliplatin. *Journal of the American Chemical Society*, 132(13):4678–4684, 2010.

[8] Ming-Jium Shieh, Chia-Yen Hsu, Ling-Yi Huang, Hsuan-Ying Chen, Fei-Hong Huang, and Ping-Shan Lai. Reversal of doxorubicin-resistance by multifunctional nanoparticles in MCF-7/ADR cells. *Journal of controlled release*, 152(3):418–425, 2011.

[9] Xuan Zhang, Hicham Chibli, Randall Mielke, and Jay Nadeau. Ultrasmall gold- doxorubicin conjugates rapidly kill apoptosis-resistant cancer cells. *Bioconjugate chemistry*, 22(2):235–243, 2010.

[10] M Caraglia, G De Rosa, G Salzano, D Santini, M Lamberti, P Sperlongano, A Lombardi, A Abbruzzese, and R Addeo. Nanotech revolution for the anticancer drug delivery through blood-brain-barrier. *Current cancer drug targets*, 12(3):186–196, 2012.

[11] Forrest M Kievit and Miqin Zhang. Cancer nanotheranostics: improving imaging and therapy by targeted delivery across biological barriers. *Advanced Materials*, 23(36):H217–H247, 2011.

[12] Wim H De Jong, Werner I Hagens, Petra Krystek, Marina C Burger, Adriënne JAM Sips, and Robert E Geertsma. Particle size-dependent organ distribution of gold nanoparticles after intravenous administration. *Biomaterials*, 29(12):1912–1919, 2008.

[13] Anne-Charlotte Faure, Sandrine Dufort, Veronique Josserand, Pascal Perriat, Jean-Luc Coll, Stephane Roux, and Olivier Tillement. Control of the in vivo biodistribution of hybrid nanoparticles with different poly (ethylene glycol) coatings. *Small*, 5(22):2565–2575, 2009.

[14] Yan Geng, Paul Dalhaimer, Shenshen Cai, Richard Tsai, Manorama Tewari, Tamara Minko, and Dennis E Discher. Shape effects of filaments versus spherical particles in flow and drug delivery. *Nature Nanotechnology*, 2(4):249–255, 2007.

[15] Anna Samia, Smita Dayal, and Clemens Burda. Quantum dot-based energy transfer: Perspectives and potential for applications in photodynamic therapy. *Photochemistry and photobiology*, 82(3):617–625, 2006.

[16] Anna CS Samia, Xiaobo Chen, and Clemens Burda. Semiconductor quantum dots for photodynamic therapy. *Journal of the American Chemical Society*, 125(51):15736–15737, 2003.

[17] Jiong Ma, Ji-Yao Chen, Mopelola Idowu, and Tebello Nyokong. Generation of singlet oxygen via the composites of water-soluble thiol-capped CdTe quantum dots sulfonated aluminum phthalocyanines. *The Journal of Physical Chemistry B*, 112(15):4465–4469, 2008.

[18] S Shankara Narayanan, Sudarson Sekhar Sinha, and Samir Kumar Pal. Sensitized emission from a chemotherapeutic drug conjugated to CdSe/ZnS QDs. *The Journal of Physical Chemistry C*, 112(33):12716–12720, 2008.

[19] Lixin Shi, Billy Hernandez, and Matthias Selke. Singlet oxygen generation from water-soluble quantum dot-organic dye nanocomposites. *Journal of the American Chemical Society*, 128(19):6278–6279, 2006.

[20] James M Tsay, Michael Trzoss, Lixin Shi, Xiangxu Kong, Matthias Selke, Michael E Jung, and Shimon Weiss. Singlet oxygen production by peptide-coated quantum dot-photosensitizer conjugates. *Journal of the American Chemical Society*, 129(21):6865–6871, 2007.

[21] Nina Gomez-Blanco et al. Effective photoreduction of a Pt (IV) complex with quantum dots: a feasible new light-induced method of releasing anticancer Pt (II) drugs. *Chemical Communications*, pages 5257–5259, 2009.

[22] N Narband, M Mubarak, D Ready, IP Parkin, SP Nair, MA Green, A Beeby, and M Wilson. Quantum dots as enhancers of the efficacy of bacterial lethal photosensitization. *Nanotechnology*, 19(44):445102, 2008.

[23] Samuel J Clarke, C Annette Hollmann, Zhijun Zhang, Diana Suffern, Stephen E Bradforth, Nada M Dimitrijevic, William G Minarik, and Jay L Nadeau. Photophysics of dopamine-modified quantum dots and effects on biological systems. *Nature materials*, 5(5):409–417, 2006.

[24] Pawel Mroz, Ying-Ying Huang, Angelika Szokalska, Timur Zhiyentayev, Sahar Janjua, Artemissia-Phoebe Nifli, Margaret E Sherwood, Christian Ruzié, K Eszter Borbas, Dazhong Fan, et al. Stable synthetic bacteriochlorins overcome the resistance of melanoma to photodynamic therapy. *The FASEB Journal*, 24(9):3160–3170, 2010.

[25] De Gao, Rodney R Agayan, Hao Xu, Martin A Philbert, and Raoul Kopelman. Nanoparticles for two-photon photodynamic therapy in living cells. *Nano letters*, 6(11):2383–2386, 2006.

[26] Kazuya Ogawa and Yoshiaki Kobuke. Recent advances in two-photon photodynamic therapy. *Anti-Cancer Agents in Medicinal Chemistry (Formerly Current Medicinal Chemistry-Anti-Cancer Agents)*, 8(3):269–279, 2008.

[27] Jean R Starkey, Aleksander K Rebane, Mikhail A Drobizhev, Fanqing Meng, Aijun Gong, Aleisha Elliott, Kate McInnerney, and Charles W Spangler. New two-photon activated photodynamic therapy sensitizers induce xenograft tumor regressions after near-IR laser treatment through the body of the host mouse. *Clinical Cancer Research*, 14(20):6564–6573, 2008.

[28] Mikhail Drobizhev, Fanqing Meng, Aleksander Rebane, Yuriy Stepanenko, Eric Nickel, and Charles W Spangler. Strong two-photon absorption in new asymmetrically substituted porphyrins: interference between charge-transfer and intermediate-resonance pathways. *The Journal of Physical Chemistry B*, 110(20):9802–9814, 2006.

[29] Daniel R Larson, Warren R Zipfel, Rebecca M Williams, Stephen W Clark, Marcel P Bruchez, Frank W Wise, and Watt W Webb. Water-soluble quantum dots for multiphoton fluorescence imaging in vivo. *Science*, 300(5624):1434–1436, 2003.

[30] Dhruba J Bharali, Derrick W Lucey, Harishankar Jayakumar, Haridas E Pudavar, and Paras N Prasad. Folate-receptor-mediated delivery of InP quantum dots for bioimaging using confocal and two-photon microscopy. *Journal of the American Chemical Society*, 127(32):11364–11371, 2005.

[31] Devika B Chithrani, Salomeh Jelveh, Farid Jalali, Monique van Prooijen, Christine Allen, Robert G Bristow, Richard P Hill, and David A Jaffray. Gold nanoparticles as radiation sensitizers in cancer therapy. *Radiation research*, 173(6):719–728, 2010.

[32] Anil K Pradhan, Sultana N Nahar, Maximiliano Montenegro, Yan Yu, HL Zhang, Chiranjib Sur, Michael Mrozik, and Russell M Pitzer. Resonant x-ray enhancement of the auger effect in high-z atoms, molecules, and nanoparticles: Potential biomedical applications. *The Journal of Physical Chemistry A*, 113(45):12356–12363, 2009.

[33] D. M. Herold, I. J. Das, C. C. Stobbe, R. V. Iyer, and J. D. Chapman. Gold microspheres: a selective technique for producing biologically effective dose

enhancement. *International Journal of Radiation Biology*, 76(10):1357–1364, 2000.

[34] Xiao-Dong Zhang, Mei-Li Guo, Hong-Ying Wu, Yuan-Ming Sun, Yan-Qiu Ding, Xin Feng, and Liang-An Zhang. Irradiation stability and cytotoxicity of gold nanoparticles for radiotherapy. *International journal of nanomedicine*, 4:165, 2009.

[35] Michael KK Leung, James CL Chow, B Devika Chithrani, Martin JG Lee, Barbara Oms, and David A Jaffray. Irradiation of gold nanoparticles by x-rays: Monte carlo simulation of dose enhancements and the spatial properties of the secondary electrons production. *Medical physics*, 38(2):624–631, 2011.

[36] Sang Hyun Cho, Bernard L Jones, and Sunil Krishnan. The dosimetric feasibility of gold nanoparticle-aided radiation therapy (GNRT) via brachytherapy using low-energy gamma-/x-ray sources. *Physics in medicine and biology*, 54(16):4889, 2009.

[37] Frank Van den Heuvel, Jean-Pierre Locquet, and Sandra Nuyts. Beam energy considerations for gold nano-particle enhanced radiation treatment. *Physics in medicine and biology*, 55(16):4509, 2010.

[38] Xiaohua Huang, Xianghong Peng, Yiqing Wang, Yuxiang Wang, Dong M Shin, Mostafa A El-Sayed, and Shuming Nie. A reexamination of active and passive tumor targeting by using rod-shaped gold nanocrystals and covalently conjugated peptide ligands. *ACS nano*, 4(10):5887–5896, 2010.

[39] Shih-Hsun Cheng and Leu-Wei Lo. Inorganic nanoparticles for enhanced photodynamic cancer therapy. *Current drug discovery technologies*, 8(3):269–276, 2011.

[40] Brian W Pogue, Julia A OHara, Eugene Demidenko, Carmen M Wilmot, Isak A Goodwin, Bin Chen, Harold M Swartz, and Tayyaba Hasan. Photodynamic therapy with verteporfin in the radiation-induced fibrosarcoma-1 tumor causes enhanced radiation sensitivity. *Cancer research*, 63(5):1025–1033, 2003.

[41] SJP Damment, C Beevers, and DG Gatehouse. Evaluation of the potential genotoxicity of the phosphate binder lanthanum carbonate. *Mutagenesis*, 20(1):29–37, 2005.

[42] Ivan H El-Sayed, Xiaohua Huang, and Mostafa A El-Sayed. Selective laser photo-thermal therapy of epithelial carcinoma using anti-EGFR antibody conjugated gold nanoparticles. *Cancer letters*, 239(1):129–135, 2006.

[43] Xiaohua Huang, Prashant K Jain, Ivan H El-Sayed, and Mostafa A El-Sayed. Plasmonic photothermal therapy (PPTT) using gold nanoparticles. *Lasers in medical science*, 23(3):217–228, 2008.

[44] Younan Xia, Weiyang Li, Claire M Cobley, Jingyi Chen, Xiaohu Xia, Qiang Zhang, Miaoxin Yang, Eun Chul Cho, and Paige K Brown. Gold nanocages: from synthesis to theranostic applications. *Accounts of chemical research*, 44(10):914–924, 2011.

[45] Sara E Skrabalak, Jingyi Chen, Yugang Sun, Xianmao Lu, Leslie Au, Claire M Cobley, and Younan Xia. Gold nanocages: synthesis, properties, and applications. *Accounts of chemical research*, 41(12):1587–1595, 2008.

[46] Yucai Wang, Kvar CL Black, Hannah Luehmann, Weiyang Li, Yu Zhang, Xin Cai, Dehui Wan, Si-Yun Liu, Max Li, Paul Kim, et al. Comparison study of gold nanohexapods, nanorods, and nanocages for photothermal cancer treatment. *ACS nano*, 7(3):2068–2077, 2013.

[47] Won Il Choi, Abhishek Sahu, Young Ha Kim, and Giyoong Tae. Photothermal cancer therapy and imaging based on gold nanorods. *Annals of biomedical engineering*, 40(2):534–546, 2012.

[48] Claire M Cobley, Leslie Au, Jingyi Chen, and Younan Xia. Targeting gold nanocages to cancer cells for photothermal destruction and drug delivery. *Expert opinion on drug delivery*, 7(5):577–587, 2010.

[49] Leslie Au, Desheng Zheng, Fei Zhou, Zhi-Yuan Li, Xingde Li, and Younan Xia. A quantitative study on the photothermal effect of immuno gold nanocages targeted to breast cancer cells. *Acs Nano*, 2(8):1645–1652, 2008.

[50] Joshua T Robinson, Kevin Welsher, Scott M Tabakman, Sarah P Sherlock, Hailiang Wang, Richard Luong, and Hongjie Dai. High performance in vivo near-IR (> 1 μm) imaging and photothermal cancer therapy with carbon nanotubes. *Nano research*, 3(11):779–793, 2010.

[51] Feifan Zhou, Shengnan Wu, Baoyan Wu, Wei R Chen, and Da Xing. Mitochondria-targeting single-walled carbon nanotubes for cancer photothermal therapy. *Small*, 7(19):2727–2735, 2011.

[52] Luís FF Neves, John J Krais, Brent D Van Rite, Rajagopal Ramesh, Daniel E Resasco, and Roger G Harrison. Targeting single-walled carbon nanotubes for the treatment of breast cancer using photothermal therapy. *Nanotechnology*, 24(37):375104, 2013.

[53] Jing-Liang Li, Xue-Liang Hou, Hong-Chun Bao, Lu Sun, Bin Tang, Jin-Feng Wang, Xun-Gai Wang, and Min Gu. Graphene oxide nanoparticles for enhanced photothermal cancer cell therapy under the irradiation of a femtosecond laser beam. *Journal of Biomedical Materials Research Part A*, 2013.

[54] Haiyan Chen, Shulan Li, Bowen Li, Xueyan Ren, Shengnan Li, Didel M Mahounga, Sisi Cui, Yueqing Gu, and Samuel Achilefu. Folate-modified gold nanoclusters as near-infrared fluorescent probes for tumor imaging and therapy. *Nanoscale*, 4(19):6050–6064, 2012.

[55] Aili Zhang, Yu Tu, Songbing Qin, Yan Li, Juying Zhou, Na Chen, Qiang Lu, and Bingbo Zhang. Gold nanoclusters as contrast agents for fluorescent and x-ray dual-modality imaging. *Journal of colloid and interface science*, 372(1):239–244, 2012.

[56] Yongdong Jin and Xiaohu Gao. Plasmonic fluorescent quantum dots. *Nature nanotechnology*, 4(9):571–576, 2009.

[57] Ying Zhang, Shao-Ning Wang, Song Ma, Jiao-Jiao Guan, Da Li, Xiang-Dong Zhang, and Zhi-Dong Zhang. Self-assembly multifunctional nanocomposites with Fe_3O_4 magnetic core and CdSe/ZnS quantum dots shell. *Journal of Biomedical Materials Research Part A*, 85(3):840–846, 2008.

[58] Shiyong Yu, Jing Zhao, and Hai-Quan Su. Optical and magnetic properties of zinc oxide quantum dots doped with cobalt and lanthanum. *Journal of nanoscience and nanotechnology*, 13(6):4066–4071, 2013.

[59] Amit Ranjan Maity, Sharbari Palmal, SK Basiruddin, Niladri Sekhar Karan, Suresh Sarkar, Narayan Pradhan, and Nikhil R Jana. Doped semiconductor nanocrystal based fluorescent cellular imaging probes. *Nanoscale*, 5(12):5506–5513, 2013.

[60] Dominik Jańczewski, Yan Zhang, Gautom Kumar Das, Dong Kee Yi, Parasuraman Padmanabhan, Kishore K Bhakoo, Timothy Thatt Yang Tan, and Subramanian Tamil Selvan. Bimodal magnetic–fluorescent probes for bioimaging. *Microscopy research and technique*, 74(7):563–576, 2011.

[61] G Ferro-Flores, B E Ocampo-García, C L Santos-Cuevas, E Morales-Avila, and E Azorín-Vega. Multifunctional radiolabeled nanoparticles for targeted therapy. *Current medicinal chemistry*, 21(1):124–138, 2014.

[62] Jin-Ming Li, Yuan-Yuan Wang, Mei-Xia Zhao, Cai-Ping Tan, Yi-Qun Li, Xue-Yi Le, Liang-Nian Ji, and Zong-Wan Mao. Multifunctional QD-based co-delivery of siRNA and doxorubicin to HeLa cells for reversal of multidrug resistance and real-time tracking. *Biomaterials*, 33(9):2780–2790, 2012.

[63] Pavel Zrazhevskiy and Xiaohu Gao. Multifunctional quantum dots for personalized medicine. *Nano Today*, 4(5):414–428, 2009.

[64] A Mukerjee, A P Ranjan, and J K Vishwanatha. Combinatorial nanoparticles for cancer diagnosis and therapy. *Current medicinal chemistry*, 19(22):3714–3721, 2012.

[65] Chih-Jen Wen, Calvin T Sung, Ibrahim A Aljuffali, Yu-Jie Huang, and Jia-You Fang. Nanocomposite liposomes containing quantum dots and anticancer drugs for bioimaging and therapeutic delivery: a comparison of cationic, pegylated and deformable liposomes. *Nanotechnology*, 24(32):325101, 2013.

[66] Chih-Jen Wen, Li-Wen Zhang, Saleh A Al-Suwayeh, Tzu-Chen Yen, and Jia-You Fang. Theranostic liposomes loaded with quantum dots and apomorphine for brain targeting and bioimaging. *International journal of nanomedicine*, 7:1599, 2012.

[67] Ki Hyun Bae, Jeong Yu Lee, Soo Hyeon Lee, Tae Gwan Park, and Yoon Sung Nam. Optically traceable solid lipid nanoparticles loaded with siRNA and paclitaxel for synergistic chemotherapy with in situ imaging. *Advanced healthcare materials*, 2(4):576–584, 2013.

[68] Francesco Canfarotta, Michael J Whitcombe, and Sergey A Piletsky. Polymeric nanoparticles for optical sensing. *Biotechnology advances*, 31(8):1585–1599, 2013.

[69] Yun-Long Wu, Hui Yin, Feng Zhao, and Jun Li. Multifunctional hybrid nanocarriers consisting of supramolecular polymers and quantum dots for simultaneous dual therapeutics delivery and cellular imaging. *Advanced healthcare materials*, 2(2):297–301, 2013.

[70] Shihui Wen, Hui Liu, Hongdong Cai, Mingwu Shen, and Xiangyang Shi. Targeted and pH-responsive delivery of doxorubicin to cancer cells using multifunctional dendrimer-modified multi-walled carbon nanotubes. *Advanced healthcare materials*, 2(9):1267–1276, 2013.

[71] Mei-Ling Chen, Ye-Ju He, Xu-Wei Chen, and Jian-Hua Wang. Quantum dots conjugated with Fe_3O_4-filled carbon nanotubes for cancer-targeted imaging and magnetically guided drug delivery. *Langmuir*, 28(47):16469–16476, 2012.

[72] L Minati, V Antonini, M Dalla Serra, and G Speranza. Multifunctional branched gold–carbon nanotube hybrid for cell imaging and drug delivery. *Langmuir*, 28(45):15900–15906, 2012.

[73] Bin Zhao, Juan Yan, Dongfang Wang, Zhilei Ge, Shijiang He, Dannong He, Shiping Song, and Chunhai Fan. Carbon nanotubes multifunctionalized by rolling circle amplification and their application for highly sensitive detection of cancer markers. *Small*, 9(15):2595–2601, 2013.

[74] Dhruba J. Bharali and Shaker A. Mousa. Emerging nanomedicines for early cancer detection and improved treatment: Current perspective and future promise. *Pharmacology & Therapeutics*, 128(2):324 – 335, 2010.

[75] Ki Young Choi, Gang Liu, Seulki Lee, and Xiaoyuan Chen. Theranostic nanoplatforms for simultaneous cancer imaging and therapy: current approaches and future perspectives. *Nanoscale*, 4:330–342, 2012.

[76] John V. Frangioni. New technologies for human cancer imaging. *Journal of Clinical Oncology*, 26(24):4012–4021, 2008.

[77] Ruth Etzioni, Nicole Urban, Scott Ramsey, Martin McIntosh, Stephen Schwartz, Brian Reid, Jerald Radich, Garnet Anderson, and Leland Hartwell. The case for early detection. *Nature Reviews Cancer*, 3(4):243–252, 2003.

[78] Benjamin J Vakoc, Dai Fukumura, Rakesh K Jain, and Brett E Bouma. Cancer imaging by optical coherence tomography: preclinical progress and clinical potential. *Nature Reviews Cancer*, 12(5):363–368, 2012.

[79] Kalevi Kairemo, Paola Erba, Kim Bergstrm, and Ernest KJ Pauwels. Nanoparticles in cancer. *Current Radiopharmaceuticals*, 1(1):30–36, 2008.

[80] EM Sevick-Muraca. Translation of near-infrared fluorescence imaging technologies: emerging clinical applications. *Annual review of medicine*, 63:217–231, 2012.

[81] Marie-Ange DHallewin, Lina Bezdetnaya, and Franois Guillemin. Fluorescence detection of bladder cancer: A review. *European Urology*, 42(5):417 – 425, 2002.

[82] Yoko Kusunoki, Fumio Imamura, Hiroshi Uda, Masayuki Mano, and Takeshi Horai. Early detection of lung cancer with laser-induced fluorescence endoscopy and spectrofluorometry*. *CHEST Journal*, 118(6):1776–1782, 2000.

[83] Cristina A. Metildi, Robert M. Hoffman, and Michael Bouvet. Fluorescence-guided surgery and fluorescence laparoscopy for gastrointestinal cancers in clinically-relevant mouse models. *Gastroenterology Research and Practice*, 2013:8, 2013.

[84] Xiaoxiao He, Kemin Wang, and Zhen Cheng. In vivo near-infrared fluorescence imaging of cancer with nanoparticle-based probes. *Wiley Interdisciplinary Reviews: Nanomedicine and Nanobiotechnology*, 2(4):349–366, 2010.

[85] Ute Resch-Genger, Markus Grabolle, Sara Cavaliere-Jaricot, Roland Nitschke, and Thomas Nann. Quantum dots versus organic dyes as fluorescent labels. *Nature methods*, 5(9):763–775, 2008.

[86] Shenglin Luo, Erlong Zhang, Yongping Su, Tianmin Cheng, and Chunmeng Shi. A review of nir dyes in cancer targeting and imaging. *Biomaterials*, 32(29):7127–7138, 2011.

[87] Yi Zhang and Tza-Huei Wang. Quantum dot enabled molecular sensing and diagnostics. *Theranostics*, 2(7):631, 2012.

[88] Takahisa Omata, Yuki Tani, Satoshi Kobayashi, and Shinya Otsuka-Yao-Matsuo. Quantum dot phosphors and their application to inorganic electroluminescence device. *Thin Solid Films*, 520(10):3829–3834, 2012.

[89] Elsa Cassette, Marion Helle, Lina Bezdetnaya, Frdric Marchal, Benoit Dubertret, and Thomas Pons. Design of new quantum dot materials for deep tissue infrared imaging. *Advanced Drug Delivery Reviews*, 65(5):719–731, 2013.

[90] Hisataka Kobayashi, Yukihiro Hama, Yoshinori Koyama, Tristan Barrett, Celeste AS Regino, Yasuteru Urano, and Peter L Choyke. Simultaneous multicolor imaging of five different lymphatic basins using quantum dots. *Nano letters*, 7(6):1711–1716, 2007.

[91] Yan Li, Zhe Li, Xiaohui Wang, Fengjun Liu, Yingsheng Cheng, Bingbo Zhang, and Donglu Shi. In vivo cancer targeting and imaging-guided surgery with near infrared-emitting quantum dot bioconjugates. *Theranostics*, 2(8):769, 2012.

[92] Melanie Bottrill and Mark Green. Some aspects of quantum dot toxicity. *Chemical Communications*, 47(25):7039–7050, 2011.

[93] Virgilio Brunetti, Hicham Chibli, Roberto Fiammengo, Antonio Galeone, Maria Ada Malvindi, Giuseppe Vecchio, Roberto Cingolani, Jay L Nadeau, and Pier Paolo Pompa. InP/ZnS as a safer alternative to CdSe/ZnS core/shell quantum dots: in vitro and in vivo toxicity assessment. *Nanoscale*, 5(1):307–317, 2013.

[94] Ken-Tye Yong, Hong Ding, Indrajit Roy, Wing-Cheung Law, Earl J Bergey, Anirban Maitra, and Paras N Prasad. Imaging pancreatic cancer using bioconjugated InP quantum dots. *ACS nano*, 3(3):502–510, 2009.

[95] Markus Haase and Helmut Schfer. Upconverting nanoparticles. *Angewandte Chemie International Edition*, 50(26):5808–5829, 2011.

[96] Meng Wang, Gopal Abbineni, April Clevenger, Chuanbin Mao, and Shukun Xu. Upconversion nanoparticles: synthesis, surface modification and biological applications. *Nanomedicine: Nanotechnology, Biology and Medicine*, 7(6):710–729, 2011.

[97] Jos A. Barreto, William OMalley, Manja Kubeil, Bim Graham, Holger Stephan, and Leone Spiccia. Nanomaterials: Applications in cancer imaging and therapy. *Advanced Materials*, 23(12):H18–H40, 2011.

[98] Liqin Xiong, Zhigang Chen, Qiwei Tian, Tianye Cao, Congjian Xu, and Fuyou Li. High contrast upconversion luminescence targeted imaging in vivo using peptide-labeled nanophosphors. *Analytical Chemistry*, 81(21):8687–8694, 2009.

[99] Liyuan Pan, Meng He, Jiebing Ma, Wei Tang, Guo Gao, Rong He, Haichuan Su, and Daxiang Cui. Phase and size controllable synthesis of $NaYbF_4$ nanocrystals

in oleic acid/ionic liquid two-phase system for targeted fluorescent imaging of gastric cancer. *Theranostics*, 3(3):210, 2013.

[100] Lei Yin Ang, Meng Earn Lim, Li Ching Ong, and Yong Zhang. Applications of upconversion nanoparticles in imaging, detection and therapy. *Nanomedicine*, 6(7):1273–1288, 2011.

[101] Kai Li, Dan Ding, QiuLi Zhao, JingZhi Sun, BenZhong Tang, and Bin Liu. Biocompatible organic dots with aggregation-induced emission for in vitro and in vivo fluorescence imaging. *Science China Chemistry*, 56(9):1228–1233, 2013.

[102] Sarit Cohen and Shlomo Margel. Engineering of near IR fluorescent albumin nanoparticles for in vivo detection of colon cancer. *Journal of Nanobiotechnology*, 10(1):36, 2012.

[103] Antje Vollrath, Stephanie Schubert, and Ulrich S Schubert. Fluorescence imaging of cancer tissue based on metal-free polymeric nanoparticles - a review. *J. Mater. Chem. B*, 1(15):1994–2007, 2013.

[104] Malka Shilo, Tobi Reuveni, Menachem Motiei, and Rachela Popovtzer. Nanoparticles as computed tomography contrast agents: current status and future perspectives. *Nanomedicine*, 7(2):257–269, 2012.

[105] Hrvoje Lusic and Mark W Grinstaff. X-ray-computed tomography contrast agents. *Chemical reviews*, 113(3):1641–1666, 2012.

[106] JF Hainfeld, DN Slatkin, TM Focella, and HM Smilowitz. Gold nanoparticles: a new x-ray contrast agent. *British Journal of Radiology*, 79(939):248–253, 2006.

[107] Yanlan Liu, Kelong Ai, and Lehui Lu. Nanoparticulate x-ray computed tomography contrast agents: from design validation to in vivo applications. *Accounts of Chemical Research*, 45(10):1817–1827, 2012.

[108] Rachela Popovtzer, Ashish Agrawal, Nicholas A Kotov, Aron Popovtzer, James Balter, Thomas E Carey, and Raoul Kopelman. Targeted gold nanoparticles enable molecular CT imaging of cancer. *Nano letters*, 8(12):4593–4596, 2008.

[109] Tobi Reuveni, Menachem Motiei, Zimam Romman, Aron Popovtzer, and Rachela Popovtzer. Targeted gold nanoparticles enable molecular CT imaging of cancer: an in vivo study. *International journal of nanomedicine*, 6:2859, 2011.

[110] Oded Rabin, J Manuel Perez, Jan Grimm, Gregory Wojtkiewicz, and Ralph Weissleder. An x-ray computed tomography imaging agent based on long-circulating bismuth sulphide nanoparticles. *Nature materials*, 5(2):118–122, 2006.

[111] Kelong Ai, Yanlan Liu, Jianhua Liu, Qinghai Yuan, Yangyang He, and Lehui Lu. Large-scale synthesis of Bi_2S_3 nanodots as a contrast agent for in vivo x-ray computed tomography imaging. *Advanced Materials*, 23(42):4886–4891, 2011.

[112] Joseph M. Kinsella, Rebecca E. Jimenez, Priya P. Karmali, Anthony M. Rush, V. Ramana Kotamraju, Nathan C. Gianneschi, Erkki Ruoslahti, Dwayne Stupack, and Michael J. Sailor. X-ray computed tomography imaging of breast cancer by using targeted peptide-labeled bismuth sulfide nanoparticles. *Angewandte Chemie International Edition*, 50(51):12308–12311, 2011.

[113] Myoung Hwan Oh, Nohyun Lee, Hyoungsu Kim, Seung Pyo Park, Yuanzhe Piao, Jisoo Lee, Samuel Woojoo Jun, Woo Kyung Moon, Seung Hong Choi, and Taeghwan Hyeon. Large-scale synthesis of bioinert tantalum oxide nanoparticles for x-ray computed tomography imaging and bimodal image-guided sentinel lymph node mapping. *Journal of the American Chemical Society*, 133(14):5508–5515, 2011.

[114] Peter J. Bonitatibus, Andrew S. Torres, Binil Kandapallil, Brian D. Lee, Greg D. Goddard, Robert E. Colborn, and Michael E. Marino. Preclinical assessment of a zwitterionic tantalum oxide nanoparticle x-ray contrast agent. *ACS nano*, 6(8):6650–6658, 2012.

[115] Yanlan Liu, Kelong Ai, Jianhua Liu, Qinghai Yuan, Yangyang He, and Lehui Lu. A high-performance ytterbium-based nanoparticulate contrast agent for in vivo x-ray computed tomography imaging. *Angewandte Chemie International Edition*, 51(6):1437–1442, 2012.

[116] Yanlan Liu, Kelong Ai, Jianhua Liu, Qinghai Yuan, Yangyang He, and Lehui Lu. Hybrid $BaYbF_5$ nanoparticles: Novel binary contrast agent for high-resolution in vivo x-ray computed tomography angiography. *Advanced Healthcare Materials*, 1(4):461–466, 2012.

[117] Hyon Bin Na, In Chan Song, and Taeghwan Hyeon. Inorganic nanoparticles for MRI contrast agents. *Advanced Materials*, 21(21):2133–2148, 2009.

[118] Akira Ito and Masamichi Kamihira. Tissue engineering using magnetite nanoparticles. *Progress in molecular biology and translational science*, 104:355, 2011.

[119] Juan Gallo, Nicholas J. Long, and Eric O. Aboagye. Magnetic nanoparticles as contrast agents in the diagnosis and treatment of cancer. *Chem. Soc. Rev.*, 42:7816–7833, 2013.

[120] Akira Ito, Masashige Shinkai, Hiroyuki Honda, and Takeshi Kobayashi. Medical application of functionalized magnetic nanoparticles. *Journal of bioscience and bioengineering*, 100(1):1–11, 2005.

[121] Yi-Xiang J. Wang. Superparamagnetic iron oxide based MRI contrast agents: Current status of clinical application. *Quantitative Imaging in Medicine and Surgery*, 1(1):35–40, 2011.

[122] Jelle O Barentsz and Paris P Tekkis. *Use of USPIOs for Clinical Lymph Node Imaging*, volume 102 of *Fundamental Biomedical Technologies*, chapter 3, pages 25–40. Springer New York, 2008.

[123] Nohyun Lee and Taeghwan Hyeon. Designed synthesis of uniformly sized iron oxide nanoparticles for efficient magnetic resonance imaging contrast agents. *Chemical Society Reviews*, 41(7):2575–2589, 2012.

[124] Hui Xie, Yanhong Zhu, Weili Jiang, Qing Zhou, Hai Yang, Ning Gu, Yu Zhang, Huibi Xu, Haibo Xu, and Xiangliang Yang. Lactoferrin-conjugated superparamagnetic iron oxide nanoparticles as a specific MRI contrast agent for detection of brain glioma in vivo. *Biomaterials*, 32(2):495–502, 2011.

[125] Aniket S. Wadajkar, Jyothi U. Menon, Yuh-Shyan Tsai, Crystal Gore, Timothy Dobin, Leah Gandee, Kim Kangasniemi, Masaya Takahashi, Bikash Manandhar, Jung-Mo Ahn, Jer-Tsong Hsieh, and Kytai T. Nguyen. Prostate cancer-specific thermo-responsive polymer-coated iron oxide nanoparticles. *Biomaterials*, 34(14):3618–3625, 2013.

[126] Claire Corot and David Warlin. Superparamagnetic iron oxide nanoparticles for MRI: contrast media pharmaceutical company R&D perspective. *Wiley Interdisciplinary Reviews: Nanomedicine and Nanobiotechnology*, 5(5):411–422, 2013.

[127] Renata Madru, Pontus Kjellman, Fredrik Olsson, Karin Wingårdh, Christian Ingvar, Freddy Ståhlberg, Johan Olsrud, Jimmy Lätt, Sarah Fredriksson, and Linda Knutsson. ^{99m}Tc-labeled superparamagnetic iron oxide nanoparticles for multimodality SPECT/MRI of sentinel lymph nodes. *Journal of Nuclear Medicine*, 53(3):459–463, 2012.

[128] Qiang Ma, Yuko Nakane, Yuki Mori, Miyuki Hasegawa, Yoshichika Yoshioka, Tomonobu M. Watanabe, Kohsuke Gonda, Noriaki Ohuchi, and Takashi Jin. Multilayered, core/shell nanoprobes based on magnetic ferric oxide particles andquantum dots for multimodality imaging of breast cancer tumors. *Biomaterials*, 33(33):8486–8494, 2012.

[129] Neil Desai. Challenges in development of nanoparticle-based therapeutics. *The AAPS journal*, 14(2):282–295, 2012.

[130] Seyed Moien Moghimi, AC Hunter, and TL Andresen. Factors controlling nanoparticle pharmacokinetics: an integrated analysis and perspective. *Annual review of pharmacology and toxicology*, 52:481–503, 2012.

[131] Michelle Longmire, Peter L Choyke, and Hisataka Kobayashi. Clearance properties of nano-sized particles and molecules as imaging agents: considerations and caveats. *Future Medicine*, 2008.

[132] Zohreh Amoozgar and Yoon Yeo. Recent advances in stealth coating of nanoparticle drug delivery systems. *Wiley Interdisciplinary Reviews: Nanomedicine and Nanobiotechnology*, 4(2):219–233, 2012.

[133] Priya Prakash Karmali and Dmitri Simberg. Interactions of nanoparticles with plasma proteins: implication on clearance and toxicity of drug delivery systems. *Expert opinion on drug delivery*, 8(3):343–357, 2011.

[134] Alexandre Albanese, Peter S Tang, and Warren CW Chan. The effect of nanoparticle size, shape, and surface chemistry on biological systems. *Annual review of biomedical engineering*, 14:1–16, 2012.

[135] Rochelle R Arvizo, Oscar R Miranda, Daniel F Moyano, Chad A Walden, Karuna Giri, Resham Bhattacharya, J David Robertson, Vincent M Rotello, Joel M Reid, and Priyabrata Mukherjee. Modulating pharmacokinetics, tumor uptake and biodistribution by engineered nanoparticles. *PLoS One*, 6(9):e24374, 2011.

[136] Shawn J Tan, Michael J Campolongo, Dan Luo, and Wenlong Cheng. Building plasmonic nanostructures with dna. *Nature nanotechnology*, 6(5):268–276, 2011.

[137] Leonid Vigderman and Eugene R Zubarev. Starfruit-shaped gold nanorods and nanowires: synthesis and SERS characterization. *Langmuir*, 28(24):9034–9040, 2012.

[138] Hongyan Liang, David Rossouw, Haiguang Zhao, Scott K Cushing, Honglong Shi, Andreas Korinek, Hongxing Xu, Federico Rosei, Wenzhong Wang, Nianqiang Wu, et al. Asymmetric silver nanocarrot structures: Solution synthesis and their asymmetric plasmonic resonances. *Journal of the American Chemical Society*, 135(26):9616–9619, 2013.

[139] N Nixon Raj, J Brijitta, D Ramachandran, AM Rabel, and V Jayanthi. Synthesis and characterization of matryoshka doll-like silica nanoparticles. In *Advanced Nanomaterials and Emerging Engineering Technologies (ICANMEET), 2013 International Conference on*, pages 61–62. IEEE, 2013.

[140] Xiao Wang, Dapeng Liu, Shuyan Song, and Hongjie Zhang. Pt@CeO_2 multicore@shell self-assembled nanospheres: clean synthesis, structure optimization, and catalytic applications. *Journal of the American Chemical Society*, 135(42):15864–15872, 2013.

[141] Matthew R Jones, Robert J Macfarlane, Andrew E Prigodich, Pinal C Patel, and Chad A Mirkin. Nanoparticle shape anisotropy dictates the collective behavior of surface-bound ligands. *Journal of the American Chemical Society*, 133(46):18865–18869, 2011.

[142] Robert Vácha, Francisco J Martinez-Veracoechea, and Daan Frenkel. Receptor-mediated endocytosis of nanoparticles of various shapes. *Nano letters*, 11(12):5391–5395, 2011.

[143] Shikha Nangia and Radhakrishna Sureshkumar. Effects of nanoparticle charge and shape anisotropy on translocation through cell membranes. *Langmuir*, 28(51):17666–17671, 2012.

[144] B Devika Chithrani, Arezou A Ghazani, and Warren CW Chan. Determining the size and shape dependence of gold nanoparticle uptake into mammalian cells. *Nano letters*, 6(4):662–668, 2006.

[145] Julie A Champion and Samir Mitragotri. Role of target geometry in phagocytosis. *Proceedings of the National Academy of Sciences of the United States of America*, 103(13):4930–4934, 2006.

[146] Randall Toy, Pubudu M Peiris, Ketan B Ghaghada, and Efstathios Karathanasis. Shaping cancer nanomedicine: the effect of particle shape on the in vivo journey of nanoparticles. *Nanomedicine*, 9(1):121–134, 2014.

[147] Jifu Tan, Samar Shah, Antony Thomas, H Daniel Ou-Yang, and Yaling Liu. The influence of size, shape and vessel geometry on nanoparticle distribution. *Microfluidics and nanofluidics*, 14(1-2):77–87, 2013.

[148] Bryan Ronain Smith, Paul Kempen, Donna Bouley, Alexander Xu, Zhuang Liu, Nicholas Melosh, Hongjie Dai, Robert Sinclair, and Sanjiv Sam Gambhir. Shape matters: intravital microscopy reveals surprising geometrical dependence for nanoparticles in tumor models of extravasation. *Nano letters*, 12(7):3369–3377, 2012.

[149] MM Janát-Amsbury, A Ray, CM Peterson, H Ghandehari, et al. Geometry and surface characteristics of gold nanoparticles influence their biodistribution and uptake by macrophages. *European Journal of Pharmaceutics and Biopharmaceutics*, 77(3):417–423, 2011.

[150] Hans C Fischer and Warren CW Chan. Nanotoxicity: the growing need for in vivo study. *Current opinion in biotechnology*, 18(6):565–571, 2007.

[151] Nikolai Khlebtsov and Lev Dykman. Biodistribution and toxicity of engineered gold nanoparticles: a review of in vitro and in vivo studies. *Chemical Society Reviews*, 40(3):1647–1671, 2011.

[152] Lei Yu and Angelo Andriola. Quantitative gold nanoparticle analysis methods: A review. *Talanta*, 82(3):869–875, 2010.

[153] Chih-Ching Huang, Zusing Yang, Kun-Hong Lee, and Huan-Tsung Chang. Synthesis of highly fluorescent gold nanoparticles for sensing mercury (II). *Angewandte Chemie*, 119(36):6948–6952, 2007.

[154] Jinbin Liu, Mengxiao Yu, Chen Zhou, Shengyang Yang, Xuhui Ning, and Jie Zheng. Passive tumor targeting of renal-clearable luminescent gold nanoparticles: long tumor retention and fast normal tissue clearance. *Journal of the American Chemical Society*, 135(13):4978–4981, 2013.

[155] Edward A Sykes, Qin Dai, Kim M Tsoi, David M Hwang, and Warren CW Chan. Nanoparticle exposure in animals can be visualized in the skin and analysed via skin biopsy. *Nature communications*, 5, 2014.

[156] Shau-Chun Wang, Li-Kai Ho, Jiin-Cherng Yen, and Tung-Hu Tsai. An automated blood sampling system to measure lovastatin level in plasma and faeces. *Biomedical Chromatography*, 20(9):911–916, 2006.

[157] Bryce J Marquis, Sara A Love, Katherine L Braun, and Christy L Haynes. Analytical methods to assess nanoparticle toxicity. *Analyst*, 134(3):425–439, 2009.

[158] RK Jain. Delivery of molecular medicine to solid tumors: lessons from in vivo imaging of gene expression and function. *Journal of controlled release*, 74(1):7–25, 2001.

[159] H Maeda, J Wu, T Sawa, Y Matsumura, and K Hori. Tumor vascular permeability and the EPR effect in macromolecular therapeutics: a review. *Journal of controlled release*, 65(1):271–284, 2000.

[160] Yasuhiro Matsumura and Hiroshi Maeda. A new concept for macromolecular therapeutics in cancer chemotherapy: mechanism of tumoritropic accumulation of proteins and the antitumor agent smancs. *Cancer research*, 46(12-1):6387–6392, 1986.

[161] Tamara Minko, Pavla Kopečkova, Vitaliy Pozharov, Keith D Jensen, and Jindřich Kopeček. The influence of cytotoxicity of macromolecules and of VEGF gene modulated vascular permeability on the enhanced permeability and retention effect in resistant solid tumors. *Pharmaceutical research*, 17(5):505–514, 2000.

[162] Vikash P Chauhan, Triantafyllos Stylianopoulos, Yves Boucher, and Rakesh K Jain. Delivery of molecular and nanoscale medicine to tumors: transport barriers and strategies. *Annual review of chemical and biomolecular engineering*, 2:281–298, 2011.

[163] Ruth Duncan and Rogerio Gaspar. Nanomedicine(s) under the microscope. *Molecular pharmaceutics*, 8(6):2101–2141, 2011.

[164] Rakesh K Jain and Triantafyllos Stylianopoulos. Delivering nanomedicine to solid tumors. *Nature reviews clinical oncology*, 7(11):653–664, 2010.

[165] Uma Prabhakar, Hiroshi Maeda, Rakesh K Jain, Eva M Sevick-Muraca, William Zamboni, Omid C Farokhzad, Simon T Barry, Alberto Gabizon, Piotr Grodzinski, and David C Blakey. Challenges and key considerations of the enhanced permeability and retention effect for nanomedicine drug delivery in oncology. *Cancer research*, 73(8):2412–2417, 2013.

[166] Fortunato Ciardiello and Giampaolo Tortora. EGFR antagonists in cancer treatment. *New England Journal of Medicine*, 358(11):1160–1174, 2008.

[167] Hui Qiang Lin, Haider Meriaty, and Andrew Katsifis. Prediction of synergistic antitumour effect of gefitinib and radiation in vitro. *Anticancer research*, 31(9):2883–2888, 2011.

[168] Benjamin Solomon, Jim Hagekyriakou, Melanie K Trivett, Steven A Stacker, Grant A McArthur, and Carleen Cullinane. EGFR blockade with ZD1839 ("Iressa") potentiates the antitumor effects of single and multiple fractions of ionizing radiation in human A431 squamous cell carcinoma. *International Journal of Radiation Oncology Biology Physics*, 55(3):713–723, 2003.

[169] Jay Patrick Lopez, Jessica Wang-Rodriguez, Catherine Y Chang, Gabriel Sneh, Michael Andrew Yu, Francisco S Pardo, Joseph Aguilera, and Weg M Ongkeko. Gefitinib (Iressa) potentiates the effect of ionizing radiation in thyroid cancer cell lines. *The Laryngoscope*, 118(8):1372–1376, 2008.

[170] Cataldo Bianco, Giampaolo Tortora, Roberto Bianco, Roberta Caputo, Bianca Maria Veneziani, Rosa Caputo, Vincenzo Damiano, Teresa Troiani, Gabriella Fontanini, David Raben, et al. Enhancement of antitumor activity of ionizing radiation by combined treatment with the selective epidermal growth factor receptor-tyrosine kinase inhibitor ZD1839 (Iressa). *Clinical cancer research*, 8(10):3250–3258, 2002.

[171] Yanping Ding, Suping Li, and Guangjun Nie. Nanotechnological strategies for therapeutic targeting of tumor vasculature. *Nanomedicine*, 8(7):1209–1222, 2013.

[172] Paul J Carter and Peter D Senter. Antibody-drug conjugates for cancer therapy. *The Cancer Journal*, 14(3):154–169, 2008.

[173] Chung Hang J Choi, Christopher A Alabi, Paul Webster, and Mark E Davis. Mechanism of active targeting in solid tumors with transferrin-containing gold

nanoparticles. *Proceedings of the National Academy of Sciences*, 107(3):1235–1240, 2010.

[174] Sanjeeb K Sahoo and Vinod Labhasetwar. Enhanced antiproliferative activity of transferrin-conjugated paclitaxel-loaded nanoparticles is mediated via sustained intracellular drug retention. *Molecular pharmaceutics*, 2(5):373–383, 2005.

[175] Renee Brissette, John KA Prendergast, and Neil I Goldstein. Identification of cancer targets and therapeutics using phage display. *Current Opinion in Drug Discovery and Development*, 9(3):363, 2006.

[176] Girja S Shukla and David N Krag. Phage-displayed combinatorial peptide libraries in fusion to β-lactamase as reporter for an accelerated clone screening: Potential uses of selected enzyme-linked affinity reagents in downstream applications. *Combinatorial chemistry & high throughput screening*, 13(1):75, 2010.

[177] Zeyu Xiao, Etgar Levy-Nissenbaum, Frank Alexis, Andrej Lupták, Benjamin A Teply, Juliana M Chan, Jinjun Shi, Elise Digga, Judy Cheng, Robert Langer, et al. Engineering of targeted nanoparticles for cancer therapy using internalizing aptamers isolated by cell-uptake selection. *ACS nano*, 6(1):696–704, 2012.

[178] Omid C Farokhzad, Sangyong Jon, Ali Khademhosseini, Thanh-Nga T Tran, David A LaVan, and Robert Langer. Nanoparticle-aptamer bioconjugates a new approach for targeting prostate cancer cells. *Cancer research*, 64(21):7668–7672, 2004.

[179] Omid C Farokhzad, Jianjun Cheng, Benjamin A Teply, Ines Sherifi, Sangyong Jon, Philip W Kantoff, Jerome P Richie, and Robert Langer. Targeted nanoparticle-aptamer bioconjugates for cancer chemotherapy in vivo. *Proceedings of the National Academy of Sciences*, 103(16):6315–6320, 2006.

[180] Avi Schroeder, Daniel A Heller, Monte M Winslow, James E Dahlman, George W Pratt, Robert Langer, Tyler Jacks, and Daniel G Anderson. Treating metastatic cancer with nanotechnology. *Nature Reviews Cancer*, 12(1):39–50, 2012.

[181] Stephanie D Steichen, Mary Caldorera-Moore, and Nicholas A Peppas. A review of current nanoparticle and targeting moieties for the delivery of cancer

therapeutics. *European Journal of Pharmaceutical Sciences*, 48(3):416–427, 2013.

[182] Anthony F Jerant, Jennifer T Johnson, Catherine Demastes Sheridan, and Timothy J Caffrey. Early detection and treatment of skin cancer. *American family physician*, 62(2), 2000.

[183] William Tuong, Lily S. Cheng, and April W. Armstrong. Melanoma: Epidemiology, diagnosis, treatment, and outcomes. *Dermatologic Clinics*, 30(1):113 – 124, 2012. United States Skin Disease Needs Assessment.

[184] Margaret A. Tucker. Melanoma epidemiology. *Hematology/Oncology Clinics of North America*, 23(3):383 – 395, 2009. Advances in Melanoma.

[185] Marianne Berwick, Esther Erdei, and Jennifer Hay. Melanoma epidemiology and public health. *Dermatologic Clinics*, 27(2):205 – 214, 2009. Dermatologic Epidemiology and Public Health.

[186] Claus Garbe and Ulrike Leiter. Melanoma epidemiology and trends. *Clinics in dermatology*, 27(1):3–9, 2009.

[187] Claus Garbe, Thomas K Eigentler, Ulrich Keilholz, Axel Hauschild, and John M Kirkwood. Systematic review of medical treatment in melanoma: current status and future prospects. *The oncologist*, 16(1):5–24, 2011.

[188] W Li and DW Melton. Cisplatin regulates the MAPK kinase pathway to induce increased expression of DNA repair gene ERCC1 and increase melanoma chemoresistance. *Oncogene*, 31(19):2412–2422, 2012.

[189] Carrie Lee, Frances Collichio, David Ollila, and Stergios Moschos. Historical review of melanoma treatment and outcomes. *Clinics in dermatology*, 31(2):141–147, 2013.

[190] Keith T Flaherty, F Stephen Hodi, and David E Fisher. From genes to drugs: targeted strategies for melanoma. *Nature Reviews Cancer*, 12(5):349–361, 2012.

[191] Christian U Blank, Anna I Hooijkaas, John B Haanen, and Ton N Schumacher. Combination of targeted therapy and immunotherapy in melanoma. *Cancer Immunology, Immunotherapy*, 60(10):1359–1371, 2011.

[192] Alexander M Menzies and Georgina V Long. Dabrafenib and trametinib, alone and in combination for BRAF-mutant metastatic melanoma. *Clinical Cancer Research*, 2014.

[193] Francesca Baldelli Bombelli, Carl A Webster, Marc Moncrieff, and Victoria Sherwood. The scope of nanoparticle therapies for future metastatic melanoma treatment. *The lancet oncology*, 15(1):e22–e32, 2014.

[194] Jin Sun, Cong Luo, Yongjun Wang, and Zhonggui He. The holistic 3M modality of drug delivery nanosystems for cancer therapy. *Nanoscale*, 5(3):845–859, 2013.

[195] Andrew M. Smith, Hongwei Duan, Aaron M. Mohs, and Shuming Nie. Bioconjugated quantum dots for in vivo molecular and cellular imaging. *Advanced Drug Delivery Reviews*, 60(11):1226–1240, 2008.

[196] Susan L. Deutscher. Phage display in molecular imaging and diagnosis of cancer. *Chemical Reviews*, 110(5):3196–3211, 2010.

[197] Lilach Agemy, Dinorah Friedmann-Morvinski, Venkata Ramana Kotamraju, Lise Roth, Kazuki N Sugahara, Olivier M Girard, Robert F Mattrey, Inder M Verma, and Erkki Ruoslahti. Targeted nanoparticle enhanced proapoptotic peptide as potential therapy for glioblastoma. *Proceedings of the National Academy of Sciences*, 108(42):17450–17455, 2011.

[198] Steven Lemieux and M Kyle Hadden. Targeting the fibroblast growth factor receptors for the treatment of cancer. *Anti-Cancer Agents in Medicinal Chemistry (Formerly Current Medicinal Chemistry-Anti-Cancer Agents)*, 13(5):748–761, 2013.

[199] Maria S Aguzzi, Debora Faraone, Daniela D'Arcangelo, Francesco De Marchis, Gabriele Toietta, Domenico Ribatti, Alberto Parazzoli, Paolo Colombo, Maurizio C Capogrossi, and Antonio Facchiano. The FGF-2-derived peptide FREG inhibits melanoma growth in vitro and in vivo. *Molecular Therapy*, 19(2):266–273, 2010.

[200] Gaëlle Lefèvre, Narjes Babchia, Armelle Calipel, Frédéric Mouriaux, Anne-Marie Faussat, Stefanie Mrzyk, and Frédéric Mascarelli. Activation of the FGF2/FGFR1 autocrine loop for cell proliferation and survival in uveal melanoma cells. *Investigative ophthalmology & visual science*, 50(3):1047–1057, 2009.

[201] John T Lee and Meenhard Herlyn. Microenvironmental influences in melanoma progression. *Journal of cellular biochemistry*, 101(4):862–872, 2007.

[202] Antonio Facchiano, Katia Russo, Angelo M Facchiano, Francesco De Marchis, Francesco Facchiano, Domenico Ribatti, Maria S Aguzzi, and Maurizio C Capogrossi. Identification of a novel domain of fibroblast growth factor 2 controlling its angiogenic properties. *Journal of Biological Chemistry*, 278(10):8751–8760, 2003.

[203] Johanna A Joyce. Therapeutic targeting of the tumor microenvironment. *Cancer cell*, 7(6):513–520, 2005.

[204] Tomi K Sawyer, Pauline J Sanfilippo, Victor J Hruby, Michael H Engel, Christopher B Heward, Jean B Burnett, and Mac E Hadley. 4-norleucine, 7-d-phenylalanine-alpha-melanocyte-stimulating hormone: a highly potent alpha-melanotropin with ultralong biological activity. *Proceedings of the National Academy of Sciences*, 77(10):5754–5758, 1980.

[205] JianQing Chen, Zhen Cheng, Timothy J Hoffman, Silvia S Jurisson, and Thomas P Quinn. Melanoma-targeting properties of ^{99m}technetium-labeled cyclic α-melanocyte-stimulating hormone peptide analogues. *Cancer research*, 60(20):5649–5658, 2000.

[206] Wei Lu, Chiyi Xiong, Guodong Zhang, Qian Huang, Rui Zhang, Jin Z Zhang, and Chun Li. Targeted photothermal ablation of murine melanomas with melanocyte-stimulating hormone analog–conjugated hollow gold nanospheres. *Clinical cancer research*, 15(3):876–886, 2009.

[207] Gillian Hunt, Carole Todd, Janet E Cresswell, and Anthony J Thody. Alpha-melanocyte stimulating hormone and its analogue Nle4DPhe7 alpha-msh affect morphology, tyrosinase activity and melanogenesis in cultured human melanocytes. *Journal of Cell Science*, 107(1):205–211, 1994.

[208] Ningwen Zhu, Paula C Eves, Effie Katerinaki, Marika Szabo, Renato Morandini, Ghanem Ghanem, Paul Lorigan, Sheila MacNeil, and John W Haycock. Melanoma cell attachment, invasion, and integrin expression is upregulated by tumor necrosis factor α and suppressed by α melanocyte stimulating hormone. *Journal of investigative dermatology*, 119(5):1165–1171, 2002.

[209] Marianne M Stanford and Grant McFadden. Myxoma virus and oncolytic virotherapy: a new biologic weapon in the war against cancer. *Expert Opinion on Biological Therapy*, 7(9):1415–1425, 2007.

[210] Taghrid S Istivan, Elena Pirogova, Emily Gan, Nahlah M Almansour, Peter J Coloe, and Irena Cosic. Biological effects of a de novo designed myxoma virus peptide analogue: evaluation of cytotoxicity on tumor cells. *PloS one*, 6(9):e24809, 2011.

[211] Marianne M Stanford, Mae Shaban, John W Barrett, Steven J Werden, Philippe-Alexandre Gilbert, Joe Bondy-Denomy, Lisa MacKenzie, Kevin C Graham, Ann F Chambers, and Grant McFadden. Myxoma virus oncolysis of primary and metastatic B16F10 mouse tumors in vivo. *Molecular Therapy*, 16(1):52–59, 2007.

[212] Nahlah M Almansour, Elena Pirogova, Peter J Coloe, Irena Cosic, and Taghrid S Istivan. A bioactive peptide analogue for myxoma virus protein with a targeted cytotoxicity for human skin cancer in vitro. *J Biomed Sci*, 19(1):65, 2012.

[213] Erkki Ruoslahti and Michael D Pierschbacher. Arg-Gly-Asp: a versatile cell recognition signal. *Cell*, 44(4):517–518, 1986.

[214] MA Buerkle, SA Pahernik, A Sutter, A Jonczyk, K Messmer, and M Dellian. Inhibition of the alpha-ν integrins with a cyclic RGD peptide impairs angiogenesis, growth and metastasis of solid tumours in vivo. *British journal of cancer*, 86(5):788–795, 2002.

[215] Tamotsu Zako, Hiroyasu Nagata, Naofumi Terada, Arata Utsumi, Masafumi Sakono, Masafumi Yohda, Hiroshi Ueda, Kohei Soga, and Mizuo Maeda. Cyclic RGD peptide-labeled upconversion nanophosphors for tumor cell-targeted imaging. *Biochemical and biophysical research communications*, 381(1):54–58, 2009.

[216] Sabine Zitzmann, Volker Ehemann, and Manfred Schwab. Arginine-glycine-aspartic acid (RGD)-peptide binds to both tumor and tumor-endothelial cells in vivo. *Cancer research*, 62(18):5139–5143, 2002.

[217] Adam J Gormley, Alexander Malugin, Abhijit Ray, Ryan Robinson, and Hamidreza Ghandehari. Biological evaluation of RGDfK-gold nanorod conjugates for prostate cancer treatment. *Journal of drug targeting*, 19(10):915–924, 2011.

[218] Praveen K Dubey, Vivek Mishra, Sanyog Jain, Sunil Mahor, and SP Vyas. Liposomes modified with cyclic RGD peptide for tumor targeting. *Journal of drug targeting*, 12(5):257–264, 2004.

[219] Dorota Bartczak and Antonios G Kanaras. Preparation of peptide-functionalized gold nanoparticles using one pot EDC/sulfo-NHS coupling. *Langmuir*, 27(16):10119–10123, 2011.

[220] Samuel J Clarke, CA Hollmann, Faisal A Aldaye, and Jay L Nadeau. Effect of ligand density on the spectral, physical, and biological characteristics of CdSe/ZnS quantum dots. *Bioconjugate chemistry*, 19(2):562–568, 2008.

[221] Noumie Surugau and Pawel L Urban. Electrophoretic methods for separation of nanoparticles. *Journal of separation science*, 32(11):1889–1906, 2009.

[222] Koji Nakamura, Keiko Yamashita, Yuki Itoh, Keisuke Yoshino, Shigenori Nozawa, and Hiroaki Kasukawa. Comparative studies of polyethylene glycol-modified liposomes prepared using different PEG-modification methods. *Biochimica et Biophysica Acta (BBA)-Biomembranes*, 1818(11):2801–2807, 2012.

[223] F Benyettou, J Hardouin, Marc Lecouvey, H Jouni, and L Motte. Pegylated versus non-pegylated γ-Fe_2O_3@ alendronate nanoparticles. *Journal of Bioanalysis & Biomedicine*, 4(3), 2012.

[224] Evan J Begg. *Instant clinical pharmacology*, volume 2. Blackwell publishing, 2002.

[225] Lihong V Wang and Song Hu. Photoacoustic tomography: in vivo imaging from organelles to organs. *Science*, 335(6075):1458–1462, 2012.

[226] Srivalleesha Mallidi, Timothy Larson, Justina Tam, Pratixa P Joshi, Andrei Karpiouk, Konstantin Sokolov, and Stanislav Emelianov. Multiwavelength photoacoustic imaging and plasmon resonance coupling of gold nanoparticles for selective detection of cancer. *Nano letters*, 9(8):2825–2831, 2009.

[227] Jason R Cook, Wolfgang Frey, and Stanislav Emelianov. Quantitative photoacoustic imaging of nanoparticles in cells and tissues. *ACS nano*, 7(2):1272–1280, 2013.

KEY TO ABBREVIATIONS

2PA: two-photon absorbance cross-section

AMF: alternating magnetic field

AUC: Area under the curve

CNT: carbon nanotube

cRGD: cyclic RGD peptide

CT: computed tomography

CTLA-4: cytotoxic T-lympocyte-associated antigen 4

DDSA: dodecenyl succinic anhydride

dH_2O: distilled water

DMEM: Dulbecco's modified eagle medium

DMP-30: tris(dimethylaminomehtyl)phenol

DMSO: dimethyl sulfoxide

DNA: deoxyribonucleic acid

Dox: doxorubicin

EDC: 1-ethyl-3-(3-dimethylaminopropyl)carbodiimide

EDS: energy dispersive X-ray spectrometry

EDTA: ethylenediaminetetraacetic acid

EGFR: epidermal growth factor receptor

EPR: enhanced permeability and retention

ESEM: enivronmental scanning electron microscopy

FAM: carboxyfluorescein

FDA: United States Food and Drug Administration

FGF: fibroblast growth factor

FREG: FREG peptide

GNRT: gold-nanoparticle assisted radiation therapy

HBSS: Hank's balanced salt solution

HER2: human epidermal growth factor receptor 2

HNC: head and neck cancer

HPLC: high-performance liquid chromatography

IC_{50}: half maximal inhibitory concentration

ICPMS: inductively-coupled plasma mass spectroscopy

IDE: investigational device exemption

INAA: instrumental neutron activation analysis

IR: infrared

MAPK: mitogen-activated protein kinase

MQQ: multilayered, core/shell nano-

MRI: magnetic resonance imaging

MSH: alpha melanocyte stimulating hormone analogue peptide

Myx: myxoma peptide

NHS: N-hydrosuccinimide

NIR: near-infrared

NIRF: near-infrared fluorescence

NMA: nadic methyl anhydride

NP: nanoparticle

PAGE: polyacrylamide gel electrophoresis

PBS: phosphate buffer solution

PDT: photodynamic therapy

PEG: polyethylene glycol

PSMA: prostate specific membrane antigen

QD: quantum dot

RES: reticuloendothelial system

ROI: region of interest

ROS: reactive oxygen species

RPMI: Roswell Park Memorial Institute medium

RRM: resonant recognition model

SCID: severe combined immunodeficiency

SDS: sodium dodecyl sulfate

SEM: standard error of the mean

SH-5KPEG-COOH: carboxymethyl-PEG-thiol (molecular weight 5 kDa)

SPECT: single-photon emission computed tomography

SPIO: superparamagnetic iron oxide

SRB: sulforhodamine B

STEM: scanning transmission electron microscopy

T_1: longitudinal / spin-lattice relaxation

T_2: transverse / spin-spin relaxation

TAE: tris(hydroxymethyl)aminomethane base, acetic acid, and ethylenediaminetetraacetic acid

TCA: trichloroacetic acid

TEM: transmission electron microscopy

UCNP: upconversion nanoparticle

USPIO: ultrasmall superparamagnetic iron oxide

UV: ultraviolet

VEGF: vascular endothelial growth factor